



**HAL**  
open science

# Strength and Stability of Cross-Laminated-Timber Walls at Short and Long Term

Olivier Perret

► **To cite this version:**

Olivier Perret. Strength and Stability of Cross-Laminated-Timber Walls at Short and Long Term. Matériaux composites et construction. Université Paris-Est, 2017. English. NNT : 2017PESC1246 . tel-02003154

**HAL Id: tel-02003154**

**<https://pastel.hal.science/tel-02003154>**

Submitted on 1 Feb 2019

**HAL** is a multi-disciplinary open access archive for the deposit and dissemination of scientific research documents, whether they are published or not. The documents may come from teaching and research institutions in France or abroad, or from public or private research centers.

L'archive ouverte pluridisciplinaire **HAL**, est destinée au dépôt et à la diffusion de documents scientifiques de niveau recherche, publiés ou non, émanant des établissements d'enseignement et de recherche français ou étrangers, des laboratoires publics ou privés.

UNIVERSITÉ PARIS-EST  
ECOLE DOCTORALE SCIENCE INGÉNIÉRIE ET  
ENVIRONNEMENT

## THÈSE

présentée pour l'obtention du grade de  
Docteur de l'Université Paris-Est

Spécialité : Matériaux et Structures

par

Olivier Perret

# STRENGTH AND STABILITY OF CROSS LAMINATED TIMBER WALLS AT SHORT AND LONG TERM

RÉSISTANCE ET STABILITÉ DE MURS EN BOIS LAMELLÉ-CROISÉ À  
COURT ET À LONG TERME

Soutenance prévue le 4 décembre 2017 devant le jury composé de :

M. PHILIPPE GALIMARD	<i>Rapporteur</i>
M. PANAGIOTIS KOTRONIS	<i>Rapporteur</i>
M. LAURENT BLÉRON	<i>Examineur</i>
M. CYRIL DOUTHE	<i>Examineur</i>
M. ARTHUR LEBÉE	<i>Examineur</i>
M. KARAM SAB	<i>Directeur de thèse</i>





---

## Remerciements

Je tiens tout d'abord à remercier le directeur de cette thèse, le Professeur Karam Sab, qui m'a permis de faire cette thèse au sein du laboratoire Navier qui m'a fourni tous les moyens matériels nécessaires au bon déroulement de ce travail. Je le remercie de m'avoir fait confiance malgré les faibles connaissances que j'avais sur les techniques d'homogénéisation en 2014, puis de m'avoir guidé et conseillé pendant plus de trois ans afin que mes travaux fournissent des éléments innovants à la communauté du bois.

Je tiens également à exprimer ma gratitude au Dr. Arthur Lebée et au Dr. Cyril Douthe, co-encadrants de cette thèse, pour leur très grande disponibilité tout au long de sa réalisation, pour leur suivi au quotidien, pour leurs encouragements et leurs conseils avisés et complémentaires.

Je remercie également tous les membres de l'équipe Matériaux et Structures Architecturées qui m'ont aidé à mener à bien mes expériences, à développer mes capacités à mettre en place un protocole expérimental et à résoudre les problèmes et les aléas inhérents à la mise en place d'une expérience. Je pense en particulier à Jean-François, Gilles, Sabine, Marie-Françoise, Géraldine, Hocine, Gilles, Daniel et Christophe.

Je remercie également les doctorants et stagiaires du laboratoire Navier qui m'ont côtoyé pendant ma thèse et en particulier Laura, Déborah et Amine avec qui j'ai partagé le quotidien avec ses hauts et ses bas et dont le soutien m'a permis de rester motivé même dans la difficulté.

Je souhaite également remercier tous mes amis qui m'ont soutenu pendant les moments difficiles et qui m'ont aidé à les affronter. Je tiens en particulier à remercier Gabrielle pour son amitié indéfectible et ses encouragements permanents et à qui je souhaite la même réussite dans ses travaux de thèse.

Enfin je tiens à remercier ma famille pour son soutien permanent malgré la distance qui nous a séparé pendant ses trois ans, mais qui ne les a pas stoppé pour venir assister à ma soutenance de thèse. Je remercie tout particulièrement ma soeur Louise et son futur époux Pierrick ainsi que mon père Richard et ma mère Véronique qui ont su m'épauler et me remonter le moral dans les tous les moments difficiles que j'ai rencontré.

---

Je dédie cette thèse à ma grand-mère Yvonne qui nous prouve tous les jours que l'âge peut rimer avec énergie, courage et bonne humeur.



à Yvonne



---

# Contents

<b>Contents</b>	<b>7</b>
<b>List of Figures</b>	<b>11</b>
<b>List of Tables</b>	<b>15</b>
<b>General Introduction</b>	<b>17</b>
<b>I Stiffness of CLT panels</b>	<b>23</b>
<b>1 Equivalent layer stiffness of CLT: Closed-form bounds and numerical validation</b>	<b>25</b>
1.1 Introduction . . . . .	25
1.2 Closed-form expressions for the equivalent layer stiffness . . . . .	27
1.2.1 Stiffness and compliance averages . . . . .	28
1.2.2 Reuss lower bound and Voigt upper bound for varying sawing pattern . . . . .	30
1.3 Equivalent-layer stiffness of Norway-Spruce . . . . .	35
1.3.1 Equivalent Young moduli . . . . .	35
1.3.1.1 Equivalent longitudinal Young modulus $E_L$ . . . . .	35
1.3.1.2 Equivalent normal and cross Young moduli $E_Z$ and $E_C$ . . . . .	36
1.3.1.3 Poisson's ratio $\nu_{LC}$ and $\nu_{CL}$ . . . . .	37
1.3.2 Equivalent shear moduli . . . . .	37
1.3.2.1 Equivalent longitudinal-layer and in-plane shear moduli $G_{LZ}$ and $G_{LC}$ . . . . .	38
1.3.3 Equivalent cross-layer shear stiffness $G_{CZ}$ . . . . .	38
1.4 Influence of the free narrow edges on cross-layer shear stiffness $G_{CZ}$ . . . . .	39

1.4.1	Presentation of the numerical model . . . . .	40
1.4.2	Discussion . . . . .	42
1.5	Conclusion . . . . .	45
<b>2</b>	<b>Experimental determination of the equivalent-layer shear stiffness of CLT through four point bending of sandwich beams</b>	<b>47</b>
2.1	Introduction . . . . .	47
2.1.1	Tests at the ring scale . . . . .	48
2.1.2	Tests at the individual board scale . . . . .	50
2.1.3	Tests at the beam scale . . . . .	51
2.1.4	Tests at a single layer scale . . . . .	52
2.2	Identification by four point bending of homogeneous sandwich beam . .	52
2.2.1	The sandwich beam model . . . . .	53
2.2.2	The four point bending test . . . . .	54
2.2.3	Validation of the sandwich beam model with a 3D finite element model . . . . .	56
2.2.3.1	The 3D model . . . . .	56
2.2.3.2	Accuracy of the stress estimation in the core . . . . .	57
2.2.3.3	Accuracy of the global deflection estimation . . . . .	59
2.2.3.4	Stiffness identification . . . . .	60
2.3	Experimental campaign . . . . .	61
2.3.1	Specimen fabrication . . . . .	61
2.3.2	Identification of bending and shear stiffness with the four point bending test . . . . .	62
2.3.3	Experimental setup . . . . .	63
2.4	Identification of the equivalent cross-layer shear stiffness . . . . .	64
2.4.1	Deflections and rotations during loading and unloading . . . . .	64
2.4.2	Stiffness measurements . . . . .	66
2.5	Conclusion . . . . .	67
<b>II</b>	<b>Stability of CLT walls at short and long term</b>	<b>69</b>
<b>3</b>	<b>The Bending-Gradient theory for the linear buckling of thick plates: Application to Cross-Laminated-Timber panels</b>	<b>71</b>
3.1	Introduction . . . . .	71
3.2	Linear buckling of plates with the Bending-Gradient theory . . . . .	75
3.2.1	Notations . . . . .	75
3.2.2	The Bending-Gradient theory . . . . .	75
3.2.2.1	Generalized stress and strain fields . . . . .	75
3.2.2.2	Bending-Gradient constitutive equations . . . . .	77

## CONTENTS

---

3.2.2.3	Projections of the Bending-Gradient model on Reissner-Mindlin models . . . . .	78
3.2.2.4	Simple support boundary conditions . . . . .	80
3.2.3	Linear buckling analysis with the Bending-Gradient theory . . .	81
3.2.3.1	The linearized 3D stress state under in-plane compression . . . . .	81
3.2.3.2	Buckling load calculation . . . . .	83
3.3	3D reference model for the linear buckling of CLT panels . . . . .	84
3.3.1	The 3D linear buckling problem . . . . .	84
3.3.1.1	The pre-stressed state . . . . .	84
3.3.1.2	Buckling modes calculation . . . . .	86
3.3.1.3	Timber elastic characteristics and CLT configurations . . . . .	87
3.3.2	Application of the 3D linear buckling to CLT panels . . . . .	88
3.3.2.1	Global behavior of the plate . . . . .	88
3.3.2.2	Buckling load and compressive strength of HSS CLT panels . . . . .	89
3.4	Comparison between numerical results and plate models . . . . .	92
3.4.1	CLT panel stiffness for practical configurations . . . . .	92
3.4.2	Influence of slenderness $\frac{b}{h}$ . . . . .	93
3.4.3	Influence of the plate aspect ratio $\frac{a}{b}$ . . . . .	96
3.4.4	Accuracy of the shear compliance stiffness projection for SSS plates . . . . .	97
3.5	Conclusions . . . . .	99
<b>4</b>	<b>Buckling of CLT columns with initial imperfections</b>	<b>101</b>
4.1	Introduction . . . . .	101
4.2	Buckling of a columns with imperfections . . . . .	103
4.2.1	Linear buckling of a column without imperfections . . . . .	103
4.2.2	Buckling of a column with initial imperfections . . . . .	106
4.2.3	Ayrton and Perry criterion . . . . .	110
4.3	Proposed shear force criterion . . . . .	111
4.3.1	Definition of the shear criterion . . . . .	111
4.3.2	Comparison between Ayrton-Perry formula and shear criterion . . . . .	113
4.4	Conclusion . . . . .	115
<b>5</b>	<b>Long-term buckling of CLT columns</b>	<b>117</b>
5.1	Wood: a viscoelastic material . . . . .	117
5.1.1	Viscoelastic behavior of wood in longitudinal direction . . . . .	117
5.1.2	Influence of climate conditions . . . . .	120
5.1.3	Orthotropic creep . . . . .	121
5.2	Definition of the problem . . . . .	122

## CONTENTS

---

5.3	Long term buckling of an imperfect Euler column . . . . .	124
5.4	Viscoelastic behavior of a column with the Timoshenko beam model under constant loading . . . . .	127
5.5	Influence of the orthotropic viscoelastic behavior on the Ayrton-Perry criterion . . . . .	130
5.5.1	Viscoelastic behavior with two creep factors $k_{\text{def},D}$ and $k_{\text{def},F}$ . . .	130
5.5.2	Viscoelastic behavior with two modification factors $k_{\text{mod},D}$ and $k_{\text{mod},F}$ . . . . .	132
5.6	Conclusion . . . . .	132
	<b>General Conclusion</b>	<b>135</b>
<b>A</b>	<b>Annexes</b>	<b>137</b>
A.1	The Timoshenko beam model . . . . .	137
A.2	Resolution of the linear buckling with the Bending-Gradient theory us- ing Voigt's notations . . . . .	142
A.3	Deflection of CLT wall with initial imperfections . . . . .	145
	<b>Bibliography</b>	<b>147</b>

# List of Figures

1	CLT panel . . . . .	17
2	Hoho building project . . . . .	18
1.1	Local and global orientations in a board . . . . .	27
1.2	Scheme of the board section . . . . .	31
1.3	Integration of mechanical properties on $A_1$ . . . . .	31
1.4	Scheme of the board section with a distance $z_1$ to the pith . . . . .	33
1.5	Scheme of the board section with a distance $z_1$ to the pith . . . . .	34
1.6	Reuss lower bound (left) and Voigt upper bound (right) for the estimation of $E_Z$ (MPa) . . . . .	36
1.7	Reuss lower bound (left) and Voigt upper bound (right) for the estimation of $E_C$ (MPa) . . . . .	37
1.8	Young moduli of Voigt and Reuss bounds for $z_1 = 0$ . . . . .	38
1.9	Reuss lower bound (left) and Voigt upper bound (right) for the estimation of $G_{CZ}$ (MPa) . . . . .	39
1.10	2D numerical simulation for calculation of the equivalent cross-layer shear stiffness (Aicher and Dill-Langer, 2000) . . . . .	41
1.11	Simplification of the model because of periodicity and symmetries . . . . .	41
1.12	2D numerical simulation for calculation of the equivalent cross-layer shear stiffness of CLT with glued edges . . . . .	42
1.13	2D numerical simulation for calculation of the equivalent cross-layer shear stiffness of CLT and with free edges . . . . .	43
1.14	Equivalent cross-layer shear moduli of Voigt and Reuss bounds for $z_1 = 1.5t$ . . . . .	44
1.15	Equivalent cross-layer shear moduli of Voigt and Reuss bounds for $\alpha = 26.6^\circ$ . . . . .	44
1.16	Equivalent cross-layer shear moduli of Voigt and Reuss bounds for $z_1 = 0.1t$ . . . . .	45

LIST OF FIGURES

2.1	Notched shear block test (Dahl and Malo, 2009a) (left), Arcan shear test (Dahl and Malo, 2009a) (center) and Single-lap shear test (right) (Ehrhart et al., 2015) . . . . .	49
2.2	Four point bending of a CFRP sandwich beam with wooden core . . . . .	52
2.3	Distribution of shear stress $\sigma_{xz}$ in the wooden core relatively to the estimation of the stress $\sigma_{xz}^c$ in the core . . . . .	54
2.4	Four point Bending test . . . . .	55
2.5	3D shear stress distribution $\sigma_{xz}(x, 0, z)$ compared to sandwich beam estimation $\sigma_s$ . . . . .	57
2.6	Shear stress $\sigma_{xz}$ along the beam for upper, lower and neutral fiber in the core from 3D and sandwich beam models . . . . .	58
2.7	Distribution of stresses $\sigma_{xx}$ , $\sigma_{zz}$ and $\sigma_{xz}$ in timber normalized with the corresponding strength . . . . .	58
2.8	Distribution of stresses $\sigma_{zz}$ in CFRP normalized with the tensile and compressive strength . . . . .	59
2.9	Relative deflection between sandwich and 3D models normalized with the mid-span deflection . . . . .	60
2.10	Weight functions for the integration of the bending compliance and the shear compliance over the beam . . . . .	62
2.11	Experimental setup . . . . .	63
2.12	Experimental loading sequence . . . . .	64
2.13	Force-Deflection diagram for the mid-span deflection $f_A$ (left) and force-rotation diagram for the relative rotation at support $\varphi_0$ (right) . . . . .	65
2.14	Force-Deflection diagram for the relative deflection $\Delta f$ (left) and Force-Deformation diagram for the relative deformation $\Delta \varepsilon$ (right) . . . . .	65
2.15	Force-Deflection diagram for anti-symmetrical deflection at $B$ and $B'$ (left) and force-rotation diagram for anti-symmetrical rotation at support (right) . . . . .	66
3.1	2D plate under out-of-plane loading . . . . .	76
3.2	Settings of the buckling problem of a simply supported plate under unilateral load . . . . .	82
3.3	3D Boundary conditions of the buckling mode calculation step . . . . .	85
3.4	Model of the uniform membrane pre-stress during the stress perturbation step in Abaqus calculation . . . . .	86
3.5	3D Boundary conditions of the buckling mode calculation step . . . . .	86
3.6	3D distribution of $\sigma_{12}$ for a 5-ply CLT square panels with $\frac{b}{h} = 15$ on SSS or HSS edges . . . . .	88
3.7	Ratio between the in-plane shear stress $\sigma_{12}$ of SSS and HSS 5-ply CLT square panels with $\frac{b}{h} = 15$ along the path $\mathcal{C}$ (Figure 3.6) . . . . .	89

*LIST OF FIGURES*

---

3.8	Displacement $u_1$ according to thickness for an HSS 5-ply CLT square panel with $\frac{b}{h} = 15$ . . . . .	90
3.9	Relative difference between HSS and SSS with varying slenderness $\frac{b}{h}$ and plate aspect ratio $\frac{a}{b}$ . . . . .	90
3.10	Ratio between reference 3D buckling load and compressive strength for a HSS square CLT panel . . . . .	91
3.11	Ratio between buckling load and compressive strength according to slenderness $\frac{b}{h}$ for a HSS 5ply-CLT square panel . . . . .	94
3.12	Relative error of plate models compared to 3D results for a HSS 5-ply-CLT square panel . . . . .	94
3.13	Ratio between the buckling load and the compressive strength according to slenderness $\frac{b}{h}$ for a HSS 3-ply-CLT square panel . . . . .	95
3.14	Relative error of plate models compared to 3D results for a HSS 3-ply-CLT square panel . . . . .	95
3.15	Ratio between the buckling load and the compressive strength according to plate ratio $\frac{a}{b}$ for a HSS 5ply-CLT with a slenderness $\frac{b}{h} = 20$ . . . . .	97
3.16	Relative error compared to numerical results for a HSS 5ply-CLT panel with a slenderness $\frac{b}{h}=20$ . . . . .	98
3.17	Relative error of the critical buckling load of SSS plates 2D results compared to 3D SSS results for 5-ply CLT plates with an aspect ratio $\frac{a}{b} = 1.22$	99
4.1	Beam under in-plane compression . . . . .	103
4.2	Definition of the deflection $f(x)$ , of the rotation of the section $\varphi(x)$ and of the global shear strain $\gamma(x)$ . . . . .	104
4.3	Beam with initial imperfection under in-plane compression . . . . .	107
4.4	Ratio $\frac{\beta(P)}{\alpha(P)}$ for varying ratios $\frac{P}{P_{cr,0}}$ and $\frac{P_{E,0}}{P_{cr,0}}$ . . . . .	109
4.5	Deflection of the beam at the equilibrium . . . . .	112
4.6	Ayrton-Perry formula (A-P) and shear criterion for CLT1 configuration .	115
4.7	Ayrton-Perry (A-P) criterion and shear criterion for CLT2 configuration	115
5.1	Creep-recovery test principle . . . . .	118
5.2	Experimental setup . . . . .	119
5.3	Poynting-Thomson . . . . .	122
5.4	Viscoelastic column with initial imperfection under compression . . . .	125
5.5	Ayrton-Perry formula and shear criterion at long-term with two creep factors $k_{def,D}$ and $k_{def,F}$ for configuration CLT1 . . . . .	131
5.6	Ayrton-Perry formula and shear criterion at long-term with two creep factors $k_{def,D}$ and $k_{def,F}$ for configuration CLT2 . . . . .	131
5.7	Ayrton-Perry formula and shear criterion at long-term with two modification factors $k_{mod,D}$ and $k_{mod,F}$ for configuration CLT1 . . . . .	132

*LIST OF FIGURES*

---

5.8	Ayrton-Perry formula and shear criterion at long-term with two modification factors $k_{\text{mod},D}$ and $k_{\text{mod},F}$ for configuration CLT2 . . . . .	133
A.1	Scheme of a beam . . . . .	138
A.2	Definition of the deflection $f(x)$ , of the rotation of the section $\varphi(x)$ and of the global shear strain $\gamma(x)$ . . . . .	138
A.3	Scheme of an elementary part of the beam of length $dx$ . . . . .	140

# List of Tables

1.1	Elastic Properties of Norway Spruce (Keunecke et al., 2007, 2008) . . .	35
2.1	Mechanical characteristics of wood and carbon fiber reinforced polymer	57
2.2	Relative error of the estimation of stiffnesses $E_{L,CFRP}^{est}$ and $G_{NZ}^{est}$ by the sandwich beam model compared to input variables $E_{L,CFRP}$ and $G_{CZ}$ . .	61
2.3	$E_{L,CFRP}$ (GPa) measures from $\Delta f$ , $\varepsilon_0$ and $\Delta\varepsilon$ . . . . .	67
2.4	$G_{CZ}$ (MPa) measures from $\Delta f$ , $\varepsilon_0$ and $\Delta\varepsilon$ . . . . .	68
3.1	<i>Elastic Properties of Norway Spruce, E and G in MPa (Keunecke et al., 2008)</i> . . . . .	87
3.2	Compressive strength of CLT with several configurations . . . . .	91
3.3	Bending stiffness ( $kN.m$ ) and shear compliance ( $MN.m^{-1}$ ) for a square CLT plate with a thickness $h = 0.15m$ . . . . .	93
4.1	Elastic and strength properties of Norway Spruce CLT1 and CLT2 (Schickhofer et al., 2016) . . . . .	113

*LIST OF TABLES*

---

# General Introduction

Cross Laminated Timber (CLT) is a wooden product which derives from the *Tripli* in France which consists of three wooden layers where the internal layer is oriented in the cross direction. In the early 1990s, the *Tripli* becomes popular again in Austria and Germany and was extended to various configuration and was called (Stürzenbecher et al., 2012). It consists in several lumber layers stacked crosswise and glued on their wide faces (Figure 1). There are several configurations of CLT from 3 to 11 layers generally symmetrical according to thickness. The thickness of lumber layers is between 10 to 50 mm for a total thickness of the CLT panel up to 400 mm (Karacabeyli and Douglas, 2013). The dimensions of panels depend on the manufacturer for a total width up to 4 to 5 m and a length up to 18 m.

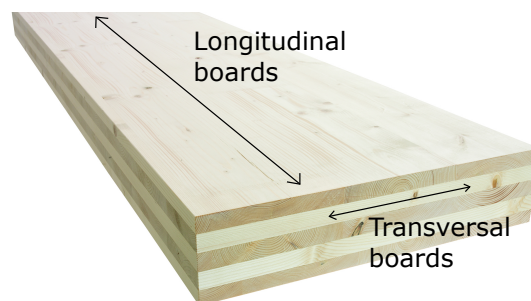


Figure 1 – CLT panel

During the last twenty years, CLT structures have gained in popularity for several reasons. First CLT panels have a low environmental impact which is an advantage compared to other construction materials such as steel and concrete. Indeed, it is made of wood which is the result of carbon storage during the photosynthesis in leaves. The manufacturing process is low carbon compared to the manufacturing process of steel and concrete. A great part of carbon emission comes from transport and from petrochemical process. Second, the prefabrication process allows a quick and easy assembling on

site. Third, the crossing layers lead to a high dimensional stability under variation of moisture content compared to other timber products.

Consequently, numerous high-rise timber buildings projects were designed and built during the last few years such as the Ho-Ho building project at Vienna in Austria which will be 84-meters high (French, 2015). Hence, the question of the buckling of CLT walls under compressive stress becomes more important with the increasing size of timber buildings since compressive load in CLT walls become larger and larger. Moreover, because of the crossing layers, the radial-tangential shear stiffness, also called rolling shear stiffness, is involved in the global shear stiffness of the CLT panel. The rolling-shear stiffness is approximately 200 times lower than the longitudinal stiffness. Because of this large stiffness contrast, shear effects are significant compared to other timber products such as glued-laminated-timber (GLT) and contributes a lower critical buckling load. Hence, it is important to study the stability of CLT walls which is the purpose of this PhD thesis. This dissertation is divided in two parts. First in Part I, the equivalent layer stiffness of CLT is investigated with a particular attention paid to the rolling shear behavior. Second, in Part II, the stability of CLT walls is investigated by considering imperfections and also the viscoelastic behavior of timber. Each chapter can be read independently from the others and are formatted to be published in scientific journals. In the following, the articulation between the different chapter is explained.



Figure 2 – Hoho building project

Before the study of the buckling of CLT walls, it is important to define its bending and shear behavior which depends on the configurations of layers: it depends on the number and on the thickness of layers. Hence, a reasonably fair accurate mechanical behavior of a single layer is necessary to model the global behavior of the CLT panel. In most models for the design of CLT panels, each layer is assumed to be homogeneous. Nonetheless, there are several heterogeneities in layers. First, the local behavior of timber is orthotropic: there is a high stiffness contrast between longitudinal direction and radial and tangential directions. Second, at board scale, there is a variation of the local ring orientation: there is a rotation of radial and tangential directions across

the section of the board. The distribution of the local ring orientation is called the sawing pattern depending on the board aspect ratio and on the distance to the pith. Consequently, the global homogeneous equivalent behavior of the board depends on this sawing pattern. Second, at the layer scale, there are other heterogeneities. A layer is composed of several boards with different sawing patterns and then on different global behaviors. Moreover, depending on the manufacturer, a board can be glued or not to its adjacent boards. The global behavior, particularly the in-plane behavior can be very sensitive to this edge gluing. Indeed, stress cannot be transmitted from one board to another if there is no edge gluing. Thus all these heterogeneities need to be taken into account to model an equivalent homogeneous layer behavior. In Chapter 1, closed-form bounds of the equivalent-layer stiffness are suggested to take into account the variations of local ring orientation. Moreover, the impact of glued narrow edges on the equivalent-layer stiffness is discussed. Particularly, a numerical study is performed to study compare the cross-layer shear stiffness of boards with and without glued narrow edges since only few studies have been presented on the cross-layer shear stiffness. It is observed that the cross-layer shear stiffness is strongly dependent on the sawing pattern, defined as the distribution of the local ring orientation over the board section, and on the narrow edges gluing.

Consequently, in Chapter 2, we suggest a new experimental protocol to measure the cross-layer shear stiffness of timber in order to compare numerical and experimental results. We suggest to use sandwich beams with a wooden core oriented in the tangential direction and with Composite Fiber Reinforced Polymers (CFRP) skins. Because, of the high stiffness and thickness contrast between CFRP skins and the wooden core, the global shear stiffness of the sandwich beam is mostly driven by the cross-layer shear stiffness. Then, from four-point bending test on this sandwich beam, it is possible to measure the shear stiffness from the difference between the total deflection and the bending deflection. A new measurement method is also suggested by using the rotation at beam ends: it was observed that such measure is more accurate than the classical measure from the relative deflection in the area between loads since it averages mechanical properties on the whole span of the beam.

Once the equivalent-layer behavior of CLT has been defined, it is possible to investigate the buckling behavior. First in Chapter 3, a perfect CLT wall is considered without imperfections. Since the thickness of CLT is relatively small compared to the width and the length, CLT panels can be modeled as plates. Several plate models are used: the Kirchhoff-Love plate model where shear effects are neglected, the Reissner-Mindlin plate model where a linear shear strain distribution over thickness is assumed and the Bending-Gradient model which is a higher order plate model considering the gradient of the bending moment. In this last model, six variables are used to describe the shear behavior instead of two in the Reissner-Mindlin. First it is observed that the critical buckling load of a simply-supported CLT wall is of the same order of magnitude

as the compressive strength for actual CLT configurations which shows that the buckling is not negligible. Moreover, it is observed that the shear effects are important and the use of the Kirchhoff-Love model is not recommended for CLT. From the comparison with a 3D numerical model, it is observed that the Bending-Gradient model is very reliable. Besides, two projections of the Bending-Gradient model on Reissner models have been suggested and one of the projection is as reliable as the Bending-Gradient model even if only two shear variables are used. Finally, the use of this shear compliance projection seems adapted for the design of CLT walls. Additionally, two kinds of simple support, called hard and soft simple support have been considered and it was observed that they can have a significant effect on the buckling of CLT walls.

In Chapter 4, initial imperfections are considered. Indeed, an actual CLT walls have some imperfections such as straightness defect, an eccentricity of the load due to the connection system, residual stress due to the manufacturing process. Note that for sake of simplicity, a Timoshenko beam model is used here. By considering these imperfections in the equilibrium of CLT walls on the deformed configuration, the deflection of the wall is defined as non-linear function of the compressive load. These deflections lead to additional bending moment and then to additional compressive stress in the longitudinal layers. As a consequence, a compressive strength criterion can be established considering these initial imperfections: this strength criterion was first suggested by Ayrton and Perry (1886) and is also called the Ayrton-Perry formula. This criterion was adapted in the Eurocode 5 (European Committee for Standardisation, 1993) for the design of timber columns and has also been recently adapted by Thiel (2013) for the design of CLT walls. Additionally to this criterion, we suggest a new shear criterion since the rolling shear strength is very low compared to the longitudinal compressive strength. It is observed that this shear criterion may be relevant when the design rolling shear strength is low and when the slenderness is low.

Finally, wood is a viscoelastic material. Its stiffness and strength vary in time. The viscoelastic behavior of wood also depends on the direction of the loading. Particularly, the rolling shear long term behavior has not been well studied until now. Whereas in current recommendations, only one parameter for the variations of the wood stiffness and one parameter for the wood strength are suggested corresponding to the longitudinal behavior, it appears that both bending and shear long term behaviors of CLT needs to be considered separately. In Chapter 5, these viscoelastic effects are considered independently for the long-term buckling of CLT walls. It is demonstrated that long-term stability criteria correspond to short term criteria using long term stiffnesses. The long term Ayrton-Perry criterion is well known and recalled from (Bažant and Cedolin, 1991) for the Euler beam model. In this chapter, we extend the problem to Timoshenko beam model by considering separately the bending and the shear creep. It is shown that the long-term Ayrton-Perry criterion can be extended to the Timoshenko beam model by considering the long-term Timoshenko critical buckling load instead of the long-term

## *General Introduction*

---

Euler critical buckling load. Moreover, it is shown, because of the orthotropic viscoelastic behavior of wood that the long term shear criterion can be relevant in a larger range of CLT configurations than at short term showing the necessity to study the long term rolling shear behavior.



# **Part I**

---

## **Stiffness of CLT panels**



---

# Equivalent layer stiffness of CLT: Closed-form bounds and numerical validation

*In order to study the buckling of CLT wall, it is first necessary to define the thick plate bending and shear stiffness of CLT which can be derived from the equivalent-layer stiffness. Since the wood is an heterogeneous material, an homogenization method is necessary to suggest an equivalent-layer stiffness from local properties. First, we suggest to integrate local mechanical properties of the wood, defined in the local orthotropic coordinate system, over the board cross section. Second, the impact of the narrow-glued edges is discussed with a focus on the cross-layer shear stiffness by means of a numerical study. This work was recently submitted (Perret et al., 2017a).*

## 1.1 Introduction

Cross-Laminated-Timber (CLT) consists in lumber layers stacked crosswise and glued on their lower and upper faces. Its quick and easy assembling, its low self-weight and its low environmental impact make this product competitive. In the last few years, several timber buildings made of CLT were built mainly in Northern America and in Western Europe such as Murray Grove in London (Lomholt, 2015) and the Treet in central Bergen (Mairs, 2016).

Nevertheless, the behavior of CLT panels is complex because of several heterogeneities at different scales. Here we discuss only heterogeneities larger than the annual ring. Moreover, wood has a strong variability compared to materials such as steel and concrete. This variability is also not discussed in the following.

At ring scale, wood elastic behavior is generally modeled as an orthotropic material with three main directions: the longitudinal direction  $L$  corresponding to wood fiber orientation, the radial and tangential directions  $R$  and  $T$ . The fibers orientation leads to a strong stiffness and strength contrast between the stiff longitudinal direction and the flexible radial and tangential directions. At board scale, another heterogeneity is due to the rotation of the material orthotropic coordinate system  $(O, L, R, T)$  (Figure 1.1). The global orthotropic system of the board is defined as  $(O, L, C, Z)$  where  $C$  and  $Z$  stand

## 1.1. INTRODUCTION

---

for cross and normal directions (Figure 1.1). The behavior of the board depends on the distribution of ring orientation through the board section, called the sawing pattern. At layer scale, individual boards can be glued or not on their narrow edges depending on the manufacturing process. Free narrow edges lead to stress concentrations lowering the stiffness and strength of CLT panels under particular loads. Note that, for free narrow edges, self-contact may be ignored since there is a small gap between boards in practice. Finally, CLT are multi-layer panels strongly heterogeneous because of cross-wise orientations of layers.

From these observations, the mechanical behavior of CLT panels is difficult to model properly. Scale of heterogeneities cited above are not clearly distinct: the curvature radius and the thickness of annual rings are comparable with the thickness of boards, the board width is larger than the layer thickness, the number of layers in CLT is small (from three to eleven). Thus, these heterogeneities require a careful attention when using homogenization techniques.

Nevertheless, in current recommendations for the design of CLT, panels are often modeled as multilayer plates or beams. This is the case of the  $\gamma$ -method recalled in Eurocode 5 (European Committee for Standardisation, 1993, 24-02-2016) and adapted to CLT (Stora Enso, 2014) where cross-layers are modeled as mechanical joints between longitudinal layers with a stiffness related to the equivalent cross-layer shear stiffness. In the CLT-designer software, Thiel and Schickhofer (2010) suggest to use Timoshenko beam theory and derived the shear stiffness of CLT beams from the Jourawski method. Advanced models have also been suggested by Franzoni et al. (2016b) for the bending of CLT panels with regular gaps and is suggested in Chapter 3 for the buckling of CLT panels. In these methods, it is assumed that the mechanical behavior of each layer, composed of several boards, can be modeled as homogeneous. It is thus assumed that there exists an equivalent layer mechanical behavior which adequately takes into account the effect of lower scale heterogeneities such as ring distribution and narrow edges gaps.

This equivalent behavior is often based on a educated guess for a small collection of plate solicitations which emerge from practical applications. First, the longitudinal and cross Young moduli  $E_L$  and  $E_C$  are involved in the bending stiffness for CLT floors (Kreuzinger, 1999; Karacabeyli and Douglas, 2013; Stora Enso, 2014; Thiel and Schickhofer, 2010) and in the in-plane stiffness for CLT walls (Thiel, 2013; Thiel and Krenn, 2016) (Chapter 3). Because of the high stiffness contrast between  $E_L$  and  $E_C$ , the cross stiffness  $E_C$  is often neglected (Stora Enso, 2014; Thiel and Schickhofer, 2010). Moreover, because of the thickness of CLT and of the cross layers, the out-of-plane shear stiffness of CLT, composed of the longitudinal shear stiffness  $G_{LZ}$  and of the cross-layer shear stiffness  $G_{CZ}$ , is also involved in the bending (Franzoni et al., 2016b) and the buckling behavior of CLT (Chapter 3). In the shear analogy method (Kreuzinger, 1999; Karacabeyli and Douglas, 2013),  $G_{LZ}$  is neglected because of the stiffness contrast compared to  $G_{CZ}$ . On the contrary, both  $G_{LZ}$  and  $G_{CZ}$  are involved in the  $\gamma$ -

method (Stora Enso, 2014) and the Timoshenko beam theory (Thiel and Schickhofer, 2010) since the influence of  $G_{LZ}$  is generally not admissible in CLT beams. Finally, the in-plane shear stiffness  $G_{LC}$  is involved in shear walls. Particularly, it has been observed a strong influence of the narrow edge gluing and of the board aspect ratio on  $G_{LC}$  (Moosbrugger et al., 2006; Bogensperger et al., 2010; Franzoni et al., 2017a). All these parameters necessitate recommendations depending on the timber strength class, on the board aspect ratio and on the narrow edge gluing as suggested in the draft for a revised version of the Eurocode 5.1.1 (European Committee for Standardisation, 24-02-2016) but the sawing pattern can also be taken into account.

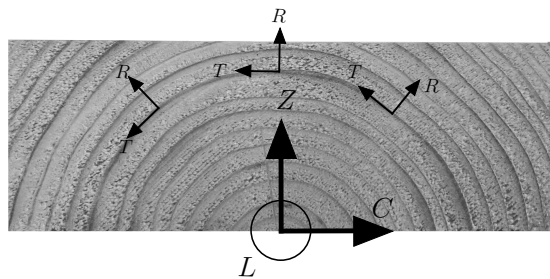


Figure 1.1 – Local and global orientations in a board

In order to give a fast and reasonable estimate of the elastic behavior of CLT, we suggest in this chapter closed-form expressions of the equivalent layer stiffness depending on the sawing pattern of the board and the local mechanical characteristics. First in Section 1.2.1 equivalent layer stiffness is calculated from the average of the local stiffness and compliance matrix in all directions of the radial-tangential plane. Then in Section 1.2.2, a finer estimation of the equivalent layer stiffness is established using Reuss lower bound and Voigt upper bound for varying sawing pattern. An application to Norway Spruce boards with varying sawing pattern is presented in Section 1.3 for boards with glued edges. In order to extrapolate these results to boards with free edges, the impact of edge gluing on the equivalent layer stiffness is first discussed in Section 1.4. Then, using finite element method, we calculate upper bounds for the cross-layer shear stiffness  $G_{CZ}$  of boards with and without glued edges.

## 1.2 Closed-form expressions for the equivalent layer stiffness

In this section, the equivalent layer stiffness is estimated from local behavior of wood using averaging techniques. The equivalent behavior of the board is expressed in the global orthotropic system ( $O, L, C, Z$ ) of the board (Figure 1.1).

### 1.2.1 Stiffness and compliance averages

For a given board, the sawing pattern is not known a priori. A first approximation of the global behavior can be obtained by averaging the local behavior in all directions of the radial-tangential plane  $(O, R, T)$ . For this purpose, the constitutive relationship between the local strain  $\varepsilon$  and the local stress  $\sigma$  is written using Kelvin's notation in the  $(O, L, R, T)$  frame:

$$\begin{pmatrix} \varepsilon_L \\ \varepsilon_R \\ \varepsilon_T \\ \sqrt{2}\varepsilon_{RT} \\ \sqrt{2}\varepsilon_{LT} \\ \sqrt{2}\varepsilon_{LR} \end{pmatrix} = \begin{pmatrix} S_{11} & S_{12} & S_{13} & 0 & 0 & 0 \\ S_{12} & S_{22} & S_{23} & 0 & 0 & 0 \\ S_{13} & S_{23} & S_{33} & 0 & 0 & 0 \\ 0 & 0 & 0 & S_{44} & 0 & 0 \\ 0 & 0 & 0 & 0 & S_{55} & 0 \\ 0 & 0 & 0 & 0 & 0 & S_{66} \end{pmatrix} \begin{pmatrix} \sigma_L \\ \sigma_R \\ \sigma_T \\ \sqrt{2}\sigma_{RT} \\ \sqrt{2}\sigma_{LT} \\ \sqrt{2}\sigma_{LR} \end{pmatrix}, \quad (1.1)$$

where  $\mathbf{S}$  is the three-dimensional compliance matrix of the local orthotropic material. Considering local Young moduli  $E$ , shear moduli  $G$  and Poisson's ratio  $\nu$ , components of the three-dimensional compliance matrix  $\mathbf{S}$  are expressed as:

$$\begin{aligned} S_{11} &= \frac{1}{E_L}, & S_{12} &= -\frac{\nu_{LR}}{E_L}, & S_{13} &= -\frac{\nu_{LT}}{E_L}, \\ S_{22} &= \frac{1}{E_R}, & S_{23} &= -\frac{\nu_{RT}}{E_R}, & S_{33} &= \frac{1}{E_T}, \\ S_{44} &= \frac{1}{2G_{RT}}, & S_{55} &= \frac{1}{2G_{LT}}, & S_{66} &= \frac{1}{2G_{LR}}. \end{aligned} \quad (1.2)$$

With Kelvin's notation, the rotation matrix  $\mathbf{R}$  around longitudinal axis  $L$  by an angle  $\theta$  (Figure 1.1) is defined as:

$$\mathbf{R}(\theta) = \begin{pmatrix} 1 & 0 & 0 & 0 & 0 & 0 \\ 0 & c^2 & s^2 & \sqrt{2}cs & 0 & 0 \\ 0 & s^2 & c^2 & -\sqrt{2}cs & 0 & 0 \\ 0 & -\sqrt{2}cs & \sqrt{2}cs & c^2 - s^2 & 0 & 0 \\ 0 & 0 & 0 & 0 & c & -s \\ 0 & 0 & 0 & 0 & s & c \end{pmatrix},$$

where  $c = \cos(\theta)$  and  $s = \sin(\theta)$ . The compliance tensor  $\mathbf{S}(\theta)$  after rotation by an angle  $\theta$  is given by:

$$\mathbf{S}(\theta) = \mathbf{R}(\theta) \cdot \mathbf{S} \cdot {}^t\mathbf{R}(\theta). \quad (1.3)$$

The average of the compliance matrix  $\mathbf{S}(\theta)$  in the domain  $\theta \in [0, 2\pi]$  gives a compliance matrix  $\bar{\mathbf{S}}$  corresponding to a transversely isotropic material:

$$\bar{\mathbf{S}} = \begin{pmatrix} \bar{S}_{11} & \bar{S}_{12} & \bar{S}_{12} & 0 & 0 & 0 \\ \bar{S}_{12} & \bar{S}_{22} & \bar{S}_{22} - \bar{S}_{44} & 0 & 0 & 0 \\ \bar{S}_{12} & \bar{S}_{22} - \bar{S}_{44} & \bar{S}_{22} & 0 & 0 & 0 \\ 0 & 0 & 0 & \bar{S}_{44} & 0 & 0 \\ 0 & 0 & 0 & 0 & \bar{S}_{66} & 0 \\ 0 & 0 & 0 & 0 & 0 & \bar{S}_{66} \end{pmatrix}, \quad (1.4)$$

where

$$\begin{cases} \bar{S}_{11} = S_{11}, \\ \bar{S}_{12} = \frac{1}{2}(S_{12} + S_{13}), \\ \bar{S}_{22} = \frac{1}{8}[3(S_{22} + S_{33}) + 2(S_{23} + S_{44})], \\ \bar{S}_{44} = \frac{1}{4}(S_{22} + S_{33} + 2(S_{44} - S_{23})), \\ \bar{S}_{66} = \frac{1}{2}(S_{55} + S_{66}). \end{cases} \quad (1.5)$$

This average compliance  $\bar{\mathbf{S}}$  defines hence apparent moduli of a transversely isotropic elastic behavior. Let  $E^S$ ,  $G^S$  and  $\nu^S$  denote the Young moduli, shear moduli and Poissons ratios from the averaged compliance. They are defined by the following expressions:

$$\begin{cases} E_L^S = \frac{1}{\bar{S}_{11}} = E_L, \\ E_N^S = \frac{1}{\bar{S}_{22}} = 8 \left( \frac{3-\nu_{RT}}{E_R} + \frac{3-\nu_{TR}}{E_T} + \frac{1}{G_{RT}} \right)^{-1}, \\ \nu_{LN}^S = -\frac{\bar{S}_{12}}{\bar{S}_{11}} = \frac{\nu_{LT} + \nu_{LR}}{2}, \\ G_{LN}^S = \frac{1}{2\bar{S}_{66}} = \left( \frac{1}{2G_{LR}} + \frac{1}{2G_{LT}} \right)^{-1}, \\ G_{NN}^S = \frac{1}{2\bar{S}_{44}} = 2 \left( \frac{1}{G_{RT}} + \frac{1+\nu_{RT}}{2E_R} + \frac{1+\nu_{TR}}{2E_T} \right)^{-1}. \end{cases} \quad (1.6)$$

Since there is no distinction here between cross and normal directions  $C$  and  $Z$  of the board, the notation  $N$  is used for the normal directions of the board.

In the following, the three-dimensional stiffness matrix  $\mathbf{C}(\theta) = \mathbf{S}^{-1}(\theta)$  is averaged in all directions of the radial tangential plane. Since Kelvin's notations are used here, the same rotation matrix  $\mathbf{R}(\theta)$  is used to calculate the stiffness matrix  $\mathbf{C}$  leading to similar results. The averaged stiffness matrix  $\bar{\mathbf{C}}$  also correspond to a transversely

## 1.2. CLOSED-FORM EXPRESSIONS FOR THE EQUIVALENT LAYER STIFFNESS

isotropic material:

$$\bar{\mathbf{C}} = \begin{pmatrix} \bar{C}_{11} & \bar{C}_{12} & \bar{C}_{12} & 0 & 0 & 0 \\ \bar{C}_{12} & \bar{C}_{22} & \bar{C}_{22} - \bar{C}_{44} & 0 & 0 & 0 \\ \bar{C}_{12} & \bar{C}_{22} - \bar{C}_{44} & \bar{C}_{22} & 0 & 0 & 0 \\ 0 & 0 & 0 & \bar{C}_{44} & 0 & 0 \\ 0 & 0 & 0 & 0 & \bar{C}_{66} & 0 \\ 0 & 0 & 0 & 0 & 0 & \bar{C}_{66} \end{pmatrix}, \quad (1.7)$$

where

$$\begin{cases} \bar{C}_{11} = C_{11}, \\ \bar{C}_{12} = \frac{1}{2}(C_{12} + C_{13}), \\ \bar{C}_{22} = \frac{1}{8}[3(C_{22} + C_{33}) + 2(C_{23} + C_{44})], \\ \bar{C}_{44} = \frac{1}{4}(C_{22} + C_{33} + 2(C_{44} - C_{23})), \\ \bar{C}_{66} = \frac{1}{2}(C_{55} + C_{66}). \end{cases} \quad (1.8)$$

The transversely isotropic elastic behavior calculated from the stiffness average is not the same as the transversely isotropic elastic behavior calculated from the compliance average:  $\bar{\mathbf{C}} \neq \bar{\mathbf{S}}^{-1}$ . Another equivalent transversely isotropic elastic behavior can thus be defined from the average stiffness  $\bar{\mathbf{C}}$ . To obtain engineering characteristics such as Young moduli and Poisson's ratios, one need first to calculate  $\bar{\mathbf{C}}^{-1}$  and then identify engineering moduli as previously (1.6). Note here that only the longitudinal shear stiffness has a simple expression:

$$G_{LN}^C = \frac{1}{2}(G_{LR} + G_{LT}).$$

### 1.2.2 Reuss lower bound and Voigt upper bound for varying sawing pattern

One can then go further in the estimation of average properties, based on the geometry of boards. Indeed, assuming an equivalent layer with glued narrow edges, it is possible to derive bounds taking explicitly the board aspect ratio and the relative distance to the pith into account. The Reuss lower bound compliance matrix  $\mathbf{S}^R$  is the average of the local compliance matrix  $\mathbf{S}(\theta)$ , where  $\theta$  is the ring orientation (Figure 1.2), over the full board section. Averaging the compliance matrix is equivalent to assume a uniform stress state  $\sigma$  over the whole section. Taking into account boards dimensions,  $\mathbf{S}^R$  can be expressed as:

$$\mathbf{S}^R = \frac{1}{4bt} \int_{-b}^b \int_{-t}^t \mathbf{S}(\theta) dC dZ. \quad (1.9)$$

First, bounds are calculated for a centered sawing pattern with a null distance to

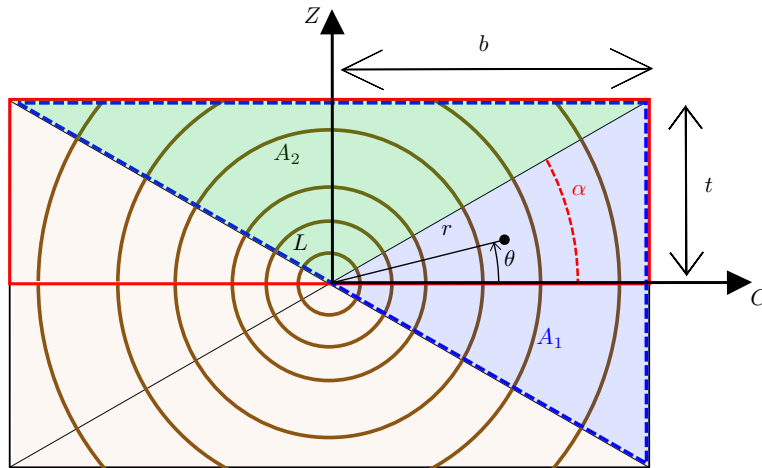


Figure 1.2 – Scheme of the board section

the pith as the rectangular red section in Figure 1.2, close to the actual sawing pattern of boards (Figure 1.1). Note that for symmetry reasons,  $S(\theta) = S(\pi + \theta)$ . Hence, Reuss and Voigt bounds of the centered sawing pattern can be simplified to:

$$\mathbf{S}^R = \frac{1}{A_1 + A_2} \left( \int_{A_1} \mathbf{S}(\theta) dA + \int_{A_2} \mathbf{S}(\theta) dA \right), \quad (1.10)$$

where  $A_1$  and  $A_2$  are blue and green triangular domains in Figure 1.2. Furthermore, the board having always an axis of symmetry ensures that the effective behavior is orthotropic.

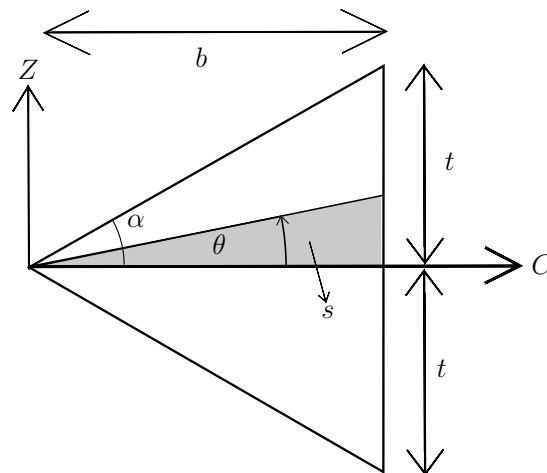


Figure 1.3 – Integration of mechanical properties on  $A_1$

## 1.2. CLOSED-FORM EXPRESSIONS FOR THE EQUIVALENT LAYER STIFFNESS

In Figure 1.3, geometrical parameters used for the integration of mechanical properties on the section  $A_1$  are presented. For an angle  $\theta$ , the area is  $s = \frac{b^2}{2} \tan \theta$  and the elementary area is then  $ds = \frac{b^2}{2} \frac{d\theta}{\cos^2 \theta}$ . In (1.3),  $\mathcal{S}(\theta)$  is expressed as a sum of power function of sinus and cosinus functions weighted by local mechanical properties  $S_{ij}$ . These functions have to be integrated on the section  $A_1$  for  $\theta \in [-\alpha; \alpha]$ . For example:

$$\int_{-\alpha}^{\alpha} \cos^4(\theta) ds = \frac{b^2}{2} \int_{-\alpha}^{\alpha} \cos^2(\theta) d\theta = \frac{b^2}{2} (\cos \alpha \sin \alpha + \alpha).$$

The integration on  $A_2$  is similar to the integration on  $A_1$  considering the change of variable  $\theta' = \theta - \frac{\pi}{2}$  varying between  $-\alpha'$  and  $\alpha' = \frac{\pi}{2} - \alpha$ . The elementary area is then  $ds' = \frac{t^2}{2} \frac{d\theta'}{\cos^2 \theta'}$ . For example:

$$\int_{\alpha}^{\pi-\alpha} \cos^4(\theta) ds' = b^2 \tan^2 \alpha \left[ \frac{1}{\tan \alpha} + \frac{1}{2} \cos \alpha \sin \alpha - \frac{3}{2} \left( \frac{\pi}{2} - \alpha \right) \right].$$

$\langle \bullet \rangle$  is defined as the average of  $\bullet$  over the whole section of the board. From previous results, it is possible to determine the average  $\langle \cos^4(\theta) \rangle$  on the entire section:

$$\langle \cos^4(\theta) \rangle = \frac{1}{4} [3 - f(\alpha) + 2h(\alpha)],$$

where:

$$f(\alpha) = \frac{\alpha}{\tan \alpha} + \left( \frac{\pi}{2} - \alpha \right) \tan \alpha \quad \text{and} \quad h(\alpha) = \frac{\alpha}{\tan \alpha} - \left( \frac{\pi}{2} - \alpha \right) \tan \alpha.$$

Proceeding the same way for all functions  $s^4$ ,  $c^2 s^2$ ,  $c^2$  and  $s^2$  and including them in the expression of  $\mathcal{S}(\theta)$  (1.3), it is possible to express the Reuss lower bound  $\mathcal{S}^R(\alpha)$  as an

orthotropic material function of  $\alpha$  and local mechanical properties:

$$\left\{ \begin{array}{l} S_{11}^R(\alpha) = S_{11}, \quad (1.11a) \\ S_{12}^R(\alpha) = \frac{1}{2} [S_{12} + S_{13} + (S_{12} - S_{13}) h(\alpha)], \quad (1.11b) \\ S_{13}^R(\alpha) = \frac{1}{2} [S_{12} + S_{13} + (S_{13} - S_{12}) h(\alpha)], \quad (1.11c) \\ S_{22}^R(\alpha) = \frac{1}{4} \left[ \begin{array}{l} 3(S_{22} + S_{33}) - 2(S_{23} + S_{44}) + 2(S_{22} - S_{33}) h(\alpha) \\ + (2S_{23} + 2S_{44} - S_{22} - S_{33}) f(\alpha) \end{array} \right], \quad (1.11d) \\ S_{33}^R(\alpha) = \frac{1}{4} \left[ \begin{array}{l} 3(S_{22} + S_{33}) - 2(S_{23} + S_{44}) + 2(S_{33} - S_{22}) h(\alpha) \\ + (2S_{23} + 2S_{44} - S_{22} - S_{33}) f(\alpha) \end{array} \right], \quad (1.11e) \\ S_{23}^R(\alpha) = \frac{1}{4} \left[ \begin{array}{l} 6S_{23} + 2S_{44} - S_{22} - S_{33} \\ + (S_{22} + S_{33} - 2S_{23} - 2S_{44}) f(\alpha) \end{array} \right], \quad (1.11f) \\ S_{44}^R(\alpha) = \frac{1}{2} \left[ \begin{array}{l} 2S_{23} + 4S_{44} - S_{22} - S_{33} \\ + (S_{22} + S_{33} - 2S_{23} - 2S_{44}) f(\alpha) \end{array} \right], \quad (1.11g) \\ S_{55}^R(\alpha) = \frac{1}{2} [S_{55} + S_{66} + (S_{55} - S_{66}) h(\alpha)], \quad (1.11h) \\ S_{66}^R(\alpha) = \frac{1}{2} [S_{55} + S_{66} + (S_{66} - S_{55}) h(\alpha)]. \quad (1.11i) \end{array} \right.$$

This approach may easily be extended taking into account the distance  $z_1$  to the pith (Figure 1.4). The Reuss lower bound of the equivalent layer stiffness of the board delimited by the red rectangle in Figure 1.4 can then be calculated as following thanks to the additivity of the integral:

$$\mathbf{S}^R(\alpha, z_1) = \frac{z_2 \mathbf{S}^R(\alpha_2) - z_1 \mathbf{S}^R(\alpha_1)}{t}, \quad (1.12)$$

where  $t = z_1 - z_2$  is the thickness of the board. Note that  $\mathbf{S}^R(\alpha, 0) = \mathbf{S}^R(\alpha)$ .

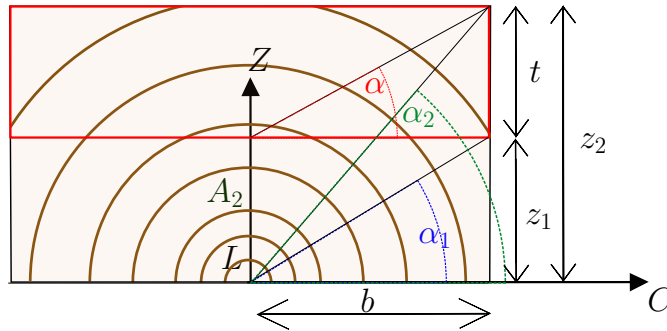


Figure 1.4 – Scheme of the board section with a distance  $z_1$  to the pith

## 1.2. CLOSED-FORM EXPRESSIONS FOR THE EQUIVALENT LAYER STIFFNESS

Moreover, this approach may also be extended taking into account an asymmetric sawing pattern with a lateral distance  $c_1$  to the symmetry axis (Figure 1.5). Nevertheless, the equivalent stiffness of this board is not orthotropic since there is no symmetry axis in the radial-tangential plane. In order to compensate this effect, it is possible to use the board symmetric to the first one (dotted in Figure 1.5) in the arrangement of the layer. Then, the Reuss lower bound  $S_{\text{sym}}^R$  and the Voigt upper bound  $C_{\text{sym}}^V$  of the arrangement of the two boards symmetric with respect to each other can be calculated by:

$$\mathbf{S}_{\text{sym}}^R(\alpha, z_1, c_1) = \frac{c_2 z_2 \mathbf{S}^R(\alpha_2) - c_2 z_1 \mathbf{S}^R(\alpha_1) - c_1 z_2 \mathbf{S}^R(\alpha_3) + c_1 z_1 \mathbf{S}^R(\alpha_4)}{2bt}. \quad (1.13)$$

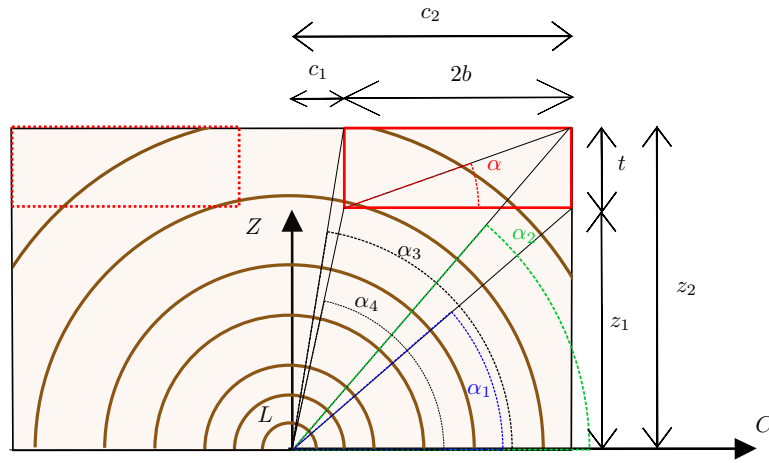


Figure 1.5 – Scheme of the board section with a distance  $z_1$  to the pith

From the expression of the Reuss lower bound of the compliance stiffness  $S^R$ , the engineering constants of the associated orthotropic material can be calculated with the following expressions:

$$\begin{cases} E_L^R = \frac{1}{S_{11}^R}, & E_C^R = \frac{1}{S_{22}^R}, & E_Z^R = \frac{1}{S_{33}^R}, \\ \nu_{LC}^R = \frac{S_{12}^R}{S_{11}^R}, & \nu_{LZ}^R = \frac{S_{13}^R}{S_{11}^R}, & \nu_{CZ}^R = \frac{S_{23}^R}{S_{22}^R}, \\ G_{LC}^R = \frac{1}{2S_{66}^R}, & G_{LZ}^R = \frac{1}{2S_{55}^R}, & G_{CZ}^R = \frac{1}{2S_{44}^R}. \end{cases} \quad (1.14)$$

Since Kelvin's notation are used, similar expression are found for the stiffness matrix  $C^V$  of the Voigt upper bound, corresponding to the average of the stiffness matrix  $C(\theta)$  over the board section, replacing  $S$  by  $C$  in (1.9,1.10,1.11,1.12,1.13). Averaging the stiffness matrix is equivalent to assume a uniform strain state  $\varepsilon$  over the whole section. Similarly to what has been done for the average in all directions (1.6), the stiffness matrix  $S^V = (C^V)^{-1}$  is introduced. Then, the engineering constants associated with

the Voigt upper bound are calculated from (1.14) by replacing the superscript  $R$  by  $V$ . Again  $\mathbf{S}^V \neq \mathbf{S}^R$ .

Let us recall that,  $\frac{1}{2}{}^t\varepsilon \cdot \mathbf{C}^V \cdot \varepsilon$  is an upper bound of the equivalent strain energy of the board for any uniform strain  $\varepsilon$  and  $\sigma \cdot \mathbf{S}^R \cdot \sigma$  is an upper bound of the equivalent stress energy for any uniform stress  $\sigma$  where  $\frac{1}{2}{}^t\varepsilon$  and  ${}^t\sigma$  stand for transpose vectors of  $\varepsilon$  and  $\sigma$ . Nevertheless, some individual engineering constants calculated from these bounds are not always bounds of the corresponding homogenized engineering constants of the board since they are sometimes coupled with other components of  $\mathbf{C}^V$  and  $\mathbf{S}^R$ . Particularly, Young moduli  $E^V$  of the Voigt upper bounds are no upper bounds of the actual Young moduli of the board. On the contrary, Young moduli  $E^R$  are lower bounds of the actual Young moduli since they are isolated in diagonal components of the matrix  $\mathbf{S}^R$  (1.2). Similarly,  $G^R$  and  $G^V$  are lower and upper bounds of the actual shear stiffness of the board.

### 1.3 Equivalent-layer stiffness of Norway-Spruce

An application of preceding formulas is made to estimate the equivalent layer stiffness of boards with glued edges from the local behavior at ring scale measured by (Keunecke et al., 2007, 2008) on Norway Spruce (Table 1.1). Only sawing pattern of boards including an axis of symmetry are studied (1.12).

	$E_L$	$E_R$	$E_T$	$G_{LR}$	$G_{LT}$	$G_{RT}$	$\nu_{LR}$	$\nu_{LT}$	$\nu_{RT}$
Value (MPa)	12,800	625	397	617	587	53	0.36	0.45	0.48
CoV (%)	9.2	20.4	10.3	12.1	10.2	10.9	13.2	8.2	19.2
Num. of specimen	10	13	11	120	120	120	10	10	13

Table 1.1 – Elastic Properties of Norway Spruce (Keunecke et al., 2007, 2008)

#### 1.3.1 Equivalent Young moduli

##### 1.3.1.1 Equivalent longitudinal Young modulus $E_L$

The equivalent longitudinal Young modulus  $E_L$  is a important characteristics of the CLT behavior particularly under bending and under in-plane load. The Reuss bound  $E_L^R$  of the equivalent longitudinal modulus is equal to the local longitudinal modulus  $E_L$  for any sawing pattern (see 1.14). The equivalent longitudinal modulus  $E_L^V$  estimated numerically from the Voigt upper bound is almost equal to the Reuss bound for varying sawing patterns: the relative difference is lower than 0.2‰ for  $\frac{b}{t} < 10$  and  $\frac{z_1}{b} < 3$ . This is a consequence of the high stiffness contrast between  $E_L$  and  $E_R$  and  $E_T$ . Thus the

### 1.3. EQUIVALENT-LAYER STIFFNESS OF NORWAY-SPRUCE

sawing pattern of boards is indifferent in practice regarding the equivalent longitudinal Young modulus  $E_L$  of CLT with glued edges .

#### 1.3.1.2 Equivalent normal and cross Young moduli $E_Z$ and $E_C$

The equivalent normal Young modulus  $E_Z$  has only a limited role in the behavior of CLT panels: it plays a role mostly when the CLT panel is placed between two vertical elements and is locally punched. In Figure 1.6,  $E_Z$  calculated from Reuss and Voigt bounds for varying board aspect ratio  $\frac{2b}{t}$  and for varying relative distance to the pith  $\frac{z_1}{2b}$ . It is observed that  $E_Z$  vary strongly between 620 MPa and 230 MPa which is approximately one third of the local radial modulus  $E_R$ . It is minimum for a relative distance to the pith  $\frac{z_1}{2b}$  between 0.2 and 0.4 and a board aspect ratio  $\frac{2b}{t} > 4$  which corresponds to common sawing patterns used for cross-layer. Using directly local moduli  $E_R$  and  $E_T$  in applications may overestimate the equivalent moduli of 200% to 274%.

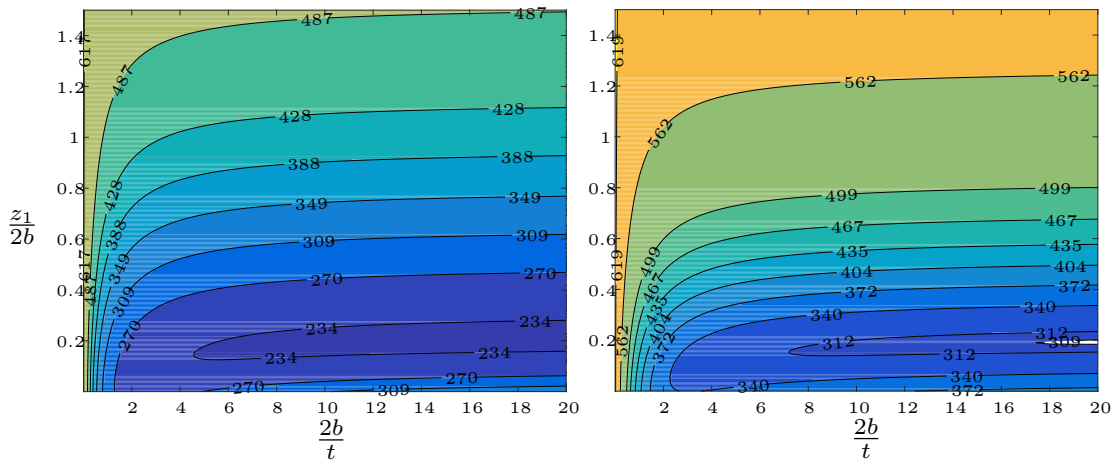


Figure 1.6 – Reuss lower bound (left) and Voigt upper bound (right) for the estimation of  $E_Z$  (MPa)

The equivalent cross Young modulus  $E_C$  is involved in the calculation of the bending and membrane stiffness. In Figure 1.7, the equivalent cross Young modulus  $E_C$  calculated from Reuss and Voigt bounds is plotted for varying board aspect ratio  $\frac{2b}{t}$  and for varying relative distance to the pith  $\frac{z_1}{2b}$ . It is observed that the equivalent cross Young modulus  $E_C$  varies strongly with the sawing pattern. It can be equal to 220 MPa which is almost three times lower than the local Young modulus  $E_R$ . This value is in contradiction with what is suggested in current recommendations for a revised version of the Eurocode 5.1.1 (European Committee for Standardisation, 24-02-2016) where a value of 450 MPa is suggested which could underestimate deformations due to cross layers.

Note, however, that  $E_C$  is generally negligible compared to  $E_L$  in the calculation of the bending and membrane stiffness of CLT.

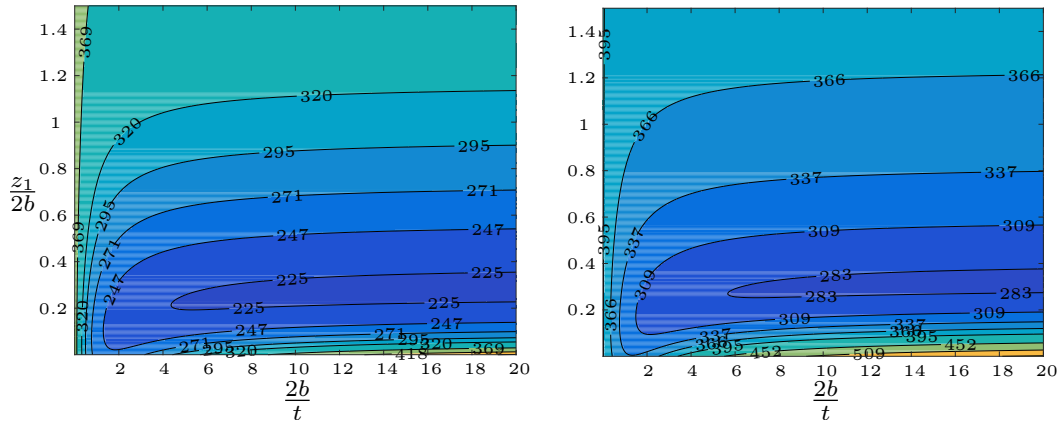


Figure 1.7 – Reuss lower bound (left) and Voigt upper bound (right) for the estimation of  $E_C$  (MPa)

In Figure 1.8, the equivalent cross and normal Young moduli  $E_C^R$ ,  $E_C^V$ ,  $E_Z^R$  and  $E_Z^V$  are compared to the compliance average  $E_N^S$  and the stiffness average  $E_N^C$ . As expected, for  $\alpha = \arctan \frac{t}{b}$  close to  $0^\circ$  and  $90^\circ$ , the bounds tend to the local behavior since the ring orientation is almost uniform in the section: local orientations coincide with the global orientations. It is further observed that for  $\alpha$  between  $30^\circ$  and  $60^\circ$ , equivalent Young moduli of Voigt and Reuss bounds can be approximated directly by moduli from averages in stiffness  $E_N^C$  and in compliance  $E_N^S$ .

### 1.3.1.3 Poisson's ratio $\nu_{LC}$ and $\nu_{CL}$

In current recommendations (Thiel, 2013; Stora Enso, 2014), the bending stiffness  $D$  of longitudinal layers in CLT is considered proportional to  $E_L$  and not to  $\frac{E_L}{1-\nu_{LC}\nu_{CL}}$  as should be done in Classical Lamination Theory. From Reuss and Voigt bounds, the Poisson's ratios product  $\nu_{LC}\nu_{CL}$  varies between 0.003 to 0.007. Then the assumption of  $E_L \approx \frac{E_L}{1-\nu_{LC}\nu_{CL}}$  is valid for CLT panels.

### 1.3.2 Equivalent shear moduli

Because of the orthotropy of the equivalent layer stiffness, each shear modulus can be studied separately and shear stiffness calculated from Reuss and Voigt bounds are true bounds of the actual equivalent layer shear stiffness.

### 1.3. EQUIVALENT-LAYER STIFFNESS OF NORWAY-SPRUCE

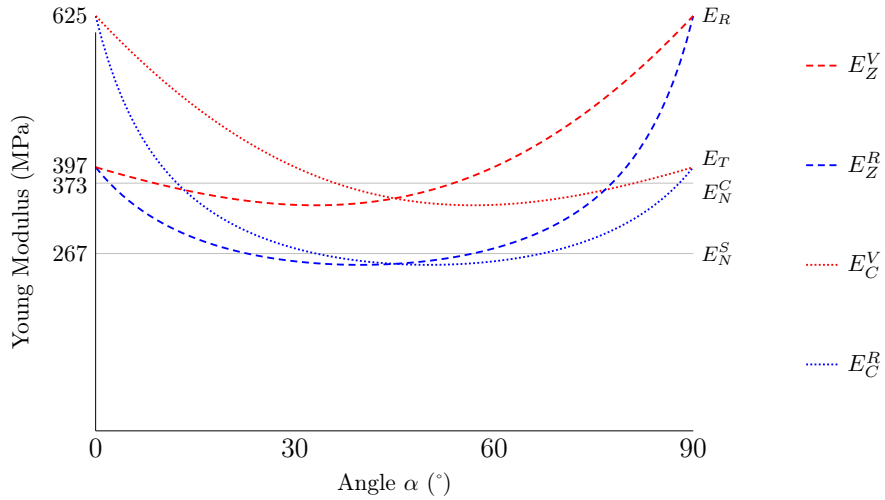


Figure 1.8 – Young moduli of Voigt and Reuss bounds for  $z_1 = 0$

#### 1.3.2.1 Equivalent longitudinal-layer and in-plane shear moduli $G_{LZ}$ and $G_{LC}$

From calculations, it is checked that for varying board aspect ratio  $\frac{2b}{t}$  and relative distance to the pith  $\frac{z_1}{2b}$ , the gap between bounds of the longitudinal-layer shear modulus  $G_{LZ}$  and the in-plane shear modulus  $G_{LC}$  is less than 0.1%. Furthermore that  $G_{LZ}$  and  $G_{LC}$  vary slightly between values of local shear moduli  $G_{LR} = 617$  MPa and  $G_{LT} = 587$  MPa since  $G_{LR} \approx G_{LT}$ . Finally, for glued narrow edges, we checked that stiffness and compliance averaged  $G_{NN}^S \approx G_{NN}^C = 602$  MPa are good approximations of  $G_{LR}$  and  $G_{LT}$  for CLT with glued narrow edges.

#### 1.3.3 Equivalent cross-layer shear stiffness $G_{CZ}$

In Figure 1.9, Reuss and Voigt bounds of equivalent layer shear stiffness  $G_{CZ}$  are plotted for varying board aspect ratio  $\frac{2b}{t}$  and for relative distance to the pith  $\frac{z_1}{2b}$ . It is observed that if the board aspect ratio is large enough, there is a sawing pattern, corresponding to a relative distance to the pith  $0.2 < \frac{z_1}{2b} < 0.3$ , which maximizes  $G_{CZ}$ . For these boards, the equivalent cross layer shear stiffness lies between 100 and 150 MPa approximately which is twice to three times higher than the local rolling shear stiffness  $G_{RT}$ . These values were assessed by experiments for CLT with glued narrow edges in Chapter 2 at board scale.

In this section, upper and lower bounds have been calculated for boards with glued edges. These bounds are also valid for any assembly of identical boards such as GLT. Nevertheless, most of CLT manufacturers do not glue narrow edges. Hence, free narrow edges effects, which are specific to CLT, are discussed in the following section.

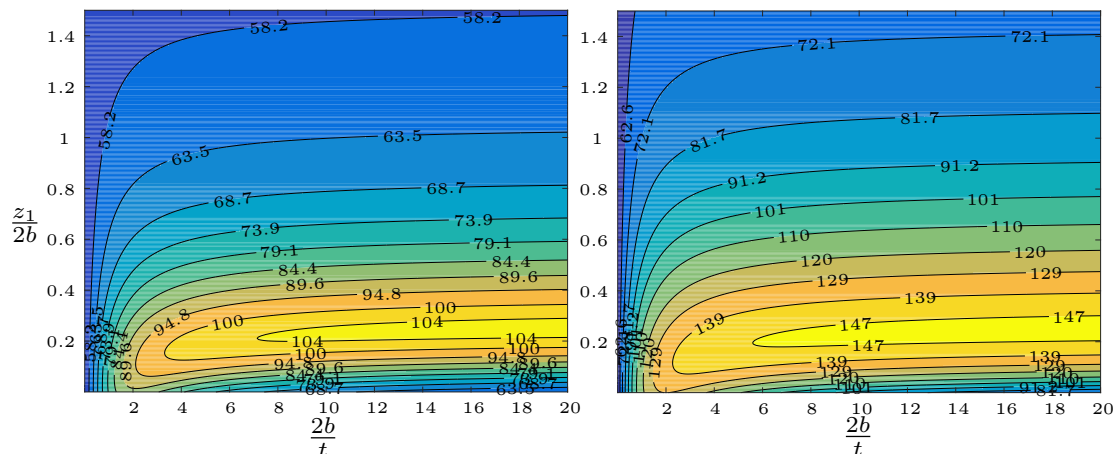


Figure 1.9 – Reuss lower bound (left) and Voigt upper bound (right) for the estimation of  $G_{CZ}$  (MPa)

## 1.4 Influence of the free narrow edges on cross-layer shear stiffness $G_{CZ}$

In this section, we discuss the impact of free narrow edges on the global behavior of CLT compared to results of Section 1.3. The free narrow edges boundary condition imposes  $\sigma_{CC} = \sigma_{LC} = \sigma_{CZ} = 0$  on narrow edges. Since a uniform strain is assumed for the Voigt upper bound calculation,  $\mathbf{C}^V$  is also an upper bound of CLT with free edges. In contrast, these conditions are not always compatible with the uniform stress assumption in the Reuss lower bound calculation. Longitudinal Young modulus  $E_L^R$ , normal Young modulus  $E_Z^R$  and the longitudinal shear modulus  $G_{LZ}$  are calculated assuming uniform stress  $\sigma_{LL}$ ,  $\sigma_{ZZ}$  and  $\sigma_{LZ}$  which are compatible with the free narrow edges boundary condition.  $E_L^R$ ,  $E_Z^R$  and  $G_{LZ}$  are also lower bounds of the corresponding homogenized engineering constants for CLT with free narrow edges and the results obtained in the previous section still hold for these moduli. Nonetheless, the equivalent cross Young modulus  $E_C^R$ , the equivalent in-plane shear modulus  $G_{LC}^R$  and the equivalent cross-layer shear modulus  $G_{CZ}^R$  are calculated from an assumption of uniform stress  $\sigma_{CC}$ ,  $\sigma_{LC}$  and  $\sigma_{CZ}$  over the whole section. Hence,  $E_C^R$ ,  $G_{LC}^R$  and  $G_{CZ}^R$  are no lower bounds of the corresponding homogenized engineering constants for CLT with free narrow edges.

Even if  $G_{LZ} \approx G_{LC}$  for glued narrow edges, they are involved in different mechanisms:  $G_{LZ}$  contributes to the global transverse shear behavior whereas  $G_{LC}$  plays a central role for the in-plane shear behavior of CLT panels. For CLT with free narrow edges, the in-plane shear and torsion behavior, depending on  $G_{LC}$ , is more complex than for glued edges. Indeed, in-plane shear stress cannot be transferred directly to the neighbouring board because of free edges (Silly, 2010). The behaviour is thus intrinsically

3D and stiffness can only be estimated considering a superposition of layers (which is beyond the scope of this chapter). In particular, Moosbrugger et al. (2006) studied the in-plane shear behavior of an infinitely thick CLT with regular gaps between neighbouring boards. They observed a significant decrease of the apparent in-plane shear modulus  $G_{LC}$  up to half that estimated for boards with glued edges. These results were compared later to 3-ply and 5-ply CLT by Bogensperger et al. (2010). Sebera et al. (2015) tested full scale CLT panels subjected to torsion and compared it with finite elements results. Strong discontinuities are observed for CLT with free narrow edges. Franzoni et al. (2017a,b) also studied the behavior of CLT with regular large gaps.

Similarly to the in-plane shear behavior, a 3D study is necessary for the equivalent cross Young modulus  $E_C$  since stress cannot be transmitted directly from one board to the other.

In the following, we focus on the impact of free narrow edges on the cross-layer shear stiffness  $G_{CZ}$  since it is an important parameter in the design of CLT.

### 1.4.1 Presentation of the numerical model

Here, we present a numerical finite elements study to compute an upper bound of the equivalent cross-layer shear stiffness  $G_{CZ}$  of wooden boards with glued and free edges. In literature, several similar studies have already been performed (Aicher and Dill-Langer, 2000; Jakobs et al., 2005) but only for free narrow edges.

This is achieved assuming that the cross-layer is sheared by the relative displacement of the adjacent longitudinal layer. Since strain is imposed, the cross-layer shear stiffness  $G_{CZ}^{\text{num}}$  calculated numerically is an upper bound of  $G_{CZ}$ . This upper bound is more precise than Voigt upper bound since displacement conditions are imposed only on the boundary whereas a uniform strain condition is imposed in the whole board for the Voigt upper bound.

In (Aicher and Dill-Langer, 2000; Jakobs et al., 2005), the cross-layer is modeled as well as the longitudinal adjacent layer (Figure 1.10). Because of the stiffness contrast between layers, this model is almost equivalent to impose directly displacement conditions on upper and lower faces of the cross-layer. Moreover, Lebée and Sab (2012) demonstrated that it is possible to isolate the core of a sandwich, here the cross-layer, from the skins, here the longitudinal layers and to obtain an upper bound of the cross-layer shear stiffness by imposing a relative displacement between upper and lower faces. Then, in the following, we extend the study to boards with glued narrow edges and compare these results to boards with free narrow edges.

The cross-layer is assumed to be infinite with an alternative orientation of the sawing patterns (Figure 1.11). Then, for glued narrow edges, a representative volume element (RVE) can be modeled as two adjacent boards. It is then possible to consider symmetry effects to reduce the problem to only two half board sections (Figure 1.11)

CHAPTER 1. EQUIVALENT LAYER STIFFNESS OF CLT: CLOSED-FORM BOUNDS AND NUMERICAL VALIDATION

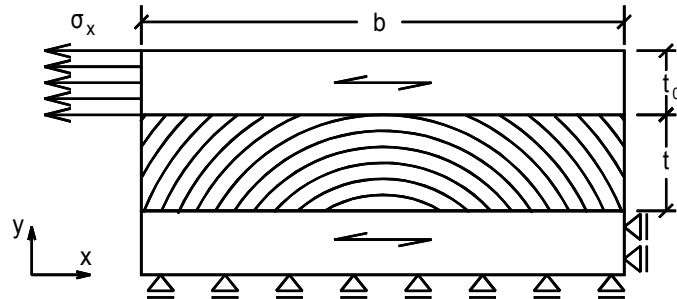


Figure 1.10 – 2D numerical simulation for calculation of the equivalent cross-layer shear stiffness (Aicher and Dill-Langer, 2000)

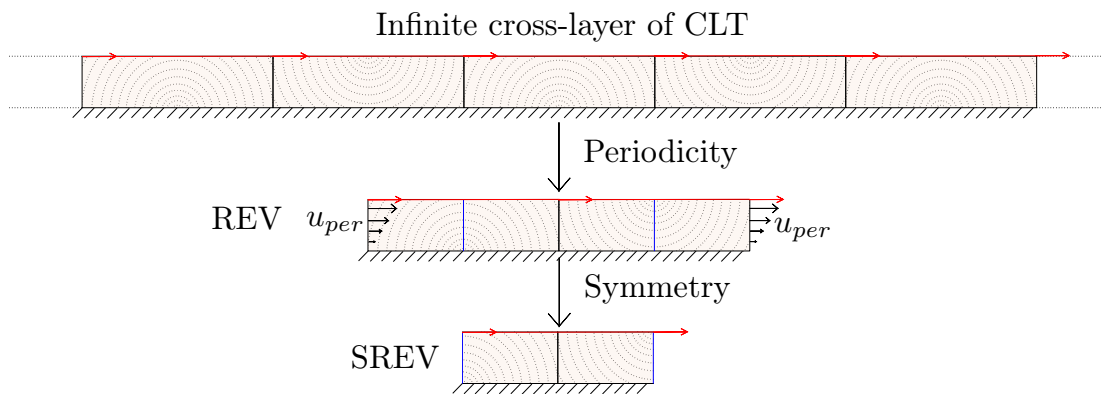


Figure 1.11 – Simplification of the model because of periodicity and symmetries

## 1.4. INFLUENCE OF THE FREE NARROW EDGES ON CROSS-LAYER SHEAR STIFFNESS $G_{CZ}$

called Sub-Representative Volume Element (SREV). Consequently, symmetry conditions are imposed on lateral sections for board with glued edges (Figure 1.12). For free edges, only one half boards is represented with one free boundary condition and one symmetry condition as shown in Figure 1.13. Finally, for each board, the local orientations of timber is varying according to the given sawing pattern.

Here, in-plane deformations are assumed in the board, a 2D numerical simulation is then performed.

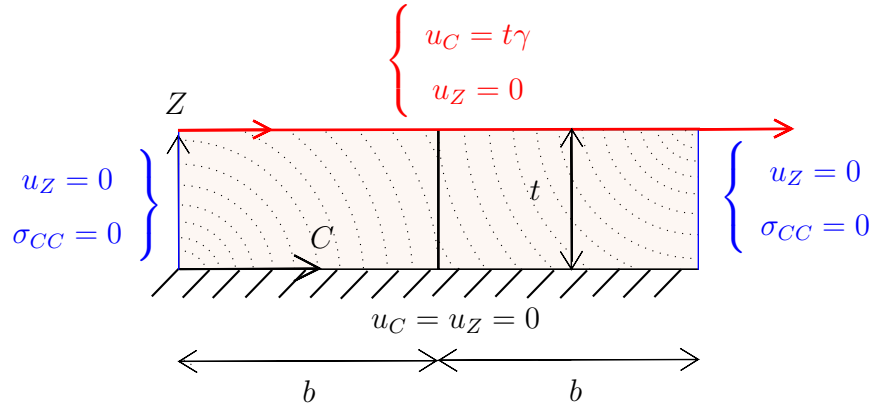


Figure 1.12 – 2D numerical simulation for calculation of the equivalent cross-layer shear stiffness of CLT with glued edges

The equivalent cross-layer shear stiffness  $G_{CZ}$  can be estimated from the strain energy in the board  $W_{\text{ela}}$ :

$$W_{\text{ela}} = \frac{1}{2} G_{CZ} \gamma^2 b t,$$

where  $\gamma = 2\varepsilon_{LC} = \frac{u_C}{t}$  is the averaged shear strain in the specimen.

### 1.4.2 Discussion

Voigt upper bound and Reuss lower bound can be compared to values measured in literature and to numerical upper bounds.

Ehrhart et al. (2015) studied variations of equivalent cross-layer shear stiffness  $G_{CZ}$  of boards with three different aspect ratios and three relative distances to the pith. In this study, boards were tested individually and narrow edges are free. Then, closed-form bounds and numerical bounds are calculated for sawing patterns corresponding to this study. In Figure 1.14,  $G_{CZ}^R$  and  $G_{CZ}^V$  are plotted according to the angle  $\alpha$  and with a relative distance to the pith  $\frac{z_1}{t} = 1.5$ . In Figure 1.15,  $G_{CZ}^R$  and  $G_{CZ}^V$  are plotted according to the relative distance to the pith  $\frac{z_1}{t}$  and with an angle  $\alpha = 26.6^\circ$ .

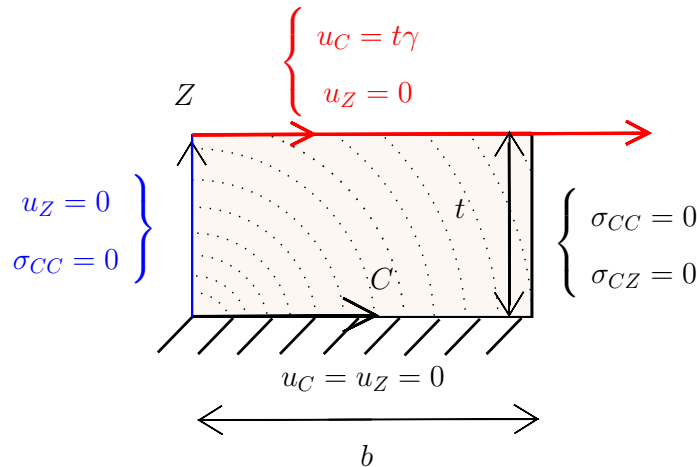


Figure 1.13 – 2D numerical simulation for calculation of the equivalent cross-layer shear stiffness of CLT and with free edges

First, it is observed that numerical upper bound for glued narrow edges is slightly lower than the Voigt upper bound for a large range of sawing patterns. This difference is greater for board close to the pith (Figure 1.15). As expected, the numerical upper bound for free narrow edges is lower than the numerical upper bound for glued narrow edges. For small angle  $\alpha$ , numerical upper bounds for glued and unglued narrow edges are similar since free edges effect are negligible and Saint-Venant principle is valid here. Nevertheless, when increasing  $\alpha$ , i.e. when decreasing the board aspect ratio, free edges effects become significant. Indeed, for  $\alpha > 20^\circ$  (Figure 1.14) and for  $\frac{z_1}{t} > 0.5$  (Figure 1.15), the numerical upper bound with free narrow edges is more than 10% lower than numerical upper bound with glued narrow edges. For  $\alpha > 45^\circ$ , which is not usual, this relative difference is higher than 21% and the upper bound for free narrow edges is lower than the lower bound of board with glued edges. Thus, the lower bound for glued narrow edges  $G_{CZ}$  must be used with caution for application to CLT with free narrow edges particularly for large  $\alpha$  since free edges effects are significant.

Second, except for large distance to the pith, measurements from Ehrhart et al. (2015) lie between Reuss and Voigt bounds. From their results, Ehrhart et al. (2015) then Schickhofer et al. (2016) suggested recommendations for the design value of  $G_{CZ}$  which are also plotted in Figures 1.14 and 1.15. Their recommendations are in agreement with the numerical upper bound for free narrow edges for usual aspect ratios when  $\alpha < 45^\circ$ . Nevertheless, it is observed that  $G_{CZ}$  can be overestimated by considering only the board aspect ratio without considering the relative distance to the pith. Particularly, for  $\frac{z_1}{t} > 2$ , the numerical upper bound is lower than 100 MPa recommended in (Ehrhart et al., 2015; Schickhofer et al., 2016).

Finally in Figure 1.16, the equivalent cross-layer shear stiffness  $G_{CZ}$  is calcu-

1.4. INFLUENCE OF THE FREE NARROW EDGES ON CROSS-LAYER SHEAR STIFFNESS  $G_{CZ}$

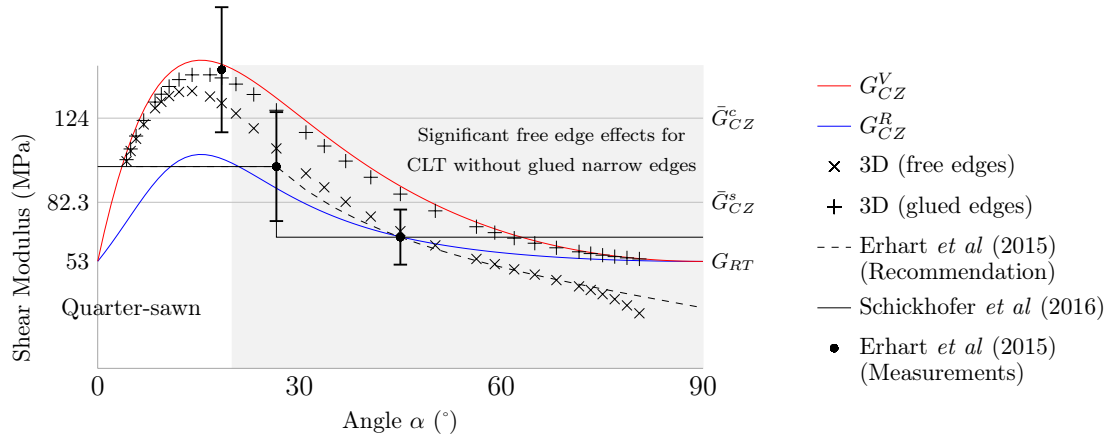


Figure 1.14 – Equivalent cross-layer shear moduli of Voigt and Reuss bounds for  $z_1 = 1.5t$

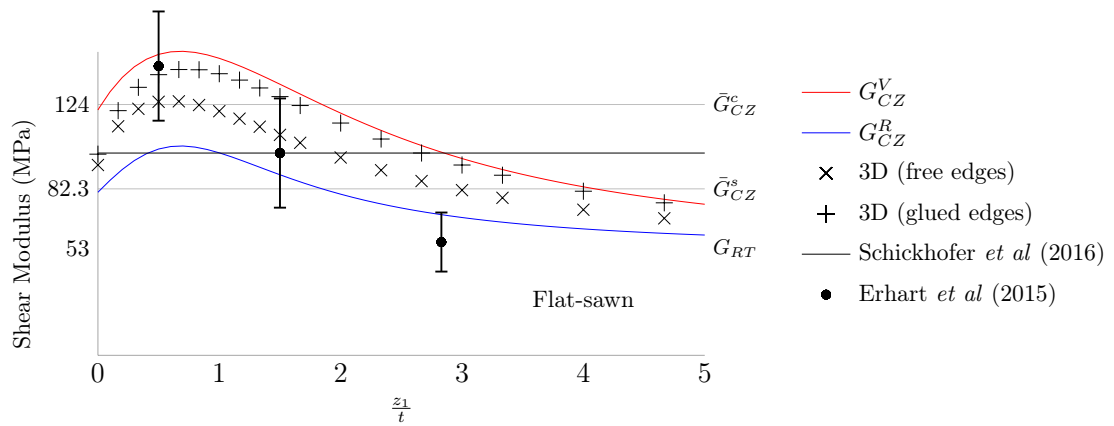


Figure 1.15 – Equivalent cross-layer shear moduli of Voigt and Reuss bounds for  $\alpha = 26.6^\circ$

lated from the Reuss lower bound  $S^R(\alpha, 0)$  and the Voigt upper bound  $C^V(\alpha, 0)$  for  $\alpha \in [0^\circ; 90^\circ]$  and  $z_1 = 0.1t$  which corresponds to samples used in (Franzoni et al., 2016a) and in Chapter 2.  $G_{CZ}$  increases up to 2.5 times the local rolling shear modulus  $G_{RT}$ . Particularly, for  $30^\circ > \alpha > 60^\circ$ , the  $G_{CZ}^R$  and  $G_{CZ}^V$  can be well approximated by  $G_{NN}^S$  and  $G_{NN}^C$ . Second, it is observed that the experimental results from Franzoni et al. (2016a) and in Chapter 2 lie between Reuss and Voigt bound. Nevertheless, numerical upper bounds are violated in both cases which could be due to a difference of the batch of wood between (Kreuzinger, 1999) used to calculate bounds and (Franzoni et al., 2016a). It is also observed that  $G_{CZ}$  measured on cross-layer with glued edges (Chapter 2) is larger than measured on boards with free edges (Franzoni et al., 2016a) on the same batch of wood as predicted numerically. Third, it is observed that the relative difference between upper bounds of boards with glued and free edges is slightly lower for boards close to the pith (Figure 1.16) than for boards more distant to the pith 1.14).

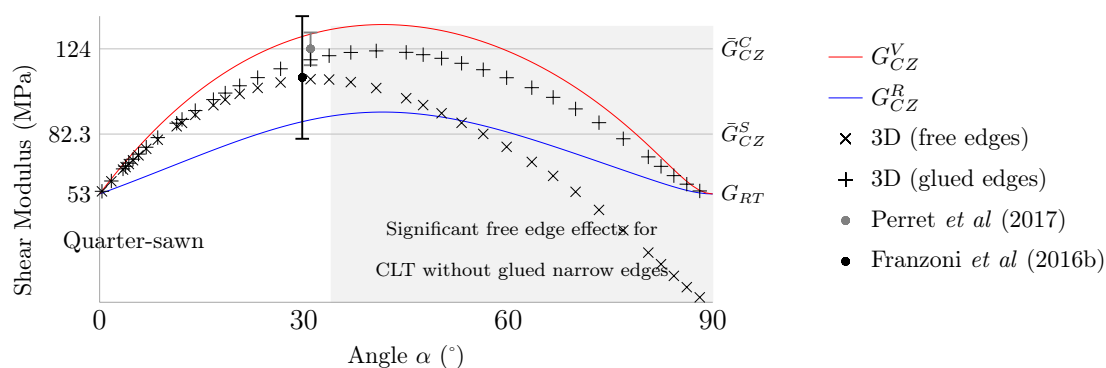


Figure 1.16 – Equivalent cross-layer shear moduli of Voigt and Reuss bounds for  $z_1 = 0.1t$

To conclude on this study, the equivalent cross layer shear stiffness  $G_{CZ}$  can be well estimated with Reuss and Voigt bounds (except for boards with free narrow edges and with small board aspect ratio which are seldom used in practice).  $G_{CZ}$  can be twice to three times the value of the local rolling shear stiffness with a careful selection of boards sawing pattern.

## 1.5 Conclusion

As a conclusion, closed-form upper and lower bounds have been suggested to estimate the equivalent layer stiffness of CLT with glued narrow edges from averages over the board section for varying sawing pattern. From these results, it was observed that the Young longitudinal modulus  $E_L$  is almost constant for varying sawing patterns and can be estimated from usual local tests. Furthermore, it was observed that cross and

## 1.5. CONCLUSION

---

normal Young moduli  $E_C$  and  $E_Z$  could decrease strongly compared to local characteristics and could take a lower value than what suggested in the revised version of the Eurocode 5.1.1 (European Committee for Standardisation, 24-02-2016).

It is also observed that for varying sawing patterns, in-plane shear modulus  $G_{LC}$  and longitudinal-layer shear modulus  $G_{LZ}$  are equivalent for glued narrow edges. Nevertheless, they are involved in very different mechanism regarding CLT. Particularly,  $G_{LZ}$  is a priori not influenced by free narrow edges conditions whereas a significant reduction of  $G_{LC}$  is observed between boards with glued and free narrow edges. This observation is in contradiction with what recommended in the revised version of the Eurocode 5.1.1 (European Committee for Standardisation, 24-02-2016) where no distinction is made between these two parameters.

Finally, it is observed that the equivalent cross-layer shear stiffness  $G_{CZ}$  varies strongly with the sawing pattern and that, with a careful selection of the sawing pattern of boards, it can be equal to 100 to 150 MPa. Then, a significant impact of free narrow edges was observed from numerical simulation:  $G_{CZ}$  is reduced compared to layers with glued narrow edges which is in agreement with experimental results from literature. Moreover, it was observed that free edges effects are more significant for increasing relative distance to the pith and decreasing the board aspect ratio.

---

# Experimental determination of the equivalent-layer shear stiffness of CLT through four point bending of sandwich beams

*The equivalent-layer stiffness can be derived from local properties of wood. Most of experimental studies on the behavior of wood have been made on the longitudinal properties. Because of the crossing layers, few studies have been performed on the local rolling shear stiffness. Here we suggest a new experimental protocol to measure directly the equivalent cross-layer shear stiffness for boards with glued narrow edges. This work was recently submitted (Perret et al., 2017b).*

## 2.1 Introduction

Cross-Laminated-Timber (CLT) is a wooden product made of several lumber layers stacked crosswise and glued on their wide faces. CLT panels are classically used in walls, floors and roofs as load carrying plate elements. Because of their low self-weight, their quick and easy assembly, and their low environmental impact, CLT panels have gained in popularity during the last few years in Northern America and in Western Europe. Several timber buildings made partly or entirely of CLT were built such as the Stadthaus building at Murray Grove in London (Lomholt, 2015), the Treet in central Bergen (Mairs, 2016) and many other projects are in progress such as the Ho-Ho building in Vienna (French, 2015) and the student residence Brock Commons in Vancouver at the University of British Columbia (Medlock, 2016).

Nevertheless, timber is a highly anisotropic material. The shear stiffness between radial and tangential directions of softwood species, also called rolling shear, is two hundred times smaller than the stiffness in the fibers' direction. Because of the crossing layers in CLT, the rolling shear significantly contributes to the global behavior of the CLT panel. Several recommendations are currently being developed to include these effects. The  $\gamma$ -method recalled in Eurocode 5 (European Committee for Standardisation, 1993) was adapted to CLT (Stora Enso, 2014) considering cross layers as mechanical joints between longitudinal layers having a stiffness related to the rolling shear stiff-

## 2.1. INTRODUCTION

---

ness. The shear analogy method (Kreuzinger, 1999) models the CLT as two virtual beams: an Euler beam without shear deformations, and a Timoshenko beam including shear stiffness of each layer. These simplified approaches may not always be sufficient for predicting the mechanical behavior of CLT and some advanced modelling are often required (Sab and Lebé, 2015; Franzoni et al., 2016b, 2017a) as noted in Chapter 3. Finally, in the CLT-designer software<sup>®</sup>, Thiel and Schickhofer (2010) suggest to use Timoshenko beam theory and derived the shear stiffness of the CLT beam from the Jourawski method. In all these approaches a reasonable estimate of the equivalent layer shear stiffness  $G_{CZ}$  is of importance. Numerous approaches have been suggested to measure this stiffness but they are not always reliable because of stress concentrations or because of indirect measurement of the shear stiffness. Moreover, a difference was observed in Chapter 1 between the local rolling shear modulus at ring scale, measured at 50 MPa approximately for softwood species, and the equivalent shear stiffness at board scale which is significantly larger (Aicher and Dill-Langer, 2000). In this chapter, we suggest a new experimental approach using the four point bending test on sandwich beam made of a wooden core between two Carbon Fiber Reinforced Polymers (CFRP) skins. In this setup, the cross-layer of a CLT is isolated from other layers and mostly contributes to the global shear behavior of the beam. It ensures a stress state close to the actual one in CLT and a proper and relevant measurement of the equivalent layer shear stiffness.

In Sections 2.1.1 to 2.1.3 several experimental studies on the shear behavior of timber are reported and classified according to the specimen scale: from the ring scale to the beam scale. After that in Section 2.1.4, the suggested methodology is briefly introduced. In Section 2.2, the validity of the sandwich beam model under four point bending is verified for specimen with a wooden core and CFRP skins. A measurement of the apparent bending stiffness by the rotation at beam ends is suggested and compared to already existing methods. Then, the feasibility and the relevance of the methodology is validated experimentally: the protocol is shown in Section 2.3 and main results on Norway Spruce specimen are presented in Section 2.4.

### 2.1.1 Tests at the ring scale

Numerous studies have been published on the rolling shear modulus and strength of timber using many different tests which are extensively reviewed and analysed by Dahl and Malo (2009a). Most of shear tests listed in (Dahl and Malo, 2009a) are adapted to measure the local shear properties of timber. In these tests, a particular attention is always paid to the relative size of specimens compared to the radius of curvature of annual rings in order to preserve a uniform orientation.

The first methodology consists on compression tests on small timber blocks with geometries and loading configurations leading to a local shear state in timber. Several of them are listed by Kollman and Côté (1968). The notched shear block test sug-

**CHAPTER 2. EXPERIMENTAL DETERMINATION OF THE EQUIVALENT-LAYER SHEAR STIFFNESS OF CLT THROUGH FOUR POINT BENDING OF SANDWICH BEAMS**

gested by the American Society for Testing and Materials (ASTM, 1981) consists in the compression of a small cubic block with notches (Figure 2.1). This test has been extensively used to measure shear strength of timber, some of which are reported by Kollman and Côté (1968). Nevertheless it has been criticized by many authors (Dahl and Malo, 2009a; Youngs, 1957; Liu et al., 1998) because of three main drawbacks: it introduces high stress concentration caused by the notch, an additional bending moment is caused by the load eccentricity and the non-uniform stress distribution over the failure plane yields inaccurate strength results. Moses and Prion (2002) captured these effects by a finite elements model and observed that they lead to an underestimation of the shear strength by a ratio of 1.7 approximately. A comparable test method called short beam tests consists in a beam with a very small span to depth ratio uniformly loaded. Dahl and Malo (2009a) observed improper failure due to additional bending moment and to impure stress state.

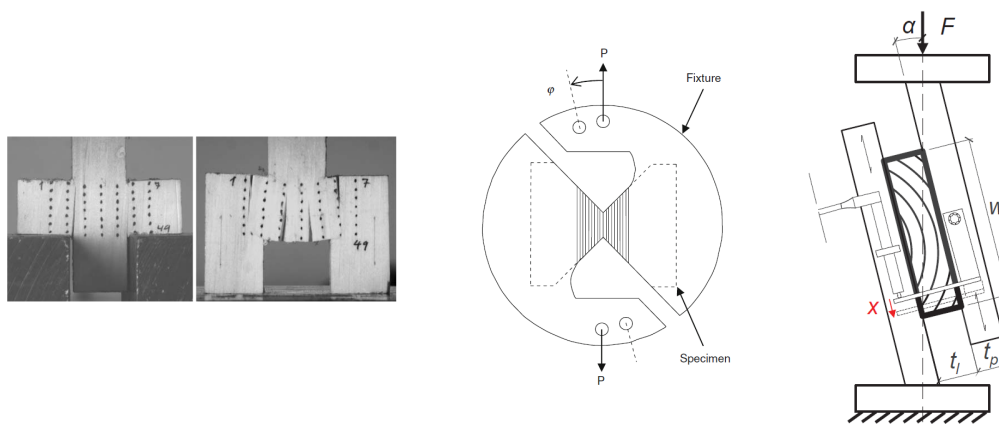


Figure 2.1 – Notched shear block test (Dahl and Malo, 2009a) (left), Arcan shear test (Dahl and Malo, 2009a) (center) and Single-lap shear test (right) (Ehrhart et al., 2015)

Another configuration is called the Iosipescu shear test (Iosipescu, 1967). A beam with  $90^\circ$  notches at top and bottom of the central section is loaded such that the central section is under pure shear stress. Using this method, Dumail et al. (2000) measured an average rolling shear stiffness of 57.7 MPa on specimen made of *Norway Spruce* where the variations of ring orientation were negligible. Nevertheless, because of the bending moment close to the central section, the shear failure can be affected by improper failure particularly in the radial-tangential plane. Using a comparable mechanical principle, the Arcan shear test (Arcan et al., 1978) consists of specimens with a butterfly shape, which leads to pure shear failure at the center section (Figure 2.1). Dahl and Malo (2009a) used this test in six different configurations to measure the shear modulus in the three orthotropic directions and evaluated an averaged rolling shear stiffness of *Norway Spruce* equal to 30 MPa approximately using video extensometry. In a following study,

## 2.1. INTRODUCTION

---

Dahl and Malo (2009b) measured an average rolling shear strength of 1.6 MPa. From these results, Dahl and Malo (2009a) observed that the Arcan shear test seems one of the most reliable test to estimate local shear strength and stiffness of wood.

Lastly, an alternative test to measure the local shear stiffness of Norway Spruce has been used by Keunecke et al. (2007). The Young and shear moduli are derived from the measure of sound velocity of longitudinal waves and transverse waves respectively in a small cubic specimen (10 mm in each material direction). In particular, they measured a local rolling shear stiffness of 53 MPa.

Several studies have been conducted with scattered results from which it is difficult to conclude on the rolling shear behavior of timber.

### 2.1.2 Tests at the individual board scale

All previously mentioned studies were about local properties of timber: particular attention was paid to rings orientation to the specimen in order to neglect their variations. Aicher and Dill-Langer (2000) then Jakobs et al. (2005) studied numerically the effect of the sawing pattern, defined as the distribution of ring orientation in the section, on the equivalent layer shear stiffness in the radial-tangential plane. They simulated numerically the single lap shear test of softwood specimen: the board size specimen is glued between two plates moving laterally respectively to each other in order to shear the specimen (Figure 2.1) (D2718, 2003). The shear modulus is estimated from the relative displacement between the two plates. They estimated an equivalent cross-layer shear stiffness between 45 MPa and 350 MPa whereas the input local rolling shear modulus was set at 50 MPa. They observed maximum values for sawing patterns with annual ring orientations at 45°. These observations were confirmed by the experimental work of Ehrhart et al. (2015) on single lap shear tests and of Franzoni et al. (2017b) on double lap shear test and the experimental and numerical work of Görlacher (2002) by means of eigenfrequency. Jakobs et al. (2005) then Ehrhart et al. (2015) observed that the increase of the board aspect ratio, defined as the ratio between width and thickness, as well as the decrease of the radial distance to the pith lead to an increase of the effective shear stiffness. Moreover, an increase of the shear strength is also observed when increasing board aspect ratio. From these observations, Ehrhart *et al* recommend to set the effective shear stiffness and strength according to linear functions of the board aspect ratio revised later by Schickhofer et al. (2016). In Chapter 1, we suggested closed-form bounds of the equivalent cross-layer shear stiffness of timber depending on the sawing pattern and on local mechanical characteristics at ring scale. It was observed particularly that, if the board is cut relatively close to the pith, the equivalent cross-layer shear stiffness lies between 100 and 150 MPa. Therefore, single or double lap shear tests are reliable to measure the effective transverse shear stiffness and strength of boards which depend on the width to depth ratio and on the radial distance to the pith. In these studies, properties of boards are measured individually leading to a high coefficient of

variation (between 20 and 30% (Ehrhart et al., 2015; Franzoni et al., 2017b)) whereas they are numerous in CLT layers which should have an averaging effect. Zhou et al. (2014) observed a smaller coefficient of variation of 16.5% from single-lap shear test on wooden cross layer made of several boards with glued narrow edges. Nevertheless, these approaches are very sensitive to geometric imperfections and wood variability. Indeed, parasitic bending moments may occur and introduce non-linear response. Mestek (2011) suggested modifications, followed by Ehrhart et al. (2015), such as the angle between the applied force and the plate orientation and also the plate's geometry to reduce these effects.

### **2.1.3 Tests at the beam scale**

Thus, tests on full-size specimen seem more relevant to measure the actual shear behavior of CLT panel. According to (408, 2012), the longitudinal shear moduli of a solid wood or glue-laminated timber beam can be calculated from two bending tests: a four point bending test with a slenderness, defined as the ratio between the span and the thickness, larger than 18 where the pure bending modulus is calculated from relative deflection in the pure bending area between loads and a three-point bending test with a slenderness of 5 where the apparent bending modulus, including the pure bending modulus and the longitudinal shear modulus, is calculated from the mid-span deflection. Another methodology is suggested by Yoshihara et al. (1998); Yoshihara and Kubojima (2002) where beams are tested under three-point bending, asymmetric four point bending or five-point bending tests (Yoshihara and Furushima, 2003) with varying span to depth ratio. These tests provide higher ratio of shear stress to bending stress and then a higher relative shear deflection. Nevertheless, the Saint Venant's principle can be violated during these tests because of small slenderness leading to a non reliable shear correction factor in the Timoshenko beam theory as observed by Yoshihara et al. (1998).

Zhou et al. (2014) studied the shear behavior of 3-ply CLT beams under three-point bending with varying span to depth ratio. They compared the measured deflection to the theoretical deflection from shear analogy method. They used equivalent cross-layer shear stiffness measured previously from single-lap shear test and longitudinal layer stiffness measured by means of vibration test. Nevertheless, they observed that the deflection is overestimated by the shear analogy method: the estimated deflection is 64% to 11% higher than the measured deflection for span to depth ratio from 6 to 14.

As a conclusion, tests on CLT beams can be used to verify assumptions on the global shear behavior of the CLT but it is not relevant to measure individually the shear behavior of each layer.

### 2.1.4 Tests at a single layer scale

Considering the advantages and inconvenient of each identification methods recalled in the preceding section, we present here a new methodology to estimate the equivalent cross-layer shear stiffness of timber: a bending test on a sandwich beam composed of a thick wooden cross-layer core glued between two thin CFRP skins (Figure 2.2). The aim of this methodology is to isolate the cross-layer in order to characterize exclusively its shear behavior. Indeed, it is commonly accepted that, when the contrast is sufficient, the skins contribute mainly to the bending stiffness and that the core mostly affects the transverse shear stiffness of the sandwich beam. Thus the shear deflection is only due to the inner cross-layer, contrary to CLT beams where it is mixed between shear effects in longitudinal layers and in cross layers. As a consequence, the equivalent cross-layer shear stiffness of the wooden core as well as the composite skins stiffness can be directly estimated from a four point bending test of the sandwich beam. Moreover, the bending stiffness is well controlled by the CFRP skins. Indeed CFRP present low material variability and creep is mitigated in the longitudinal direction in contrast to longitudinal layers in CLT beams. Besides, the variability of the wooden core is closest to the actual behavior of cross-layers of CLT than that of single lap shear tests because it is made of numerous boards. We will see that this also reduce the standard deviation of results. Finally, we investigate a new measurement of the bending stiffness from the rotation at beam ends which will prove more reliable than the measurement from the relative deflection between loads since it averages the bending behavior on the whole span of the beam. In this chapter, only the short term elastic behavior is presented but the methodology is already under application for creep tests.

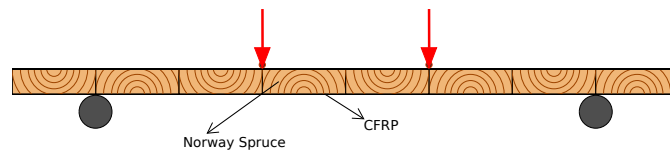


Figure 2.2 – Four point bending of a CFRP sandwich beam with wooden core

## 2.2 Identification by four point bending of homogeneous sandwich beam

Here, we consider that characteristics at board scale are homogeneous to analyze the behavior of a sandwich beam under four point bending. Therefore we use the notation  $G_{CZ}$  instead of  $G_{RT}$  and  $E_C$  instead of  $E_T$ .  $G_{CZ}$  and  $E_C$  are a mean of local properties  $G_{RT}$ ,  $E_R$  and  $E_T$  averaged at board scale (Chapter 1). Basic features of sandwich theory are first recalled and their hypothesis are validated by a reference 3D finite

element model. The numerical model is also used to investigate the sensitivity of the identification procedure to input characteristics and local effects.

## 2.2.1 The sandwich beam model

Main features of the sandwich beam model are recalled here, more details can be found in (Lebéé and Sab, 2012). The studied sandwich beam is composed of a thick homogeneous wooden core of thickness  $t_c$  between two thin CFRP skins of thickness  $t_s$ . The total thickness is noted  $h = t_c + 2t_s$  and the width is noted  $b$ . Cartesian coordinates  $x, y, z$  are used in the reference frame  $(\underline{e}_x, \underline{e}_y, \underline{e}_z)$  (Figure 2.4) where  $x$  is the abscissa in the longitudinal direction of the beam and  $y$  and  $z$  are the coordinates in the section of the beam. Among the nine mechanical characteristics of the wooden core and the five mechanical characteristics of CFRP, which is modeled as transversely isotropic, only the Young moduli in the beam longitudinal direction and the transverse shear moduli are necessary in the beam model. They are noted  $(E_s, G_s)$  for the skins and  $(E_C, G_{CZ})$  for the core. In the sandwich beam model (Allen, 2013), a stiffness and a thickness contrasts are assumed between the core and the skins such that:

$$E_s \gg E_C, \quad E_s t_s \gg E_C t_c, \quad t_c \gg t_s. \quad (2.1)$$

Considering here  $E_s = 110$  GPa,  $E_C = 0.43$  GPa,  $t_c = 30$  mm and  $t_s = 1.2$  mm, we easily check that these conditions are satisfied. Hence, because of these contrasts, the skins contribute mainly to the bending stiffness  $D$  whereas the core mostly affects the shear force stiffness  $F$  as recalled from Allen (2013):

$$\left\{ \begin{array}{l} D \approx \frac{b(h^3 - t_c^3)}{12} E_s, \\ F \approx \frac{b(t_c + t_s)^2}{t_c} G_{CZ}. \end{array} \right. \quad (2.2a)$$

$$(2.2b)$$

The bending moment  $M$  and the shear force  $Q$  are classically defined by:

$$\left\{ \begin{array}{l} M(x) = - \int_{-\frac{h}{2}}^{\frac{h}{2}} b z \sigma_{xx}(x, z) dz, \\ Q(x) = \int_{-\frac{h}{2}}^{\frac{h}{2}} b \sigma_{xz}(x, z) dz. \end{array} \right. \quad (2.3a)$$

$$(2.3b)$$

## 2.2. IDENTIFICATION BY FOUR POINT BENDING OF HOMOGENEOUS SANDWICH BEAM

Approximations of the bending stress  $\sigma_{xx}$  and the shear stress  $\sigma_{xz}$  are derived according to Jourawski (1856):

$$\begin{cases} \sigma_{xx}(z) = -\frac{ME(z)}{D}z, & (2.4a) \\ \sigma_{xz}(z) = -\frac{Q}{D} \int_{-\frac{h}{2}}^z \zeta E(\zeta) d\zeta. & (2.4b) \end{cases}$$

Furthermore, considering the stiffness contrast (2.1), the shear stress  $\sigma_{xz}$  (2.4b) can be approximated as uniform in the wooden core by:

$$\sigma_{xz}^c \approx \frac{Q}{b(t_c + t_s)}. \quad (2.5)$$

In Figure 2.3, this approximated shear stress  $\sigma_{xz}^c$  is compared to the shear stress distribution calculated from Jourawski method (2.4b). For the studied specimen (Section 2.3), the difference is lower than 1% in the core.

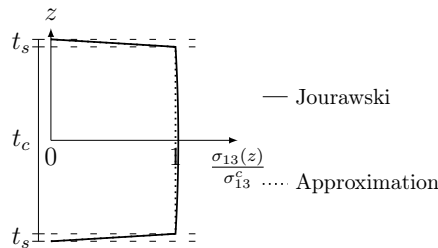


Figure 2.3 – Distribution of shear stress  $\sigma_{xz}$  in the wooden core relatively to the estimation of the stress  $\sigma_{xz}^c$  in the core

### 2.2.2 The four point bending test

Different measures allowing the identification of the bending and shear force stiffnesses from the four point bending are now presented. The beams of length  $L$  are simply supported on a span  $l < L$  and submitted to two loads  $\frac{P}{2}$  placed symmetrically at a distance  $\frac{l_0}{2}$  from the mid-span (Figure 2.4). The beam is under pure bending state between the two loads leading to a constant curvature. The bending stiffness  $D$  is then directly related to the relative deflection  $\Delta f = f_A - \frac{f_B + f_{B'}}{2}$ , between the mid-span (point A in Figure 2.4) and a point distant to the mid-span of a length  $a < \frac{l_0}{2}$  (points B and B' in Figure 2.4):

$$D = \frac{P(l - l_0)}{8\Delta f} a^2, \quad (2.6)$$

**CHAPTER 2. EXPERIMENTAL DETERMINATION OF THE EQUIVALENT-LAYER SHEAR STIFFNESS OF CLT THROUGH FOUR POINT BENDING OF SANDWICH BEAMS**

where  $f_A$ ,  $f_B$  and  $f'_B$  are absolute deflections at points  $A$ ,  $B$ , and  $B'$ . In the pure bending area, the bending stiffness  $D$  is also directly related to the relative bending strain  $\Delta\varepsilon = \varepsilon_{xx}(-\frac{h}{2}) - \varepsilon_{xx}(\frac{h}{2})$  between lower face in tension and the upper face in compression of CFRP skins:

$$D = \frac{P(l-l_0)h}{4\Delta\varepsilon}. \quad (2.7)$$

Moreover, at beam ends ( $C$  and  $C'$  in Figure 2.4), the bending moment  $M$  and the shear force  $Q$  vanish and effective rotations  $\varphi_C$  and  $\varphi_{C'}$  at ends  $C$  and  $C'$  may be directly identified to the beam inclination. The relative rotation of the section at beam ends  $\varphi_0 = \varphi_C - \varphi_{C'}$  is related to the bending stiffness  $D$  by:

$$D = \frac{P(l^2 - l_0^2)}{8\varphi_0}. \quad (2.8)$$

The relative accuracy of these different measurements will be discussed in Sections 2.2.3.3 and 2.4.

Since the global deflection includes bending and shear deflections, the shear stiffness  $F$  of the beam can be expressed as a function of the mid-span deflection  $f_A$  and the bending stiffness  $D$ :

$$\frac{1}{F} = \frac{4f_A}{P(l-l_0)} - \frac{1}{8D} \left( l^2 - \frac{1}{3}(l-l_0)^2 \right), \quad (2.9)$$

where  $D$  is derived either from  $\Delta f$ ,  $\Delta\varepsilon$  or  $\varphi_0$  according to (2.6,2.7,2.8).

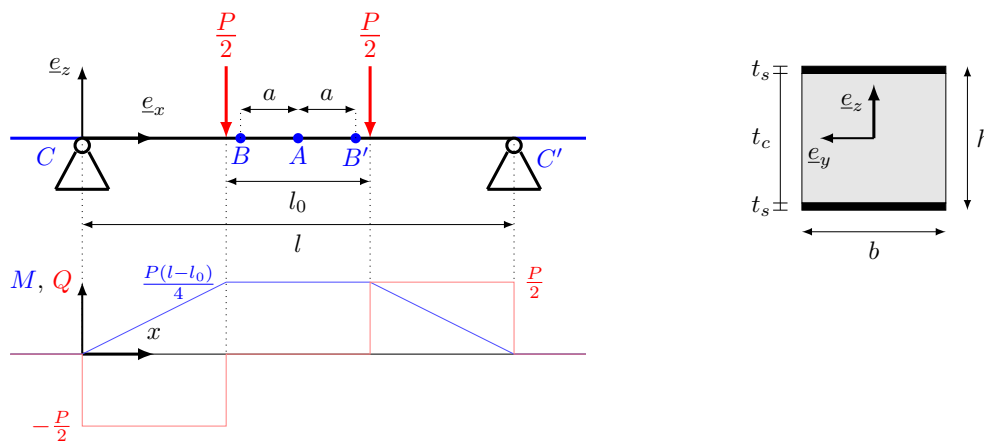


Figure 2.4 – Four point Bending test

The bending stiffness  $D$  is inversely proportional to  $\Delta f$ ,  $\Delta\varepsilon$  and  $\varphi_0$  according to (2.6, 2.7,2.8). Thus small relative variations of  $\Delta f$ ,  $\Delta\varepsilon$  or  $\varphi_0$  will lead to relative varia-

tions of the estimated bending stiffness  $D$  of the same order of magnitude. In contrast, according to (2.9), the shear stiffness  $F$  is calculated from the difference between the deflection  $f_A$  and the estimated bending deflection at mid-span. For the studied specimen, the shear deflection is approximately one third of the total deflection  $f_A$ . Thus, considering that the total deflection  $f_A$  do not vary, small relative variations of  $\Delta f$ ,  $\Delta \varepsilon$  or  $\varphi_0$  will lead to relative variations of the estimated shear stiffness  $F$  twice larger. Conversely, considering that  $\Delta f$ ,  $\Delta \varepsilon$  or  $\varphi_0$  do not vary, small relative variations of  $f_A$  will lead to relative variations of the estimated shear stiffness  $F$  three times larger. Thus it is observed that the predicted shear stiffness  $F$  is very sensitive, much more than  $D$ , to variations of  $\Delta f$ ,  $\Delta \varepsilon$ ,  $\varphi_0$  and  $f_A$ . This is why a fine estimation of the bending stiffness  $D$  and of the mid-span deflection  $f_A$  is necessary to predict properly the shear stiffness  $F$ .

### 2.2.3 Validation of the sandwich beam model with a 3D finite element model

In this section, the validity of the sandwich beam model is investigated by means of a 3D model complying with the geometry of samples used in the experimental study (Section 2.3.1).

#### 2.2.3.1 The 3D model

The beam is modeled by a core perfectly bounded with two skins with the finite elements software ABAQUS. Cylinders corresponding to supports and loads are modeled as rigid cylindrical shells. Supports are fixed while intermediate cylinders moving vertically are loaded with  $P/2$ . A frictionless tangent contact is set between the beam and the cylinders.

An incremental static analysis is performed with a starting increment of 1% of the total load  $P = 1\text{kN}$ . Non-linear geometric effects are taken into account in the calculation of the deformed state in order to handle contact interactions.

The beam is meshed with 3D cubic elements C3D20R (Hibbett et al., 1998) with twenty nodes and reduced integration on 8 points. Figure 2.5 shows that the size of the mesh decreases close to contact areas to better capture local stresses and strains in these boundary layers.

Both materials are modeled as transversely isotropic (Table 2.1): the skins are isotropic in the plane  $(O, \underline{e}_y, \underline{e}_z)$  and the core is isotropic in the plane  $(O, \underline{e}_x, \underline{e}_z)$ . The mechanical characteristics of the wooden core are in agreement with the experimental study of Franzoni et al. (2017b) and with Reuss and Voigt bounds calculated in Chapter 1.

Only one fourth of the beam is tested because of planes of symmetry normal to  $\underline{e}_x$  and to  $\underline{e}_y$ .

CHAPTER 2. EXPERIMENTAL DETERMINATION OF THE EQUIVALENT-LAYER SHEAR STIFFNESS OF CLT THROUGH FOUR POINT BENDING OF SANDWICH BEAMS

Elastic Moduli (MPa)	$E_L$	$E_C$	$G_{LC}$	$G_{CZ}$	$\nu_{LN}$
CFRP	115,000	7,000	4,000	2,700	0.3
Wood	12,700	430	600	110	0.43

Table 2.1 – Mechanical characteristics of wood and carbon fiber reinforced polymer

2.2.3.2 Accuracy of the stress estimation in the core

In this paragraph, the stress distribution in the wooden core of the beam is studied in order to check if the shear stress is almost uniform in the core between supports and loads and if the bending stress in the core is negligible in agreement with the main hypotheses of the sandwich beam theory.

In Figure 2.5, the relative error of the transverse shear stress  $\sigma_{xz}$  in one half of the beam is plotted with respect to the sandwich beam estimation  $\sigma_s = \frac{P}{2b(t_s+t_c)}$  (2.5). It is observed that, in approximately 90% of the area between support and load, the relative difference between the predicted shear stress  $\sigma_s$  and the 3D reference shear stress is within 10%. As expected, fast variations are observed close to contacts with cylinders.

In Figure 2.6, distributions of the transverse shear stress are plotted along the  $x$  axis at three locations: at neutral fibre level in the wooden core and at fibers close to the interface between wood and composites at  $z = \pm \frac{7t_c}{16}$  (yellow lines in Figure 2.5). The origin of the abscissa is located at the support, the load is applied at 200 mm from the support, -100 mm is the free end of the beam. Boundary layers are observed close to supports and loads, they are getting smaller close to the neutral axis. From these figures, the sandwich beam hypothesis of a constant shear stress distribution in the wooden core is globally satisfied.

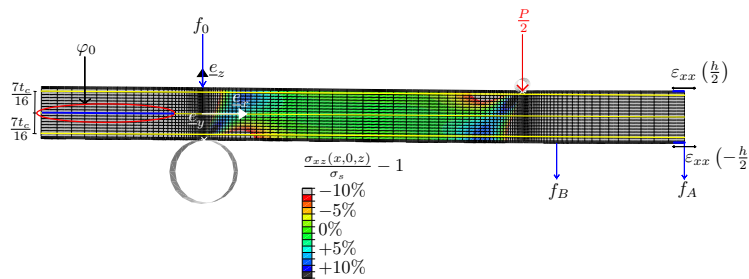


Figure 2.5 – 3D shear stress distribution  $\sigma_{xz}(x, 0, z)$  compared to sandwich beam estimation  $\sigma_s$

In Figures 2.7 and 2.8, the bending stress  $\sigma_{xx}$ , the transverse stress  $\sigma_{zz}$  and the shear stress  $\sigma_{xz}$  are plotted in the wooden core at neutral axis and on fibers close to the interface between wood and composites at  $z = \pm \frac{7t_c}{16}$ , and in the CFRP skins on top and

## 2.2. IDENTIFICATION BY FOUR POINT BENDING OF HOMOGENEOUS SANDWICH BEAM

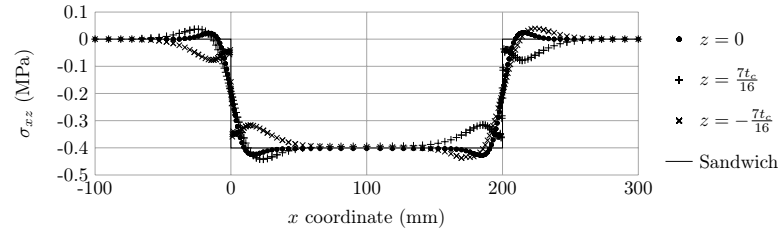


Figure 2.6 – Shear stress  $\sigma_{xz}$  along the beam for upper, lower and neutral fiber in the core from 3D and sandwich beam models

bottom fibers  $z = \pm \frac{h}{2}$ . Stresses are normalized with the corresponding strength: the transverse tensile, compressive and rolling shear strength of wood are set to  $\sigma_{cr,90,t} = 1.8$  MPa, to  $\sigma_{cr,90,c} = 3.0$  MPa and to  $\sigma_{cr,RT} = 1.7$  MPa respectively according to Franzoni et al. (2017b); the transverse compressive and tensile strength of CFRP skins are set to 50 MPa.

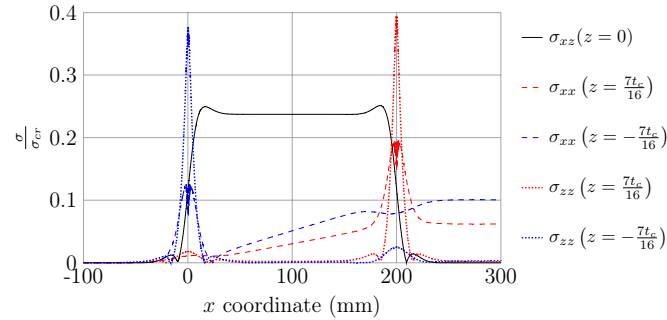


Figure 2.7 – Distribution of stresses  $\sigma_{xx}$ ,  $\sigma_{zz}$  and  $\sigma_{xz}$  in timber normalized with the corresponding strength

High stress concentrations are observed at contact areas on top fiber under the load and on bottom fiber on support. Particularly, a maximum compressive transverse stress  $\sigma_{zz}$  of 60% of the compressive strength is observed in CFRP skins due to the small contact area with cylinders. This high stress could lead to local punching of CFRP skins. In the experimental setup (Section 2.3.3) metal plates are therefore set between cylinders and specimen during tests reducing up to six times this local transverse stress in skins and to twice the local stress in the wooden core according to a complementary 3D finite element study (not shown here for consistency). The global deflection measured with this metal plates differs less than 2% from the deflection without metal plates.

Nevertheless, in the area between supports and loads, the wooden core is mostly sheared. Neglecting local stress concentration close to contact areas and considering its linear distribution through thickness, the average bending stress  $\sigma_{xx}$  in the wooden core is approximately 1.7% of the compressive strength and 2.9% of the tensile strength

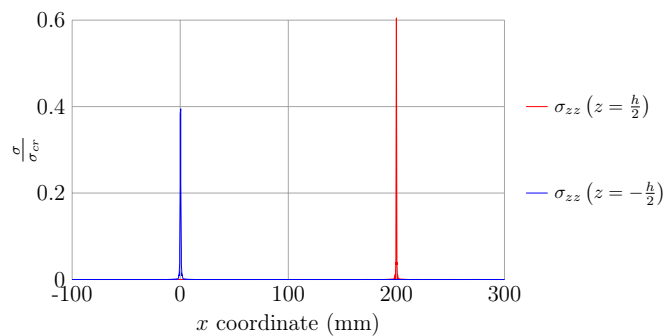


Figure 2.8 – Distribution of stresses  $\sigma_{zz}$  in CFRP normalized with the tensile and compressive strength

between support and load. The transverse stress  $\sigma_{zz}$  is very low, lower than 1% of the strength, in the major part of the section between load and supports. In contrast, the average shear stress is approximately 24% of the rolling shear strength. Thus, the assumption of a pure shear state in the core between load and support is admissible as first approximation compared to averaged bending and transverse stress.

### 2.2.3.3 Accuracy of the global deflection estimation

The deflection of the sandwich beam is observed for a total applied load  $P$  of 1 kN corresponding to 24% of the rolling shear failure measured in (Franzoni et al., 2017b) and to a maximum deflection of 2mm approximately. Kinematic variables  $\varphi_0$ ,  $\Delta f$ ,  $f_A$  and  $\Delta\varepsilon$  are evaluated by the three-dimensional result on locations pointed in Figure 2.5 and corresponding to the sensors locations during experiment (Section 2.3).

- $\Delta f$ ,  $f_A$  are given by deflections of the lower fiber at  $x = \frac{l}{2} - a$  ( $f_B$ ) and  $x = \frac{l}{2}$  ( $f_A$ );
- $\Delta\varepsilon$  is extracted from the longitudinal strains on top and bottom fibers at mid-span section;
- The rotation  $\varphi_0$  is calculated from a linear regression of the deflection at neutral axis on the domain plotted in blue (Figure 2.5)  $x \in [\frac{l-L}{2}; \frac{l-L}{10}]$  in order to avoid boundary layers close to supports.

In Figure 2.9, the difference between the reference three-dimensional deflection  $u_z(x, 0, z)$  on neutral ( $z = 0$ ), upper ( $z = \frac{h}{2}$ ) and lower ( $z = -\frac{h}{2}$ ) axis and the deflection  $f(x)$  calculated from the sandwich beam model are plotted along the beam normalized with the three-dimensional mid-span deflection  $u_z(\frac{l}{2}, 0, 0)$  at neutral axis. It is observed that the deflection approximated by the sandwich beam theory is very close to the 3D results.

Moreover, in Figure 2.9, a local deflection at supports is observed. On the upper fiber, this deflection is equal to 1.4% of the total mid-span deflection. This is due to a

## 2.2. IDENTIFICATION BY FOUR POINT BENDING OF HOMOGENEOUS SANDWICH BEAM

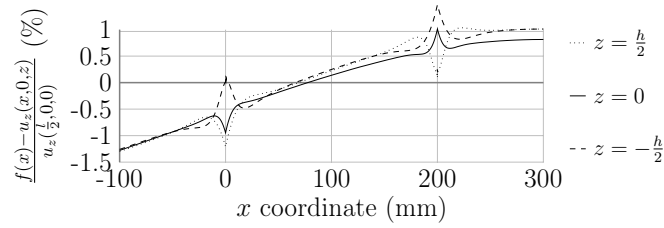


Figure 2.9 – Relative deflection between sandwich and 3D models normalized with the mid-span deflection

local punching. Compared to the variability of wood mechanical characteristics, the effect of this punching on the measured deflections is negligible. Indeed, the 3 deflections are very close at the mid-span (the relative difference is about 0.2%). Thus the impact of the local punching on the measurement of deflection is negligible.

### 2.2.3.4 Stiffness identification

A linear regression between the load  $P$  and the kinematic variables is calculated from results at each increment of the numerical calculations to the tangent stiffness at each step. The bending stiffness  $D^{\text{est}}$  is estimated from the relative deflection  $\Delta f$ , the relative bending strain  $\Delta \varepsilon$  at mid-span and the relative rotation at beam ends  $\varphi_0$  according to the sandwich beam model (Equations 2.6, 2.7 and 2.8).

In Table 2.2, skins Young modulus  $E_{L,\text{CFRP}}^{\text{est}}$  and apparent core shear stiffness  $G_{NZ}^{\text{est}}$  estimated from the deflection measurement ( $f_A, \Delta f, \varphi_0, \Delta \varepsilon$ ) are compared with the actual elastic parameters ( $E_{L,\text{CFRP}}, G_{CZ}$ ) in the 3D finite-element model. It is first observed that the skins Young modulus  $E_{L,\text{CFRP}}$  is always overpredicted which is mostly due to the sandwich beam assumptions: contribution of the wooden core in the bending stiffness is neglected. On the contrary, the core shear stiffness  $G_{CZ}$  is always underestimated which is partly due to the assumption of negligible contribution of skins to shear compliance (Allen, 2013).

Moreover, it is observed that predictions with rotation  $\varphi_0$  or strains  $\Delta \varepsilon$  have an accuracy of 2% whereas predictions with relative deflection  $\Delta f$  have an accuracy of 3.5%. From a parametric study in Table 2.2, the relative errors of predicted stiffnesses vary slightly according to input parameters ( $E_{L,\text{CFRP}}, G_{CZ}$ ). Particularly, it is observed that the prediction error of  $E_{L,\text{CFRP}}^{\text{est}}$  is subjected to larger variations when estimated from  $\Delta f$  than from  $\Delta \varepsilon$  or  $\varphi_0$ .

From these comparisons and analyses, we conclude that the sandwich beam model is accurate for the estimation of the composite modulus  $E_{L,\text{CFRP}}$  and the equivalent rolling shear modulus  $G_{CZ}$  with an error lower than 2.0% according to  $\varphi_0$  or  $\Delta \varepsilon$ , which confirms the relevance of the estimation based on  $\varphi_0$ .

CHAPTER 2. EXPERIMENTAL DETERMINATION OF THE EQUIVALENT-LAYER SHEAR STIFFNESS OF CLT THROUGH FOUR POINT BENDING OF SANDWICH BEAMS

$E_{L,CFRP}$	(GPa)	105	110	115	105	110	115	105	110	115
$G_{CZ}$	(MPa)	105	110	115	105	110	115	105	110	115
$\frac{E_{L,CFRP}^{est} - E_{L,CFRP}}{E_{L,CFRP}}$	$\Delta f$	3.26	2.93	2.66	3.24	2.90	2.63	3.22	2.88	2.58
	$\varphi_0$	2.02	2.01	1.99	1.94	1.93	1.91	1.87	1.86	1.84
(%)	$\Delta \varepsilon$	1.91	2.01	1.89	1.83	1.82	1.81	1.76	1.75	1.74
$\frac{G_{NZ}^{est} - G_{CZ}}{G_{CZ}}$	$\Delta f, f_A$	-3.53	-3.35	-3.19	-3.55	-3.36	-3.21	-3.54	-3.36	-3.20
	$\varphi_0, f_A$	-1.27	-1.56	-1.84	-1.26	-1.56	-1.83	-1.26	-1.56	-1.83
(%)	$\Delta \varepsilon, f_A$	-1.05	-1.56	-1.63	-1.05	-1.35	-1.63	-1.06	-1.36	-1.63

Table 2.2 – Relative error of the estimation of stiffnesses  $E_{L,CFRP}^{est}$  and  $G_{NZ}^{est}$  by the sandwich beam model compared to input variables  $E_{L,CFRP}$  and  $G_{CZ}$

## 2.3 Experimental campaign

### 2.3.1 Specimen fabrication

The specimen are made of a wooden core between two CFRP layers. The wood comes from samples taken from Franzoni et al. (2017b). It consists of *Norway Spruce* boards with a thickness of 30 mm and a width of 100 mm. They have been previously conditioned at 20°C and 65% relative humidity (RH) during at least one week, so that the moisture content in boards is between 10 and 13% before gluing. Ten boards are glued on their narrow faces with a two components glue including a thixotropic epoxy based impregnating resin and an adhesive (Sikadur 330). Then, 800 mm long specimens with a width  $b = 40$  mm and a thickness  $t_c = 30$  mm are cut, so that the wood fibers are oriented in the transverse direction. These specimen are conditioned again at 20°C and 65% relative humidity (RH) before gluing with CFRP skins. A total of 12 specimens are fabricated.

The CFRP skins are made of six carbon fiber epoxy prepreg sheets stacked and cured at 120°C during 90 minutes. The final skins consist thus in CFRP with a length  $L = 800$ mm, a width  $b = 40$ mm and a thickness  $t_s = 1.2$ mm  $\pm$  0.2mm. Two sets of CFRP skins with different mechanical properties are used in this study (One for specimens RS1-1 to RS1-3, the others for specimens RS2-1 to RS2-9).

Finally, for each wooden specimen, the CFRP skins are glued on the top and bottom faces of timber with the same glue as for timber's narrow edges during 24 hours. The thickness of the glue is measured between smaller than 0.2 mm. As observed in Figures 2.2 and 2.11, boards are carefully oriented, so that the pith is alternatively at the bottom and top faces of the specimen in order to mitigate their effect on the global behavior.

### 2.3.2 Identification of bending and shear stiffness with the four point bending test

Each specimen is made of several boards with different mechanical properties because of annual rings as well as natural variations of wood which for the moment were not taken into account in the model. To consider these variations, it is possible to go further than in Section 2.2 and to assume that the bending stiffness  $D(x)$  and the shear stiffness  $F(x)$  vary slowly along the beam. Thus,  $D$  and  $F$  measured from relative deflection  $\Delta f$ , rotation on beam ends  $\varphi_0$ , bending strains  $\varepsilon_{xx}$  and mid-span deflection  $f_A$  (Section 2.2.2) are averaged properties of the beam. By means of Castigliano theorem, it can be shown that the measured bending stiffness  $D_{\Delta f}$  (2.6),  $D_\varepsilon$  (2.7),  $D_\varphi$  (2.8) and  $D_f$  (2.9) and the measured shear stiffness  $F_f$  (2.9) are averages of the local bending stiffness  $D(x)$  and shear stiffness  $F(x)$ :

$$\frac{1}{D_{\Delta f}} = \frac{1}{a} \int_0^l \frac{w_{\Delta f}(x)}{D(x)} dx \quad ; \quad \frac{1}{D_\varphi} = \frac{2}{l+l_0} \int_0^l \frac{w_\varphi(x)}{D(x)} dx \quad ; \quad \frac{1}{D_\varepsilon} = \frac{1}{D\left(\frac{l}{2}\right)} \quad ;$$

$$\frac{1}{D_f} = \frac{2l}{l^2 - \frac{(l-l_0)^2}{3}} \int_0^l \frac{w_{f,D}(x)}{D(x)} dx \quad ; \quad \frac{1}{F_f} = \frac{1}{l-l_0} \int_0^l \frac{w_{f,F}(x)}{F(x)} dx,$$

where,  $w_{\Delta f}(x)$ ,  $w_\varphi(x)$ ,  $w_{f,D}$  and  $w_{f,F}$  can be considered as weight functions plotted in Figure 2.10.

From these distributions, the equivalent compliance  $\frac{1}{D_\varphi}$  is a weighted average of  $\frac{1}{D(x)}$  on the whole span  $l$  of the beam whereas  $\frac{1}{D_{\Delta f}}$  is a weighted average on a length  $2a$  only. Thus, the measurement of the bending compliance with the relative deflection  $\Delta f$  is more sensitive to variations of the wood mechanical characteristics than the measurement with the average of support rotation  $\varphi_0$ . Moreover it is observed that  $D_\varepsilon$  is a local measurement of the bending stiffness and is therefore sensitive to local variations. It is also observed that the measured compliance  $\frac{1}{D_f}$  is also an average on the whole span of the beam and is closer to  $\frac{1}{D_\varphi}$  than to  $\frac{1}{D_{\Delta f}}$  (Figure 2.10). Finally,  $\frac{1}{F_f}$  is an average of the shear compliance  $\frac{1}{F(x)}$  on the span between supports and loads.

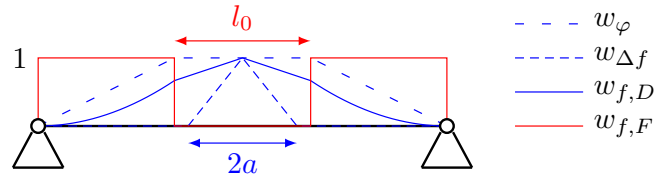


Figure 2.10 – Weight functions for the integration of the bending compliance and the shear compliance over the beam

## CHAPTER 2. EXPERIMENTAL DETERMINATION OF THE EQUIVALENT-LAYER SHEAR STIFFNESS OF CLT THROUGH FOUR POINT BENDING OF SANDWICH BEAMS

It can thus be concluded that, since there is a variability of wood characteristics in CLT cross-layer, the estimation of  $D$  based on  $\varphi_0$  will be more reliable and will *a priori* present a reduced standard deviation compared to estimations with  $\Delta f$  and  $\Delta \varepsilon$ . This will be confirmed in Section 2.4.

### 2.3.3 Experimental setup

The experimental setup is presented in Figure 2.11. Specimen are supported on two cylinders of radius  $R = 20\text{mm}$  on a span  $l = 600\text{mm}$ . They are loaded vertically and symmetrically by two cylinders of radius  $r = 4\text{mm}$  spaced of a length  $l_0 = 200\text{mm}$ . Steel plates are setup between specimen and cylinders to mitigate local punching. Several sensors are set up to measure variables introduced in Section 2.3.2:

- Five linear variable differential transformers (LVDTs) are placed on the frame. Three of them measure the vertical deflection on the lower axis of the beam: one at mid-span ( $f_A$ ), the two others on both sides at a distance  $a$  of 80mm from the mid-span ( $f_B$  and  $f_{B'}$ ). The two remaining LVDTs are located on the upper axis to measure the vertical settlement on supports.
- Two inclinometers are screwed into the wooden core on cantilevers on both sides of the specimen to measure the end rotation ( $\varphi_C$  and  $\varphi_{C'}$ );
- Two strain gauges are glued on the upper ( $\epsilon_{11}^+$ ) and the lower skins ( $\epsilon_{11}^-$ ) close to the mid-span.

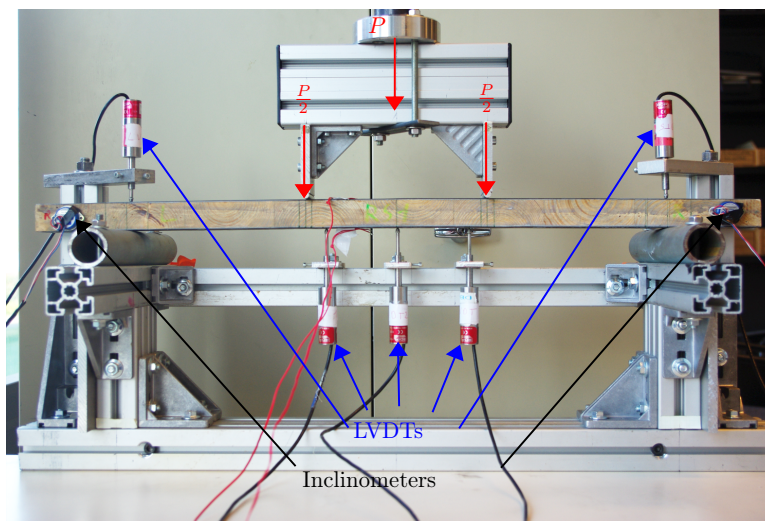


Figure 2.11 – Experimental setup

The specimen is loaded with a monitored vertical displacement up to 2.5mm, then unloaded to 1.0mm, next reloaded to 2.5mm and finally totally unloaded (Figure 2.12).

## 2.4. IDENTIFICATION OF THE EQUIVALENT CROSS-LAYER SHEAR STIFFNESS

Thus, the specimen is never loaded more than 30% of the failure load measured by Franzoni et al. (2017b) at 1.7 MPa in order to remain within the elastic range. The testing speed is set to 3mm/min so that the measurement time is approximately one minute to mitigate viscoelastic effects. Moduli measurements are derived from the reloading steps to avoid rigid body motions and tolerance recovering by linear regression between the load  $P$  and  $\Delta f$ ,  $\varphi_0$ ,  $\Delta\varepsilon$  and  $f_A$ .

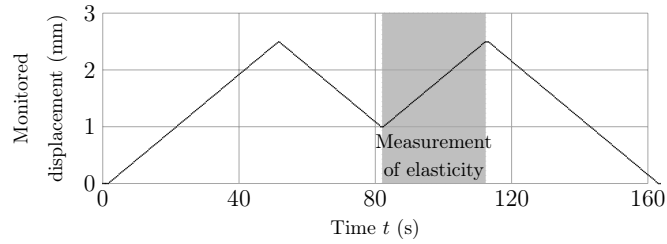


Figure 2.12 – Experimental loading sequence

## 2.4 Identification of the equivalent cross-layer shear stiffness

### 2.4.1 Deflections and rotations during loading and unloading

In this section, results are plotted during the whole experiment in order to determine the best data to fit linear regressions in order to measure the elastic linear behavior of the sandwich beam. Here, results are plotted for the experiment RS1-3.

In Figure 2.13 the force-deflection diagram between the applied force  $P$  and the mid-span deflection is plotted for the four steps of the experiment. A difference of slope is observed between the first loading phase and the following phases. The first loading is usually overlooked because of several deformations:

- plastic deformations at supports and under loads due to stress concentration
- non-linear geometrical deformations due to Herzian contact between a rigid cylinder and the beam which affects only the early stage of the loading
- settlement effects during the first loading due to contact imperfections at the beginning of the experiment

In Figure 2.13 the force-rotation diagram between the applied force  $P$  and the relative rotation at supports  $\varphi_0$  is plotted. In Figure 2.14, the force deflection diagram between the applied force  $P$  and the relative deflection  $\Delta f$  is also plotted. In Figure 2.14, the force deformation diagram between the applied force  $P$  and the relative deformation  $\Delta\varepsilon$  is also plotted. Similarly, a difference of slope is observed between the first phase and the following phases. This difference is more visible in Figure 2.14(left)

CHAPTER 2. EXPERIMENTAL DETERMINATION OF THE EQUIVALENT-LAYER SHEAR STIFFNESS OF CLT THROUGH FOUR POINT BENDING OF SANDWICH BEAMS

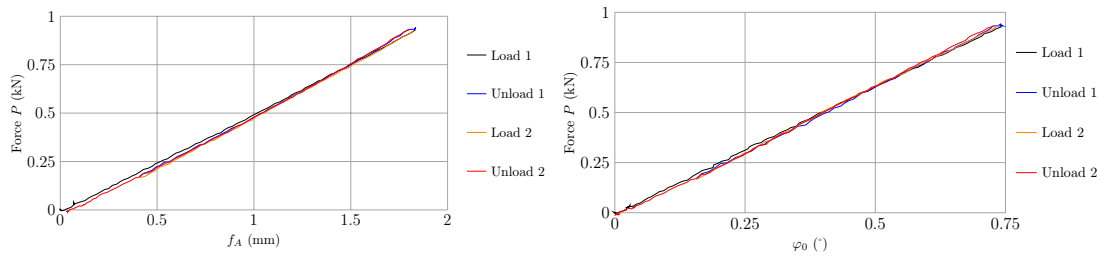


Figure 2.13 – Force-Deflection diagram for the mid-span deflection  $f_A$  (left) and force-rotation diagram for the relative rotation at support  $\varphi_0$  (right)

compared to the others. Moreover, the slope is not constant during the three last phases for the diagram with  $\Delta f$  (Figure 2.14). A linear regression seems more relevant for  $P > 0.5kN$  than on the whole reloading phase. Finally, the noise is more visible in Figure 2.14(left) than in Figure 2.13. This difference can be partly explained by the relative importance of the measured variable compared to the global deformations. Indeed, the relative deflection  $\Delta f$  measured here are only 7% of the total deflection  $f_A$ , which is approximately 10% of the total bending deflection and not representative of the global bending of the beam. On the contrary, the rotations  $\varphi_C$  and  $\varphi_{C'}$  are of the same order of magnitude of the ratio between mid-span deflection  $f_A$  and mid-span length  $\frac{l}{2}$ .  $\Delta f$  is then more sensitive to second order effects and to local defects than  $\varphi_0$ ,  $f_A$  and  $\Delta \varepsilon$ .

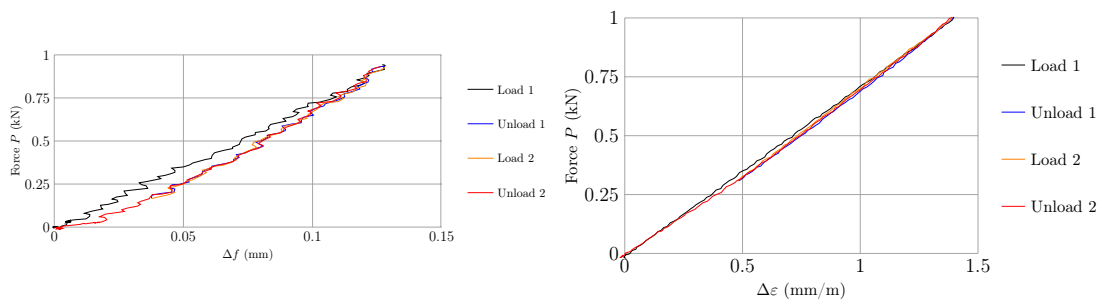


Figure 2.14 – Force-Deflection diagram for the relative deflection  $\Delta f$  (left) and Force-Deformation diagram for the relative deformation  $\Delta \varepsilon$  (right)

In Figure 2.15, the force  $P$  is plotted as a function of the skew-symmetric part of the deflection  $\frac{f_B - f_{B'}}{2}$ . The skew-symmetric deflections are not negligible compared to the relative deflection  $\Delta f$  which show the necessity of two LVDTs on both sides of the specimen. Indeed, since only  $P$ , the symmetrical part of the load, is known here, it must be plotted as a function of the symmetrical part of deflections which is not measurable without LVDTs on both sides of the experiment. Moreover, a great part of these deflections are due to inelastic deformations during the first loading. After this loading, the skew-symmetric deflection remains relatively constant when  $P > 0.5$  kN.

## 2.4. IDENTIFICATION OF THE EQUIVALENT CROSS-LAYER SHEAR STIFFNESS

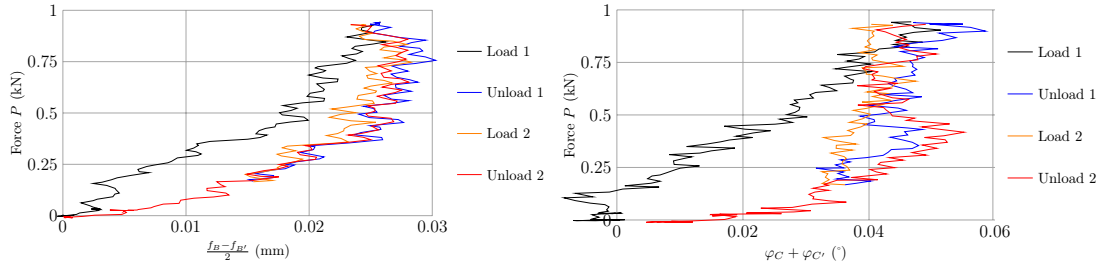


Figure 2.15 – Force-Deflection diagram for anti-symmetrical deflection at  $B$  and  $B'$  (left) and force-rotation diagram for anti-symmetrical rotation at support (right)

In Figure 2.15, the force  $P$  is plotted as a function of the skew-symmetric part of end rotations  $\varphi_C + \varphi_{C'}$ . As observed previously, most of skew-symmetric rotations are due to the inelastic deformations during the first loading phase. Nevertheless, these rotations are small compared to the relative rotation  $\varphi_0$ .

From these observations, we conclude that the linear regression must be done during the second loading phase and a careful attention has to be paid to the uniformity of the slope particularly for a low force  $P$  and for the diagram of  $P$  as a function of  $\Delta f$ . Moreover, a higher sensitivity to second-order effects was observed for the measurement of  $\Delta f$  compared to measurements of  $\varphi_0$ ,  $\Delta\varepsilon$  and  $f_A$ . Finally, non negligible skew-symmetric deflections are observed showing the importance of two sensors on both sides of the experiment for each measurement.

### 2.4.2 Stiffness measurements

In Table 2.3 the CFRP skins apparent Young modulus  $E_{L,CFRP}$  is given for each specimen.  $E_{L,CFRP}$  stands for the two sets of CFRP used in this study. Four specimen have been tested using the three methods of measurement (RS1-1, RS1-2, RS1-3, RS2-1). Stronger variations and lower values are observed for measurement obtained from  $\Delta f$  than measurement from  $\varphi_0$  and  $\Delta\varepsilon$ . This low measured bending stiffness lead to high measured equivalent cross-layer shear modulus  $G_{CZ}$  (Table 2.4) particularly for RS1-1 where  $G_{CZ} = 412$  MPa according to  $\Delta f$  measurement which is inconsistent with other methods and which show the poor reliability of this measurement. Results with the two other methods ( $\varphi_0$  and  $\Delta\varepsilon$ ) seems more reliable since they are close to each other. The relative difference between  $E_{L,CFRP}$  measured from  $\Delta\varepsilon$  and from  $\varphi_0$  is less than 6%. The skins modulus  $E_{L,CFRP}$  (resp. wooden core shear stiffness  $G_{CZ}$ ) measured with rotation at ends  $\varphi_0$  is always larger (resp. smaller) than the modulus measured with relative strain  $\Delta\varepsilon$ . This relative difference is much higher than the one observed from 3D results (Table 2.2). Considering these results, only the measurements of  $E_{L,CFRP}$  and  $G_{CZ}$  from  $\varphi_0$  is performed in the rest of the tests (RS2-2 to RS2-9).

The average of the equivalent cross-layer shear stiffness  $G_{CZ}$  is finally 124 MPa.

CHAPTER 2. EXPERIMENTAL DETERMINATION OF THE EQUIVALENT-LAYER SHEAR STIFFNESS OF CLT THROUGH FOUR POINT BENDING OF SANDWICH BEAMS

Specimen	CFRP	$\Delta f$	$\varphi_0$	$\Delta \varepsilon$
RS1-1	Set 1	99.7	132	130
RS1-2	Set 1	115	131	123
RS1-3	Set 1	115	127	122
RS2-1	Set 2	97.2	110	104
RS2-2	Set 2	-	111	-
RS2-3	Set 2	-	117	-
RS2-4	Set 2	-	112	-
RS2-5	Set 2	-	112	-
RS2-6	Set 2	-	104	-
RS2-7	Set 2	-	96.8	-
RS2-8	Set 2	-	103	-
RS2-9	Set 2	-	101	-
Average	Set 1 (Set 2)	110 (97.2)	130 (106)	125 (104)
COV (%)	Set 1 (Set 2)	8.15 (-)	2.01 (6.31)	3.28 (-)
Number	Set 1 (Set 2)	3 (1)	3 (9)	3 (1)

Table 2.3 –  $E_{L,CFRP}$  (GPa) measures from  $\Delta f$ ,  $\varepsilon_0$  and  $\Delta \varepsilon$

This value is in agreement with Voigt and Reuss bounds calculated in Chapter 1. Moreover, this value is higher than the equivalent rolling shear modulus measured by Franzoni et al. (2017b) on the same batch of wood. This difference is mainly due to the edge gluing in the present test whereas narrow edge are free in (Franzoni et al., 2017b) as observed numerically in Chapter 1. Finally, the relevance of the proposed methodology is then illustrated through the low coefficient of variation (6.71%) compared to single-lap shear test from Franzoni et al. (2017b) (27%) due to averaging effects which a consequence of the numerous boards in a single specimen. The use of measurements based on the rotation and long size specimen also reduces drastically the variability.

## 2.5 Conclusion

In this chapter, we proposed a new methodology to identify experimentally the equivalent shear stiffness at the layer scale by using flexural test on sandwich structures. In this four point bending, we advocate for a measure using inclinometers to identify the bending stiffness from the ends rotation, the estimation is more reliable than with the classical estimation based on relative displacement at mid-span. This better accuracy is partly due to the averaging effects of rotation compared to the relative deflection

## 2.5. CONCLUSION

Specimen	$\Delta f$	$\varphi_0$	$\Delta \varepsilon$			
RS1-1	412	131	137			
RS1-2	185	131	152			
RS1-3	171	131	145			
RS2-1	154	110	128			
RS2-2	-	129	-			
RS2-3	-	118	-			
RS2-4	-	120	-			
RS2-5	-	110	-			
RS2-6	-	135	-			
RS2-7	-	124	-			
RS2-8	-	126	-			
RS2-9	-	122	-	(Franzoni et al., 2017b)	Upper bound	Lower bound
Average	231	124	140	110	125	83.2
COV (%)	52.9	6.71	7.41	27		
Number	4	12	4	10		

Table 2.4 –  $G_{CZ}$  (MPa) measures from  $\Delta f$ ,  $\varepsilon_0$  and  $\Delta \varepsilon$

between loading points. The measurement of rotation is also significantly less sensitive to the quality and the precision of sensors setup compared to the measurement of the variations of deflection.

Then, we conducted a first experimental campaign on these sandwich structure and confirmed the reliability of the method. Indeed, the equivalent cross-layer shear modulus of the sample was estimated at 124 MPa with a coefficient of variation of 6.71% which is remarkably low for wood characteristics. The simultaneous testing of several boards in a single sandwich is very beneficial.

To go further, we look forward to use this methodology to study the viscoelastic behavior of the equivalent cross-layer shear stiffness of timber which is needed to design Cross-Laminated-Timber in the long term. Currently, only few studies on the viscoelastic behavior of Cross-Laminated-Timber panels have been published to the authors knowledge (Jöbstl and Schickhofer, 2007; Pirvu and Karacabeyli, 2014; Colling, 2014; Li, 2015). In all these studies, the whole CLT panels are tested and the viscoelastic behavior of the cross-layer is not directly identified. Recently, specimen used in this study have been put into four point bending test during several months to identify directly the creep due to the cross-layer shear of timber at constant climate.

## **Part II**

---

# **Stability of CLT walls at short and long term**



---

# The Bending-Gradient theory for the linear buckling of thick plates: Application to Cross-Laminated-Timber panels

*In the first part of this PhD thesis, the equivalent-layer stiffness of CLT has been defined and an experimental protocol has been defined to measure the equivalent cross-layer shear stiffness. Then, from these equivalent homogeneous behavior, it is possible to derive the linear elastic behavior of CLT. We first introduce the buckling problem of a CLT panel without initial imperfections using the Bending-Gradient theory. This chapter was published in the International Journal of Solids and Structures (Perret et al., 2016)*

## 3.1 Introduction

Cross Laminated Timber (CLT) is an innovative wooden structural product which consists in several lumber layers stacked crosswise and glued on their wide faces. CLT constructions are assembled relatively quickly compared to buildings in steel or concrete and combine a low self-weight and high membrane and bending stiffnesses. These attributes make it competitive prefabricated structures with a low environmental impact. CLT panels are classically used in walls, floors and roofs as load carrying plate elements. Thus, several studies were performed to model the bending of CLT plates (Stürzenbecher et al., 2010; Guggenberger and Moosbrugger, 2006; Franzoni et al., 2016b, 2017a,b).

CLT was introduced in Austria and Germany in the early 1990s (Stürzenbecher et al., 2012). During the last twenty years, CLT structures have gained in popularity and taller and taller buildings are designed every year. As an example, the building Stadthaus, at Murray Grove in London (Lomholt, 2015), is the tallest modern timber building in the world. This nine-storey building is entirely designed in CLT except for the first floor. Until now, loads involved in timber buildings were relatively far from design limits. Nevertheless, with the increasing size of timber buildings such as the Ho-Ho building project at Vienna in Austria which will be 84-meters high (French,

### 3.1. INTRODUCTION

---

2015), higher compressive stresses will be involved in bearing walls and could lead to buckling. Although CLT walls are thick, they are made of a highly anisotropic material and this anisotropy could lead to a lower buckling load than predicted with the classical lamination theory. Indeed, the shear stiffness between radial and tangential directions in timber, called also rolling-shear, is two hundred times lower than the stiffness in fibers' direction. As rolling shear is involved in cross layers during buckling, taking it into account seems important with such a contrast.

Yet, the combination of such an anisotropy with thick sections is relatively new in the domain of composite materials. In the Eurocode 5 (European Committee for Standardisation, 1993) for the design of timber constructions, the buckling load is derived from the Euler-buckling of slender beams where the transverse shear strain is neglected. In order to take into account long term loading, imperfections and possible transverse shear effects, several safety coefficients are introduced. Nevertheless, these coefficients often lead to oversized timber structures which are then less competitive than structures made of steel or concrete. Thus, using a more appropriate theory to design timber structures could lead to more competitive CLT buildings.

Since one of the dimensions of CLT panels, the thickness, is significantly lower than the others, plate theories are appropriate to model CLT panels. Thus, the 3D problem can be reduced to a 2D one associated with a chosen reference surface and a lower number of variables than the full problem. In these theories, called Equivalent Single Layer (ESL) theories, properties of interest are integrated through the thickness of the plate and transposed to the single layer model. These theories often follow an axiomatic approach since they are derived from displacement and/or stress field distribution assumptions. The simplest example is the classical lamination theory for thin plates, or Classical Plate Theory (CPT), derived from the Kirchhoff-Love plate theory (Kirchhoff, 1850; Love, 1888). In this theory, the main assumptions are: cross-sections remain plane and normal to the mid-plane section (no transverse shear); the transverse normal stress is negligible compared to in-plane stress. To comply with these assumptions, the in-plane displacement is assumed to vary linearly through the thickness:  $u_\alpha = -x_3 U_{3,\alpha}$  and the out-of plane displacement  $u_3 = U_3$  is assumed to be constant through the thickness and equal to mid-plane deflection. The CPT converges to the exact 3D solution when increasing the slenderness of the plate (Ciarlet and Destuynder, 1979; Ciarlet, 1997). In his technical report, Leissa (1985) provided a large overview of the buckling of rectangular laminated composites by considering several loading configurations, boundary conditions and geometries of orthotropic and anisotropic laminates mainly based on the classical lamination theory. He also pointed the necessity to consider shear effects, which are neglected in the CPT, when the thickness of the plate increases.

In order to capture shear effects in the plate, Hencky (1947) suggested another in-plane displacement field distribution by introducing the rotation field  $\varphi_\alpha$  adding then two new variables. The in-plane displacement is there defined as  $u_\alpha = x_3 \varphi_\alpha$  and the

transverse shear strain as  $\gamma_\alpha = U_{3,\alpha} + \varphi_\alpha$ . Thus, the so-called first-order shear deformation theory (FOSDT) leads to a uniform transverse shear strain distribution through the thickness. Since the actual distribution of the transverse shear stress is at least quadratic through the thickness, the transverse shear stiffness is often adjusted with a shear correction factor  $\kappa$ . For homogeneous plates, values of  $\frac{5}{6}$  or  $\frac{\pi^2}{12}$  are used by Reissner (1945) and Mindlin (1951) respectively. Even if this theory is also called the Reissner-Mindlin theory, Reissner's model is based on static assumptions: indeed he assumes a parabolic distribution of the transverse shear stress which does not exactly correspond to Hencky's kinematic. The FOSDT was extended to heterogeneous plate by Yang et al. (1966) to study the propagation of harmonic waves in laminated plates. Whitney and Pagano (1970) applied the same procedure as Yang et al. (1966) to the problems of cylindrical bending, bending of rectangular plates and natural frequencies. Results presented by the FOSDT are more accurate than the CPT, in particular for thick and highly anisotropic plates. Nevertheless, applying directly the FOSDT to laminated plates leads to an inaccurate description of the local stress field since it does not ensure transverse shear stress continuity at layers interfaces. Chow (1971) then Whitney (1972) suggested to include shear correction factors adapted to laminated composites by considering the cylindrical bending of a laminate. The lamination scheme and the shear stress continuity across thickness are considered to estimate these correction factors. Concerning buckling, Noor (1975) studied the symmetrical and unsymmetrical laminated composite and showed that the Reissner-Mindlin's theory gives good results for the critical load of such laminates compared to a mixed finite-difference scheme suggested by Noor (1973) provided that shear correction factors are well determined.

As an improvement of the FOSDT, higher-order shear deformation theories (HOSDT) were introduced to provide a better shear strain distribution through the thickness and to guaranty shear stress boundary conditions at the top and bottom surfaces without the use of correction factors. One of the first HOSDT was suggested by Kączkowski (1980) who assumed a cubic distribution of the in-plane displacement while the out-of-plane displacement remains constant through the thickness. Alternative cubic forms were suggested by Ambartsumian (1970) and Levinson (1980). By considering zero shear stress at outer surfaces, the problem is rewritten by keeping only FOSDT's kinematic unknowns. Despite this simplification in the number of variables, two additional boundary conditions on the gradient of the deflection are introduced. Levinson (1980) showed that his theory gives exactly the same wave equation for the deflection as FOSDT with the shear correction factor  $\kappa = \frac{5}{6}$ , when studying natural frequencies. Moreover, this HOSDT presents more accurate results than FOSDT for static problems such as plate torsion (Levinson, 1980), or bending (Reddy, 1984), in particular for stress distribution. Following Kączkowski's example, several others HOSDT were suggested by considering various in-plane displacement distributions with the global form:  $u_\alpha(x_3) = x_3\varphi_\alpha + f(x_3)\zeta_\alpha$ .  $\zeta$  is an additional variable representing plate warping and

### 3.1. INTRODUCTION

---

$f$  a suitable function which approximates the actual distribution of the transverse shear strain through the thickness and which allows the shear stress to vanish at top and bottom surfaces. For example,  $f$  was considered polynomial (Kączkowski, 1980; Ambartsumian, 1970; Reissner, 1975; Levinson, 1980; Reddy, 1984) and trigonometric (Touratier, 1991). Concerning buckling, Phan and Reddy (1985) used the cubic form suggested by Reddy (1984) to study laminated composites. The buckling load given by the HOSDT is in good agreement with the three-dimensional solution of Noor (1973) and with the first order shear deformation theory with appropriate correction factors (Noor, 1975). It is pointed in this study that this HOSDT is an improvement of the FOSDT since it does not require shear correction factors.

Zig-zag theories (ZZT) are the most refined HOSDT and have been developed to model the actual piece-wise continuous displacement and transverse shear stress distributions through the thickness. These theories comply with the inter-laminar continuity of displacements and of transverse shear stress fields in multi-layered plates. In his review, Carrera (2003) distinguishes three kinds of ZZT based on works of Lekhnitskii (1935), Ambartsumian (1957a,b) and Reissner (1984). Lekhnitskii's work has been extended to orthotropic and anisotropic plates by Ren (1986b,a) and applied to buckling and free vibrations of laminated plates by Ren and Owen (1989) with accurate results. As pointed by Carrera (2003), most of other improvements or extensions of these theories are based on Ambartsumian model such as Whitney (1969). ZZT are well adapted but limited to composites with classical lamination scheme. Moreover they involved higher-order partial derivative equations than the Reissner-Mindlin model.

Lebée and Sab (2011a) suggested an improvement of the Reissner-Mindlin theory by considering every components of the gradient of the bending moment to describe the shear behavior of the plate. The Bending-Gradient theory is found to an exact extension of the Reissner-Mindlin model to mirror symmetric plates (Lebée and Sab, 2013). Four additional unknowns are used to take into account the cylindrical bending part and the torsional part of the shear force and to include warping effects. The Bending-Gradient (BG) theory is found to turn exactly into the Reissner-Mindlin model in the case of an homogeneous plate. Lebée and Sab (2011b) studied the case of the cylindrical bending of laminated plates and compared their results to the exact solution of Pagano (1969), to the solution provided by Whitney (1969) using a Reissner-Mindlin model and to a finite-element solution. The Bending-Gradient captures more efficiently displacement and stress fields for symmetrical laminates with non-orthotropic ply than the Reissner-Mindlin model. Indeed, in such laminates, the effect of warping is neglected in the model provided by Whitney (1972).

The aim of this chapter is to extend the Bending-Gradient theory to plate buckling and to apply it to CLT panels. We restrict our study to the case of rectangular plates uniformly loaded with the membrane stress  $N_{11}^0$  in  $x_1$ -direction. In section 3.2, the Bending-Gradient theory is briefly recalled and extended to linear buckling. The intro-

duction of two projections on a simplified Reissner-Mindlin model is also discussed. Then, in section 3.3, a 3D numerical study is conducted and provides reference results. Finally, analytic results from the Bending-Gradient theory, the CPT and the FOSDT are compared with reference results in section 3.4.

## 3.2 Linear buckling of plates with the Bending-Gradient theory

### 3.2.1 Notations

Vectors and higher-order tensors, up to sixth order, are used in the following. When using short notations, several underlining styles are used: vectors are straight underlined,  $\underline{\mathbf{u}}$ . Second order tensors are underlined with a tilde:  $\underline{\underline{\mathbf{M}}}$  and  $\underline{\underline{\boldsymbol{\sigma}}}$ . Third order tensors are underlined with a parenthesis:  $\underline{\underline{\mathbf{R}}}$  and  $\underline{\underline{\boldsymbol{\Gamma}}}$ . Fourth order tensors are doubly underlined with a tilde:  $\underline{\underline{\underline{\mathbf{D}}}}$  and  $\underline{\underline{\underline{\mathbf{C}}}}^\sigma$ . Sixth order tensors are doubly underlined with a parenthesis:  $\underline{\underline{\underline{\mathbf{h}}}}$ . The full notation with indices is also used. Einstein's notation is followed on repeated indices. Furthermore, Greek indices  $\alpha, \beta, \delta, \gamma = 1, 2$  denote in-plane dimensions and Latin indices  $i, j, k, l = 1, 2, 3$ , all three dimensions.

The transpose operation  ${}^T \bullet$  is applied to any order tensors as follows:  $({}^T a)_{\alpha\beta\dots\psi\omega} = a_{\omega\psi\dots\beta\alpha}$ . Three contraction products are defined, the usual dot product ( $\underline{\mathbf{a}} \cdot \underline{\mathbf{b}} = a_i b_i$ ), the double contraction product ( $\underline{\mathbf{a}} : \underline{\mathbf{b}} = a_{ij} b_{ji}$ ) and a triple contraction product ( $\underline{\mathbf{a}} : \underline{\mathbf{b}} = a_{\alpha\beta\gamma} b_{\gamma\beta\alpha}$ ). It should be noticed that closest indices are summed together in contraction products. The derivation operator  $\nabla$  is also formally represented as a vector so that  $\underline{\mathbf{a}} \cdot \nabla = a_{ij} \nabla_j = a_{ij,j}$  is the divergence and  $\underline{\mathbf{a}} \otimes \nabla = a_{ij} \nabla_k = a_{ij,k}$  is the gradient. Here  $\otimes$  is the dyadic product.  $\underline{\mathbf{a}} \otimes^s \nabla = a_i \nabla_j = \frac{1}{2} (a_{i,j} + a_{j,i})$  is the symmetric gradient of  $\underline{\mathbf{a}}$ .

### 3.2.2 The Bending-Gradient theory

Full details about the Bending-Gradient theory are provided in Lebée and Sab (2011a,b); Sab and Lebée (2015); Lebée and Sab (2015b,a).

#### 3.2.2.1 Generalized stress and strain fields

We consider a linear elastic plate of constant thickness  $h$  and characteristic length  $L$  which mid-plane is the 2D domain  $\omega$  (Figure 3.1). The 3D domain is then defined as  $\Omega = \omega \times [-h/2, h/2]$ . Cartesian coordinates  $x_1, x_2, x_3$  are used in the reference frame  $(\underline{\mathbf{e}}_1, \underline{\mathbf{e}}_2, \underline{\mathbf{e}}_3)$ . The plate is loaded with the distributed load  $\underline{\mathbf{p}}_3 = p_3(x_1, x_2)\underline{\mathbf{e}}_3$  in the transverse direction. The 3D constitutive tensor  $\underline{\underline{\underline{\mathbf{C}}}}$  is monoclinic with respect to  $(\underline{\mathbf{e}}_1, \underline{\mathbf{e}}_2)$ -plane:  $C_{\alpha\beta\gamma 3} = C_{333\alpha} = 0$ . Moreover the plate follows mirror symmetry

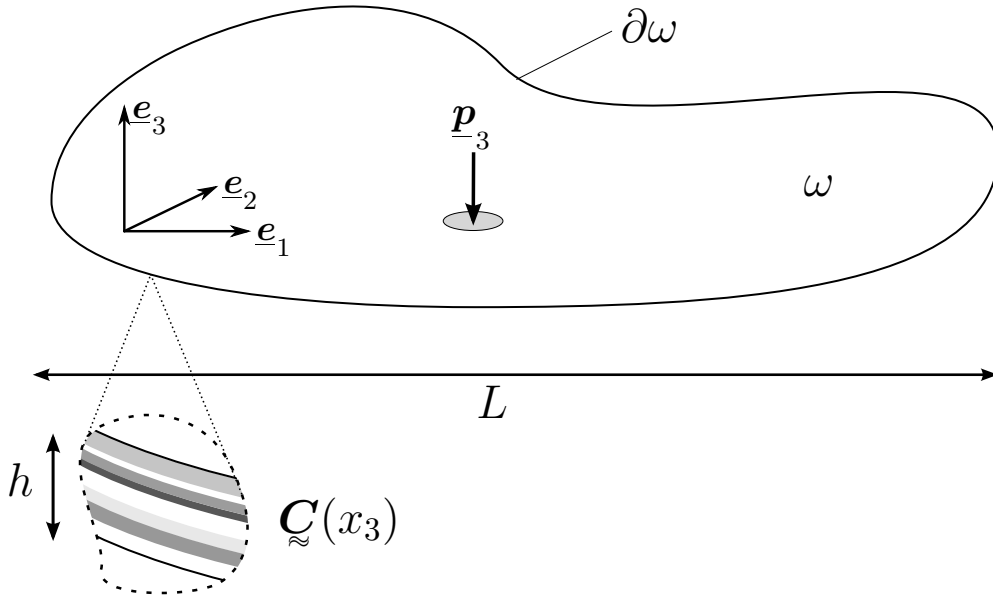


Figure 3.1 – 2D plate under out-of-plane loading

according to  $\omega$ , in other words  $\underline{\underline{C}}$  is an even function of  $x_3$ . The conventional generalized stresses for plates in bending are defined from the 3D stress field  $\sigma_{ij}$  as follows:

$$\begin{cases} M_{\alpha\beta} = \int_{-\frac{h}{2}}^{\frac{h}{2}} x_3 \sigma_{\alpha\beta} dx_3 & \text{on } \omega \\ Q_\alpha = \int_{-\frac{h}{2}}^{\frac{h}{2}} \sigma_{\alpha 3} dx_3 & \text{on } \omega \end{cases} \quad (3.1a)$$

$$\quad (3.1b)$$

where  $M_{\alpha\beta}$  is the bending moment and  $Q_\alpha$  the shear force. Integrating the 3D equilibrium equation leads to the following Reissner-Mindlin plate equilibrium equation:

$$\begin{cases} M_{\alpha\beta,\beta} = Q_\alpha \\ Q_{\alpha,\alpha} + p_3 = 0 \end{cases} \iff \begin{cases} \underline{\underline{M}} \cdot \underline{\nabla} = \underline{\underline{Q}} \\ \underline{\underline{Q}} \cdot \underline{\nabla} + p_3 = 0 \end{cases} \quad (3.2)$$

In the Reissner-Mindlin model,  $\underline{\underline{M}}$  and  $\underline{\underline{Q}}$  are in duality with the curvature  $\underline{\underline{\chi}} = \underline{\varphi} \otimes^s \underline{\nabla}$  and the transverse shear strain  $\underline{\underline{\gamma}} = \underline{\varphi} + \underline{\nabla} U_3$  where  $U_3$  is the deflection and  $\underline{\varphi}$  the rotation.  $\underline{\underline{M}}$  follows the classical symmetry of stress tensors:  $M_{\alpha\beta} = M_{\beta\alpha}$ . In the Bending-Gradient theory, an additional static unknown is introduced: the generalized shear force  $R_{\alpha\beta\gamma} = M_{\alpha\beta,\gamma}$ . The 2D third-order tensor  $\underline{\underline{R}}$  complies with the following symmetry:  $R_{\alpha\beta\gamma} = R_{\beta\alpha\gamma}$ . It is possible to derive the shear force  $\underline{\underline{Q}}$  from  $\underline{\underline{R}}$  with:  $Q_\alpha =$

CHAPTER 3. THE BENDING-GRADIENT THEORY FOR THE LINEAR BUCKLING OF THICK PLATES: APPLICATION TO CROSS-LAMINATED-TIMBER PANELS

$R_{\alpha\beta\beta}$  or  $\underline{\mathbf{Q}} = \underline{\mathbf{i}} : \underline{\mathbf{R}}$ .  $\underline{\mathbf{i}}$  is the identity for in-plane tensor:  $i_{\alpha\beta\gamma\delta} = \frac{1}{2}(\delta_{\alpha\gamma}\delta_{\beta\delta} + \delta_{\alpha\delta}\delta_{\beta\gamma})$  where  $\delta_{\alpha\beta}$  is the Kronecker symbol  $\delta_{\alpha\beta} = 1$  if  $\alpha = \beta$  and 0 if  $\alpha \neq \beta$ .

The main difference between Reissner-Mindlin and Bending-Gradient plate theories is that the latter enables the distinction between each components of the gradient of the bending moment whereas they are mixed into the shear force with the Reissner-Mindlin theory. The full bending gradient  $\underline{\mathbf{R}}$  has six components whereas  $\underline{\mathbf{Q}}$  has two components. Thus, using the full bending gradient as a static unknown introduces four additional static variables. More precisely:  $R_{111}$  and  $R_{222}$  are the cylindrical bending parts of shear forces  $Q_1$  and  $Q_2$  respectively,  $R_{121}$  and  $R_{122}$  are the torsion parts of these shear forces respectively and  $R_{112}$  and  $R_{221}$  are linked to strictly self-equilibrated stresses.

By generalizing the Reissner-Mindlin equilibrium (3.2), the Bending-Gradient equilibrium equations are:

$$\begin{cases} R_{\alpha\beta\gamma} = M_{\alpha\beta,\gamma} \\ R_{\alpha\beta\beta,\alpha} + p_3 = 0 \end{cases} \iff \begin{cases} \underline{\mathbf{R}} = \underline{\mathbf{M}} \otimes \underline{\mathbf{\nabla}} \\ (\underline{\mathbf{i}} : \underline{\mathbf{R}}) \cdot \underline{\mathbf{\nabla}} + p_3 = 0 \end{cases} \quad \text{on } \omega \quad (3.3)$$

Generalized stresses  $\underline{\mathbf{M}}$  and  $\underline{\mathbf{R}}$  work with the associated strain variables: the curvature  $\underline{\mathbf{\chi}}$  and the generalized shear strain  $\underline{\mathbf{\Gamma}}$  respectively. These strain fields must comply with the compatibility equations:

$$\begin{cases} \chi_{\alpha\beta} = \Phi_{\alpha\beta\gamma,\gamma} \\ \Gamma_{\alpha\beta\gamma} = \Phi_{\alpha\beta\gamma} + i_{\alpha\beta\gamma\delta} U_{3,\delta} \end{cases} \iff \begin{cases} \underline{\mathbf{\chi}} = \underline{\mathbf{\Phi}} \cdot \underline{\mathbf{\nabla}} \\ \underline{\mathbf{\Gamma}} = \underline{\mathbf{\Phi}} + \underline{\mathbf{i}} \cdot \underline{\mathbf{\nabla}} U_3 \end{cases} \quad (3.4)$$

where  $\underline{\mathbf{\Phi}}$  is the third-order tensor related to generalized rotations.  $\underline{\mathbf{\Phi}}$  and  $\underline{\mathbf{\Gamma}}$  are 2D-third-order tensors following the symmetry  $\Phi_{\alpha\beta\gamma} = \Phi_{\beta\alpha\gamma}$ ,  $\Gamma_{\alpha\beta\gamma} = \Gamma_{\beta\alpha\gamma}$ .

### 3.2.2.2 Bending-Gradient constitutive equations

The Bending-Gradient plate constitutive equations are:

$$\begin{cases} M_{\alpha\beta} = D_{\alpha\beta\gamma\delta} \chi_{\delta\gamma} \\ \Gamma_{\alpha\beta\gamma} = h_{\alpha\beta\gamma\delta\epsilon\zeta} R_{\zeta\epsilon\delta} \end{cases} \iff \begin{cases} \underline{\mathbf{M}} = \underline{\mathbf{D}} : \underline{\mathbf{\chi}} \\ \underline{\mathbf{\Gamma}} = \underline{\mathbf{h}} : \underline{\mathbf{R}} \end{cases} \quad \text{on } \omega \quad (3.5)$$

where  $\underline{\mathbf{D}} = \underline{\mathbf{d}}^{-1}$  is the conventional Kirchhoff-Love fourth-order bending tensor classically defined as follows:

$$D_{\alpha\beta\gamma\delta} = \int_{-\frac{h}{2}}^{\frac{h}{2}} x_3^2 C_{\alpha\beta\gamma\delta}^\sigma(x_3) dx_3 \quad (3.6)$$

### 3.2. LINEAR BUCKLING OF PLATES WITH THE BENDING-GRADIENT THEORY

$$\text{with } C_{\alpha\beta\gamma\delta}^{\sigma} = C_{\alpha\beta\gamma\delta} - \frac{C_{\alpha\beta 33}C_{\gamma\delta 33}}{C_{3333}}$$

Here,  $\underline{\underline{C}}^{\sigma}$  is the plane stress elasticity tensor and  $\underline{\underline{C}}$  is the fourth-order 3D elasticity stiffness tensor.

The sixth-order generalized shear compliance tensor  $\underline{\underline{h}}$  is then defined as follows:

$$\underline{\underline{h}} = \int_{-\frac{h}{2}}^{\frac{h}{2}} \left( \int_{-\frac{h}{2}}^{x_3} z \underline{\underline{d}} : \underline{\underline{C}}^{\sigma} dz \right) \cdot \underline{\underline{g}} \cdot \left( \int_{-\frac{h}{2}}^{x_3} z \underline{\underline{C}}^{\sigma} : \underline{\underline{d}} dz \right) dx_3 \quad (3.7)$$

where  $g_{\alpha\beta}(x_3) = (C_{\alpha 3\beta 3})^{-1}$  is the out-of-plane transverse shear compliance tensor. The fourth-order tensor  $\underline{\underline{D}}$  and the sixth order tensor  $\underline{\underline{h}}$  follow the major symmetry:  $D_{\alpha\beta\gamma\delta} = D_{\delta\gamma\beta\alpha}$ ,  $h_{\alpha\beta\gamma\delta\epsilon\zeta} = h_{\zeta\epsilon\delta\gamma\beta\alpha}$  and the minor symmetry:  $D_{\alpha\beta\gamma\delta} = D_{\beta\alpha\gamma\delta}$ ,  $h_{\alpha\beta\gamma\delta\epsilon\zeta} = h_{\beta\alpha\gamma\delta\epsilon\zeta}$ .

The tensor  $\underline{\underline{h}}$  is not always positive definite. For this reason, the Moore-Penrose pseudo-inverse is introduced:

$$\underline{\underline{H}} = \lim_{\kappa \rightarrow 0} \left( \underline{\underline{h}} : \underline{\underline{h}} + \kappa \underline{\underline{I}} \right)^{-1} : \underline{\underline{h}} \quad (3.8)$$

where  $I_{\alpha\beta\gamma\delta\epsilon\zeta} = i_{\alpha\beta\gamma\delta\epsilon\zeta} \delta_{\gamma\delta}$  is the sixth-order identity tensor. For example the Moore-Penrose pseudo-inverse of  $\begin{pmatrix} \lambda & 0 \\ 0 & 0 \end{pmatrix}$  is  $\begin{pmatrix} 1/\lambda & 0 \\ 0 & 0 \end{pmatrix}$ . Thus, the reciprocal relationship of Equation (3.5) may be introduced:

$$R_{\alpha\beta\gamma} = H_{\alpha\beta\gamma\delta\epsilon\zeta} \Gamma_{\zeta\epsilon\delta} \iff \underline{\underline{R}} = \underline{\underline{H}} : \underline{\underline{\Gamma}} \text{ on } \omega \quad \text{for } \underline{\underline{\Gamma}} \in \text{Im} \left( \underline{\underline{h}} \right)$$

where  $\text{Im} \left( \underline{\underline{h}} \right) \subseteq (\mathbb{R}^2)^3$  is the image of the sixth-order tensor  $\underline{\underline{h}}$ .

#### 3.2.2.3 Projections of the Bending-Gradient model on Reissner-Mindlin models

In the case of a homogeneous plate, it was demonstrated that the Bending-Gradient model is strictly reduced to a Reissner-Mindlin model (Lebée and Sab, 2011a). Indeed, it can be shown that in this case:

$$h_{\alpha\beta\gamma\delta\epsilon\zeta} = i_{\alpha\beta\gamma\eta} f_{\eta\theta}^R i_{\theta\delta\epsilon\zeta} \iff \underline{\underline{h}} = \underline{\underline{i}} \cdot \underline{\underline{f}}^R \cdot \underline{\underline{i}} \quad (3.9)$$

where  $f_{\alpha\beta}^R = \frac{6h}{5} g_{\alpha\beta}$  is the shear force compliance tensor classically used in the Reissner-Mindlin model. For this reason, the Bending-Gradient theory can be seen as an extension to heterogeneous plates of the Reissner-Mindlin theory. It is thus suggested here to investigate projections of the Bending-Gradient on a Reissner-Mindlin model. Even if these projections are less accurate than the Bending-Gradient model, some of them

may be applicable to a given problem with a good accuracy. In the present work, two relevant projections are tested to provide a Reissner-Mindlin shear constitutive law  $\underline{f}$  (or  $\underline{F}$ ) from the generalized shear constitutive law  $\underline{h}$ .

**3.2.2.3.1 Shear Compliance Projection (SCP)** The components of the generalized shear tensor  $\underline{R}$  may be rewritten as :

$$Q_\alpha = R_{\alpha\beta\beta}, \quad R_{221}, \quad R_{112},$$

$$\Delta Q_1 = R_{111} - 2R_{122}, \quad \Delta Q_2 = R_{222} - 2R_{121}$$

where  $\Delta Q_1$ ,  $\Delta Q_2$ ,  $R_{221}$  and  $R_{112}$  are four self-equilibrated static unknowns. They are clearly set apart from shear forces  $Q_\alpha$ . Thus, we assume that these unknowns do not contribute to the transverse shear energy and keep only the contribution of Reissner-Mindlin shear forces  $Q_1$  and  $Q_2$ . This is equivalent to set  $\underline{R} = \frac{2}{3}\underline{i} \cdot \underline{Q}$  in the shear stress energy and leads to:

$$W^{*BG,R}(R) = \frac{1}{2} {}^T \underline{R} : \underline{h} : \underline{R} = \frac{1}{2} {}^T \left( \frac{2}{3} \underline{i} \cdot \underline{Q} \right) : \underline{h} : \left( \frac{2}{3} \underline{i} \cdot \underline{Q} \right)$$

$$= \frac{1}{2} {}^T \underline{Q} \cdot \left[ \left( \frac{2}{3} \underline{i} \right) : \underline{h} : \left( \frac{2}{3} \underline{i} \right) \right] \cdot \underline{Q}$$

Consequently, the Reissner-Mindlin shear stress energy is obtained with the following projection of  $\underline{h}$ :

$$\underline{f}^{sc} = \left( \frac{2}{3} \underline{i} \right) : \underline{h} : \left( \frac{2}{3} \underline{i} \right)$$

$$\begin{cases} f_{11}^{sc} &= \frac{4}{9} (h_{111111} + h_{122221} + 2h_{111221}) \\ f_{12}^{sc} &= f_{21}^{sc} = \frac{4}{9} (h_{111121} + h_{111222} + h_{121221} + h_{222221}) \\ f_{12}^{sc} &= \frac{4}{9} (h_{222222} + h_{121121} + 2h_{121222}) \end{cases} \quad (3.10)$$

This projection is used by Lebée and Sab (2011a,b) to evaluate the distance between Bending-Gradient and Reissner-Mindlin models.

**3.2.2.3.2 Shear Stiffness Projection (SSP)** Another possible projection is obtained assuming, for the generalized rotation field, the particular form  $\underline{\Phi} = \underline{i} \cdot \underline{\varphi} \in \text{Im} \left( \underline{h} \right)$ . From  $\frac{2}{3}\underline{i} : \underline{i} = \underline{\delta}$  it is deduced that  $\underline{\varphi} = \frac{2}{3}\underline{i} : \underline{\Phi}$ . Reissner-Mindlin rotations have thus the following form:

$$\varphi_1 = \frac{2}{3}\Phi_{111} + \frac{1}{3}\Phi_{122} \quad \varphi_2 = \frac{2}{3}\Phi_{222} + \frac{1}{3}\Phi_{121}$$

Considering the generalized shear strain energy in the Bending-Gradient model

### 3.2. LINEAR BUCKLING OF PLATES WITH THE BENDING-GRADIENT THEORY

(Lebée and Sab, 2015b):

$$\begin{aligned} W^{\text{BG},\Gamma}(\Gamma) &= \frac{1}{2} \left( \underline{\Phi} + \underline{\mathbf{i}} \cdot \underline{\nabla} U_3 \right) : \underline{\mathbf{H}} : \left( \underline{\Phi} + \underline{\mathbf{i}} \cdot \underline{\nabla} U_3 \right) \\ &= \frac{1}{2} \left( \underline{\varphi} + \underline{\nabla} U_3 \right) \cdot \left[ \underline{\mathbf{i}} : \underline{\mathbf{H}} : \underline{\mathbf{i}} \right] \cdot \left( \underline{\varphi} + \underline{\nabla} U_3 \right) \end{aligned}$$

the Reissner-Mindlin shear strain energy is obtained with the following projection of the sixth-order generalized shear stress tensor  $\underline{\mathbf{H}}$ :

$$\begin{aligned} \underline{\mathbf{F}}^{\text{ss}} &= \underline{\mathbf{i}} : \underline{\mathbf{H}} : \underline{\mathbf{i}} \\ \begin{cases} F_{11}^{\text{ss}} &= H_{111111} + H_{122221} + 2H_{111221} \\ F_{12}^{\text{ss}} &= F_{21}^{\text{ss}} = H_{111121} + H_{111222} + H_{121221} + H_{222221} \\ F_{12}^{\text{ss}} &= H_{222222} + H_{121121} + 2H_{121222} \end{cases} \end{aligned} \quad (3.11)$$

The relevance of these two projections will be tested in section 3.4.

#### 3.2.2.4 Simple support boundary conditions

On the plate boundaries  $\partial\omega$ , the normal and the tangent vectors are noted  $\underline{\mathbf{n}}$  and  $\underline{\mathbf{t}}$  respectively. In the Reissner-Mindlin plate model, there are two kinds of simple support conditions: soft or hard simple support (SSS and HSS respectively). The soft-simple-support condition is modelled by restraining only the out-of-plane displacement  $U_3$  and letting the tangent rotation  $\varphi_t$  free. The latter is restrained on a hard simply supported edge  $\partial\omega$ :

$$\text{SSS} \begin{cases} U_3 = 0 \\ \underline{\mathbf{M}} \cdot \underline{\mathbf{n}} = \underline{\mathbf{0}} \end{cases} \quad \text{HSS} \begin{cases} U_3 = 0 \\ \underline{\mathbf{n}} \cdot \underline{\mathbf{M}} \cdot \underline{\mathbf{n}} = 0 \\ \varphi_t = 0 \end{cases} \quad (3.12)$$

In the Bending-Gradient model, general boundary conditions consist in setting:

$$\begin{cases} \underline{\mathbf{M}} = \underline{\mathbf{M}}^d & \text{or } \underline{\Phi} \cdot \underline{\mathbf{n}} = \underline{\mathbf{H}}^d \text{ on } \partial\omega & (3.13a) \\ \left( \underline{\mathbf{i}} : \underline{\mathbf{R}} \right) \cdot \underline{\mathbf{n}} = V_3^d & \text{or } U_3 = U_3^d \text{ on } \partial\omega & (3.13b) \end{cases}$$

Since  $\underline{\mathbf{Q}} = \underline{\mathbf{i}} : \underline{\mathbf{R}}$ , the out-of-plane boundary condition (3.13b) is the same as in the Reissner-Mindlin model. However, the boundary condition (3.13a) differs since the bending moment  $M_{tt}$  may be imposed in the Bending-Gradient theory adding one boundary condition compared to the Reissner-Mindlin model.

As in the Reissner-Mindlin model, the soft simple support boundary condition is modeled by restraining the out-of-plane displacement  $U_3$  and letting the other kinematic

fields free:

$$U_3 = 0 \text{ and } M_{nn} = M_{nt} = M_{tt} = 0 \quad (3.14)$$

Contrary to the Reissner-Mindlin model, the bending moment  $M_{tt}$  is set to zero. Since  $M_{tt} = \int_{-\frac{h}{2}}^{\frac{h}{2}} x_3 \sigma_{tt} dx_3$  (see Equation 3.1a), it seems to involve a 3D stress component to which no 3D boundary condition should be applied. Actually it does since for an heterogeneous plate  $\sigma_{\alpha\beta}$  is a linear combination of all bending moment components  $M_{\alpha\beta}$  (Lebée and Sab, 2011a). The condition  $M_{tt} = 0$  is thus related to the boundary layer ensuring  $\underline{\sigma} \cdot \underline{n} = 0$ . It is here remarked that in the case of a homogeneous plate  $\sigma_{\alpha\beta} = \frac{12x_3}{h^3} M_{\alpha\beta}$  imposes on soft simple supported edges only  $M_{nn} = M_{nt} = 0$  as in the Reissner-Mindlin model.

The hard simple support boundary condition (3.12) cannot be directly transposed from the Reissner-Mindlin model to the Bending-Gradient model since generalized rotations  $\Phi_{\alpha\beta\gamma}$  are a combination of both rotations  $\varphi_\alpha$ . Nevertheless, it can be demonstrated that if the constitutive material is orthotropic with respect to  $(\underline{n}, \underline{t})$ ,  $\Phi_{ntn}$  is working with  $M_{nt}$  and is then the only component of  $\underline{\Phi}$  directly related to the tangent displacement  $u_t$  and then to the tangent rotation  $\varphi_t$ . Since rectangular CLT panels comply with this assumption (boards are oriented in  $x_1$  or  $x_2$ -direction depending on the layer), the hard simple support boundary is defined by:

$$U_3 = 0, \Phi_{ntn} = 0 \text{ and } M_{nn} = M_{tt} = 0 \quad (3.15)$$

Similarly to the Reissner-Mindlin model, in the present extension of the Bending-Gradient theory to plate buckling, closed-form solutions for  $\underline{\Phi}$  could only be derived in the case of hard simple support. From a practical point of view, it is difficult to know whether hard or soft simple support are applied. For this reason, both hypothesis will be investigated numerically in section 3.3.2.1.

### 3.2.3 Linear buckling analysis with the Bending-Gradient theory

We consider now a linear elastic rectangular plate of length  $a$ , width  $b$  and thickness  $h$ , which mid-plane is the 2D domain  $\omega = ([0, a], [0, b])$ . We assume that the plate is uniformly pre-loaded with the membrane stress  $\underline{N}^0(\lambda) = -\lambda \underline{e}_1 \otimes \underline{e}_1$  (see Figure 3.2).

The membrane stress is defined as  $N_{\alpha\beta} = \int_{-\frac{h}{2}}^{\frac{h}{2}} \sigma_{\alpha\beta} dx_3$ .

#### 3.2.3.1 The linearized 3D stress state under in-plane compression

The initial stress corresponding to the pre-load  $\underline{N}^0(\lambda)$  is noted  $\underline{\sigma}^0$  and complies with the equality:  $\int_{-\frac{h}{2}}^{\frac{h}{2}} \sigma_{\alpha\beta}^0 dx_3 = N_{\alpha\beta}^0$ . We consider now the perturbed state  $\underline{u} = \underline{u}_0 + \underline{\xi}$

### 3.2. LINEAR BUCKLING OF PLATES WITH THE BENDING-GRADIENT THEORY

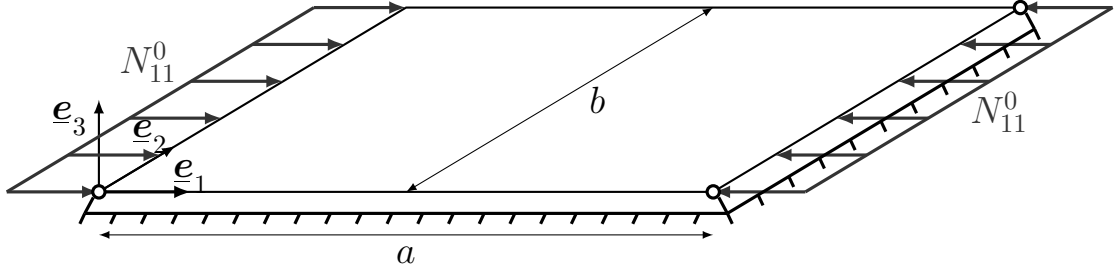


Figure 3.2 – Settings of the buckling problem of a simply supported plate under unilateral load

where  $\underline{u}_0$  is the initial displacement field and  $\underline{\xi}$  a small perturbation which comply with kinematic boundary conditions. The Piola-Lagrange stress tensor  $\underline{\sigma}$ , also called the first Piola-Kirchhoff stress tensor, is expressed at first order as:

$$\sigma_{ij} = \sigma_{ij}^0 + \xi_{i,k} \sigma_{kj}^0 + C_{ijkl} \frac{1}{2} (\xi_{k,l} + \xi_{l,k}) \quad (3.16)$$

In the following, we assume that the third term in Equation (3.16) takes the same form as the Bending-Gradient stress tensor:  $\underline{\sigma}^{\text{BG}} = \underline{\mathbb{C}} : (\underline{\xi} \otimes^s \underline{\nabla})$  and depends then on  $\underline{M}$  and  $\underline{R}$  (Lebée and Sab, 2011a).

Since  $\underline{\sigma}^0$  is already in equilibrium ( $\sigma_{ij,j}^0 = 0$ ), the 3D equilibrium  $\sigma_{ij,j} = 0$  is given only by the divergence of the second and the third term in equation (3.16):

$$(\xi_{i,k} \sigma_{kj}^0)_{,j} + \sigma_{ij,j}^{\text{BG}} = \xi_{i,kj} \sigma_{kj}^0 + \sigma_{ij,j}^{\text{BG}} = 0 \quad (3.17)$$

It can be demonstrated through asymptotic expansions (Ciarlet and Destuynder, 1979; Lebée and Sab, 2013) that the 3D displacement field of a plate has only an out-of-plate component depending on in-plane directions at the leading order:  $\underline{\xi} = U_3(x_1, x_2) \cdot \underline{e}_3$ . The Equation (3.17) may then be rewritten by separating in-plane and out-of-plane parts of the equilibrium:

$$\begin{cases} \sigma_{\alpha\beta,\beta}^{\text{BG}} + \sigma_{\alpha 3,3}^{\text{BG}} = 0 & (3.18a) \end{cases}$$

$$\begin{cases} \sigma_{\alpha\beta}^0 U_{3,\alpha\beta} + \sigma_{3\gamma,\gamma}^{\text{BG}} + \sigma_{33,3}^{\text{BG}} = 0 & (3.18b) \end{cases}$$

The integration of  $x_3 \times (3.18a)$  through the thickness, after integration by part, is found to be equivalent to the plate equilibrium  $M_{\alpha\beta,\beta} - i_{\alpha\gamma\delta\eta} R_{\eta\delta\gamma} = M_{\alpha\beta,\beta} - R_{\alpha\beta\beta} = 0$ . In absence of out-of-plane  $p_3$ , the integration through the thickness of Equation (3.18b)

leads to the following equality:

$$\nabla \cdot \left( \underset{\approx}{\mathbf{i}} : \underset{\approx}{\mathbf{R}} \right) + U_{3,\alpha\beta} N_{\alpha\beta}^0 = 0 \quad (3.19)$$

It may be noted here that the second term of the equilibrium (3.19) due to second-order effects of in-plane load  $\mathcal{N}^0$  and to out-of-plane deflection  $U_3$  takes the same form in the Bending-Gradient theory as in Kirchhoff-Love (Timoshenko and Gere, 1961) and Reissner-Mindlin models.

### 3.2.3.2 Buckling load calculation

The substitution of the set of equilibrium (Eq. 3.3, 3.19), compatibility (Eq. 3.4) and constitutive equations (Eq. 3.5) results in an eigenvalue problem which solutions are the critical buckling modes  $\lambda$  associated with the corresponding eigenmodes  $(U_3, \mathbf{\Phi})$ :

$$\left\{ \begin{array}{l} \left[ \underset{\approx}{\mathbf{i}} : \left[ \left( \underset{\approx}{\mathbf{D}} : \left( \mathbf{\Phi} \cdot \nabla \right) \right) \otimes \nabla \right] \right] \cdot \nabla - \lambda U_{3,11} = 0 \\ \mathbf{\Phi} + \underset{\approx}{\mathbf{i}} \cdot \nabla U_3 = \underset{\approx}{\mathbf{h}} : \left[ \left( \underset{\approx}{\mathbf{D}} : \left( \mathbf{\Phi} \cdot \nabla \right) \right) \otimes \nabla \right] \end{array} \right. \quad (3.20a)$$

$$\left\{ \begin{array}{l} \left[ \underset{\approx}{\mathbf{i}} : \left[ \left( \underset{\approx}{\mathbf{D}} : \left( \mathbf{\Phi} \cdot \nabla \right) \right) \otimes \nabla \right] \right] \cdot \nabla - \lambda U_{3,11} = 0 \\ \mathbf{\Phi} + \underset{\approx}{\mathbf{i}} \cdot \nabla U_3 = \underset{\approx}{\mathbf{h}} : \left[ \left( \underset{\approx}{\mathbf{D}} : \left( \mathbf{\Phi} \cdot \nabla \right) \right) \otimes \nabla \right] \end{array} \right. \quad (3.20b)$$

Closed form solution of this problem are derived looking for expressions of  $U_3$  and  $\mathbf{\Phi}$  in the form of double-Fourier series. Considering kinematic compatibility (Eq. 3.4), hard simple support boundary conditions (Eq. 3.15) and the geometry of the plate (which is rectangular with each layer's principal axes coinciding with the rectangular reference frame  $(\mathbf{e}_1, \mathbf{e}_2, \mathbf{e}_3)$ ), expressions of  $U_3$  and  $\mathbf{\Phi}$  are looked in the following form:

$$U_3 = \sum_{m=1}^{\infty} \sum_{n=1}^{\infty} U_3^{mn} \sin(K_m x_1) \sin(K_n x_2)$$

$$\text{for } \Phi_{111}, \Phi_{221} \text{ and } \Phi_{122} :$$

$$\Phi_{\alpha\beta\gamma} = \sum_{m=1}^{\infty} \sum_{n=1}^{\infty} \Phi_{\alpha\beta\gamma}^{mn} \cos(K_m x_1) \sin(K_n x_2) \quad (3.21)$$

$$\text{for } \Phi_{121}, \Phi_{112} \text{ and } \Phi_{222} :$$

$$\Phi_{\alpha\beta\gamma} = \sum_{m=1}^{\infty} \sum_{n=1}^{\infty} \Phi_{\alpha\beta\gamma}^{mn} \sin(K_m x_1) \cos(K_n x_2)$$

$$\text{where } K_m = \frac{m\pi}{a} \text{ and } K_n = \frac{n\pi}{b} \text{ for } \{m, n\} \in \mathbb{N}^{*2}$$

$U_3^{mn}$  and  $\Phi_{\alpha\beta\gamma}^{mn}$  are the amplitudes of each term of the out-of-plane displacement and the generalized rotations associated with the  $\{m, n\}$  mode respectively. With such a form, solutions of the problem (3.20) may be found using Voigt notations (see A.2). For a given mode, the critical buckling load  $\lambda_{mn}$  is derived from the Equation (A.16).

It is noticed here that the eigenvalue solution for a Reissner-Mindlin model may

### 3.3. 3D REFERENCE MODEL FOR THE LINEAR BUCKLING OF CLT PANELS

be obtained by replacing  $\underline{\underline{h}}$  by  $\underline{\underline{i}}^T \cdot \underline{\underline{f}} \cdot \underline{\underline{i}}$  (Eq. 3.9) where  $\underline{\underline{f}}$  is the second-order shear compliance tensor of a Reissner-Mindlin model. In this study and in the following comparisons,  $\underline{\underline{f}}$  takes successively the forms  $\underline{\underline{f}}^R$ ,  $\underline{\underline{f}}^{sc}$  and  $\underline{\underline{f}}^{ss} = \left(\underline{\underline{F}}^{ss}\right)^{-1}$  to comply with the FOSDT corrected by  $\kappa$ , the shear compliance and the shear stiffness projections respectively.

It is noted here that the critical load calculated with the Kirchhoff-Love model by Timoshenko and Gere (1961) may be deduced from the Equation (A.16) by neglecting shear effects  $\underline{\underline{h}} = \underline{\underline{0}}$ :

$$\lambda_{mn}^K = \frac{\pi^2}{b^2} \left( \frac{m^2}{\alpha^2} D_{1111} + \frac{n^4}{m^2} \alpha^2 D_{2222} + 2n^2 (D_{1122} + 2D_{1212}) \right) \quad (3.22)$$

where  $\alpha = \frac{a}{b}$  is the plate aspect ratio. From this expression, the minimal buckling load for a varying  $\alpha$  may be deduced as:

$$\lambda_{min}^K = \frac{2\pi^2 n^2}{b^2} \left( \sqrt{D_{1111} D_{2222}} + D_{1122} + 2D_{1212} \right) \quad (3.23)$$

$$\text{for } \alpha = \frac{m}{n} \sqrt[4]{\frac{D_{1111}}{D_{2222}}}$$

## 3.3 3D reference model for the linear buckling of CLT panels

A 3D numerical study is performed using the finite element software ABAQUS. These numerical results will be considered as the reference results for the comparison with analytical models in section 3.4.

### 3.3.1 The 3D linear buckling problem

The linear buckling analysis is performed in two steps: the plate is initially pre-stressed with the uniform membrane stress  $\underline{\underline{N}}^0(\lambda) = -\lambda \underline{\underline{e}}_1 \otimes \underline{\underline{e}}_1$  and then buckling modes satisfying boundary conditions are calculated as linear perturbations of the reference state.

#### 3.3.1.1 The pre-stressed state

For the design of walls, it is conventionally assumed that the 3D pre-stress field is equivalent to a uniform membrane stress  $N_{11}$ . For homogeneous plates such as steel plates, the 3D pre-stress is uniform in the whole plate and is then  $\sigma_{11} = N_{11}/h$ .

Nonetheless, for a laminated plate, the pre-stress equivalent to a uniform membrane stress is not uniform but depends on the out-of-plane coordinate:  $\sigma_{11} = \sigma_{11}(x_3)$ . Thus, boundary conditions of the actual 3D problem (see Figure 3.3) are given by the following equality up to a rigid motion:

$$\begin{cases} \underline{\boldsymbol{\sigma}} \cdot \underline{\mathbf{n}} = \mathbf{0} & \text{for } x_2 = \{0, b\} \\ \underline{\boldsymbol{\sigma}} \cdot \underline{\mathbf{n}} = \begin{pmatrix} \sigma_{11}(x_3) \\ 0 \\ 0 \end{pmatrix} & \text{for } x_1 = \{0, a\} \end{cases} \quad (3.24)$$

where

$$\int_{-\frac{h}{2}}^{\frac{h}{2}} \sigma_{11}(x_3) dx_3 = N_{11}$$

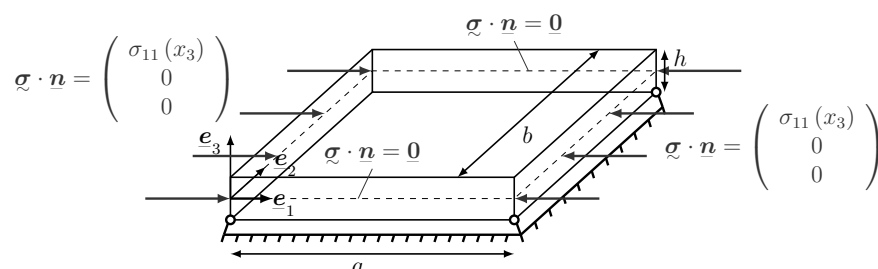


Figure 3.3 – 3D Boundary conditions of the buckling mode calculation step

Nonetheless, applying directly this stress distribution is not convenient in Abaqus. An alternative approach consists thus in imposing the corresponding strain field. Indeed, from the classical lamination theory, the 3D in-plane strain field  $\underline{\boldsymbol{\varepsilon}}$  may be expressed as a function of the membrane stress:

$$\varepsilon_{\alpha\beta} = E_{\alpha\beta} = a_{\alpha\beta\gamma\delta} N_{\gamma\delta}^0 \Leftrightarrow \underline{\boldsymbol{\varepsilon}} = \underline{\boldsymbol{E}} = \underline{\boldsymbol{a}} : \underline{\boldsymbol{N}}^0 \quad (3.25)$$

$$\text{with } \underline{\boldsymbol{a}}^{-1} = \underline{\boldsymbol{A}} = \int_{-\frac{h}{2}}^{\frac{h}{2}} \underline{\boldsymbol{C}}^\sigma dx_3$$

where  $\underline{\boldsymbol{E}}$  is the membrane strain tensor and  $\underline{\boldsymbol{A}}$  the fourth-order membrane stiffness tensor. From the orthotropy of CLT plates, it is possible to derive the strain distribution  $E_{11}$  and  $E_{22}$  corresponding to the pre-stressed state. Thus, kinematic boundary conditions are applied on the CLT plate to model a uniform membrane stress as shown in Figure 3.4. The pre-strain field is then uniformly distributed in the whole plate with a compression in  $x_1$ -direction and a dilatation in  $x_2$ -direction modeling in-plane Poisson's effect and vanishing  $N_{12}^0$  and  $N_{22}^0$ .

### 3.3. 3D REFERENCE MODEL FOR THE LINEAR BUCKLING OF CLT PANELS

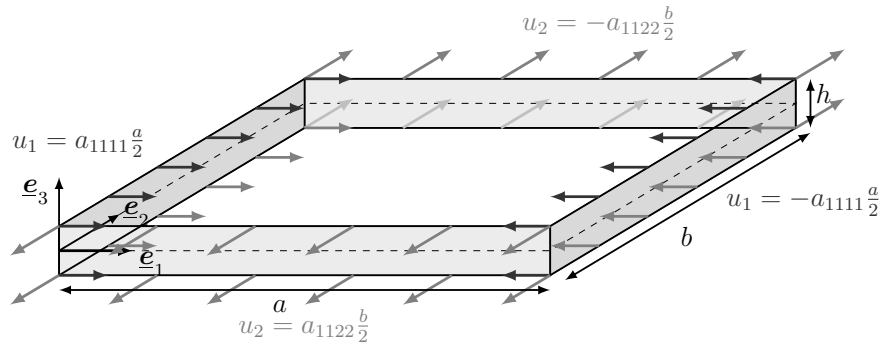


Figure 3.4 – Model of the uniform membrane pre-stress during the stress perturbation step in Abaqus calculation

#### 3.3.1.2 Buckling modes calculation

During the second step, the buckling modes are calculated as additional perturbed states which comply with boundary conditions. Thus, 3D simple support boundary conditions must be modeled in this step.

Hard and soft simple support boundary conditions (see section 3.2.2.4) are applied only on the 2D plate models. In the 3D problem, there is no rotation field  $\varphi$  but only three translational degrees of freedom and thus HSS and SSS conditions cannot be directly applied to the 3D model. Nevertheless we may assume that restraining the tangent displacement  $u_t$  is a good 3D model to set tangent rotation  $\varphi_t$  to zero. These equivalent 3D hard and soft simple support boundary conditions are shown in Figure 3.5 for a rectangular plate.

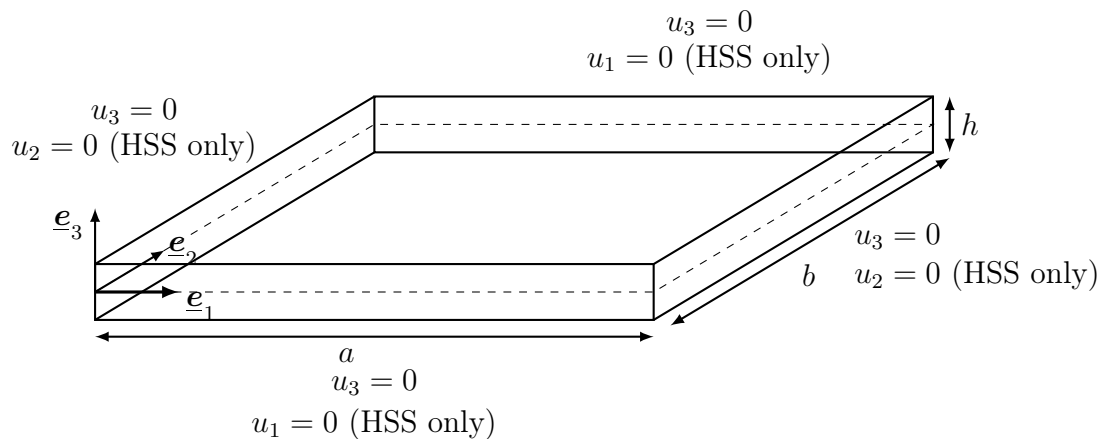


Figure 3.5 – 3D Boundary conditions of the buckling mode calculation step

The C3D20R element, a quadratic 3D brick-element with 20 nodes is used to mesh

the plate. There are three degrees of freedom at each node, one for each translation. A reduced integration with only 8 integration points is chosen to evaluate the material response in each element (ABAQUS, 2004). A convergence study was performed to find the most suitable mesh with an accuracy of 0.1% in terms of buckling load. In order to reduce the time of calculation, elements are stretched in in-plane directions (see Figure 3.8).

### 3.3.1.3 Timber elastic characteristics and CLT configurations

Timber is a material with a high anisotropy and is often modeled as a linear orthotropic material. Norway Spruce mechanical characteristics are used in this chapter because it is one of the most used species in timber construction. Reference values are taken from Keunecke et al. (2008) (see Table 3.1). For an orthotropic material,  $E_i$ ,  $G_{ij}$  and  $\nu_{ij}$  stand for Young and shear moduli and Poisson's ratios respectively.  $L$ ,  $R$  and  $T$  stand for longitudinal, radial and tangential directions respectively.

$E_L$	$E_R$	$E_T$	$G_{LR}$	$G_{LT}$	$G_{RT}$	$\nu_{LR}$	$\nu_{LT}$	$\nu_{RT}$
<b>12800</b>	625	397	617	587	<b>53</b>	0.36	0.45	0.41

Table 3.1 – *Elastic Properties of Norway Spruce, E and G in MPa (Keunecke et al., 2008)*

There is a high contrast between the longitudinal stiffness  $E_L$  and the rolling shear stiffness  $G_{RT}$ . These two characteristics will thus drive the buckling load of CLT panels and are of main importance. In the present model,  $R$  is oriented in the out-of-plane direction  $\underline{e}_3$  and  $L$  ( $T$  respectively) is alternatively oriented in  $\underline{e}_1$  ( $\underline{e}_2$  respectively) and in  $\underline{e}_2$  ( $\underline{e}_1$  respectively) directions depending on layers<sup>1</sup>. In the upper and lower layers, fibers ( $L$ ) are always oriented in  $x_1$ -direction.

Standard CLT panels are generally made of 3,5 or 7 plies which have the same thickness in the present study, and comply with the mirror symmetry. In the following, the slenderness  $\frac{b}{h}$  varies between 10 and 35 and the plate aspect  $\frac{a}{b}$  varies between 0.5 and 4 to include geometries of actual structures.

---

1. Since, this chapter was chronologically the first chapter studied during this thesis, there is here no distinction between the global equivalent layer stiffness in the coordinate system  $(O, L, C, Z)$  and the local stiffness in the coordinate system  $(O, L, R, T)$ . Nonetheless, conclusions of the numerical application in this chapter would be similar using the equivalent-layer stiffness derived in Part I.

### 3.3.2 Application of the 3D linear buckling to CLT panels

#### 3.3.2.1 Global behavior of the plate

**3.3.2.1.1 The boundary layer** On Fig. 3.6, the distribution of in-plane stress  $\sigma_{12}$  of the first buckling mode is drawn for an out-of-plane displacement magnitude normalized to 1. It is noted here that the global shape of the buckling mode is similar for hard and soft simple support boundary conditions and comply with the double-sinus form suggested in section 3.2.3.

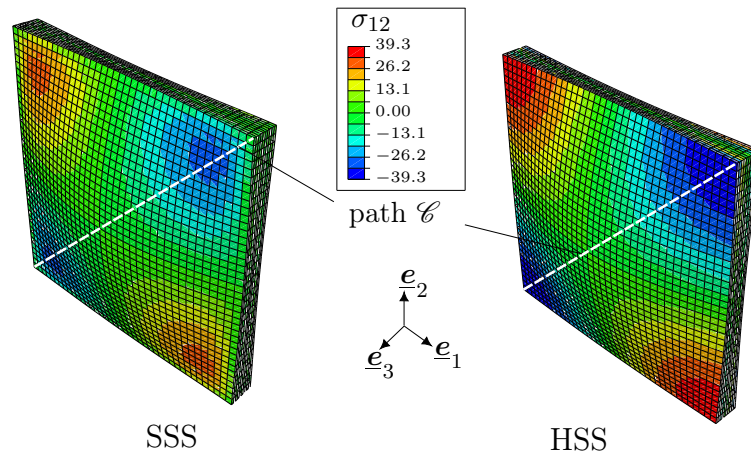


Figure 3.6 – 3D distribution of  $\sigma_{12}$  for a 5-ply CLT square panels with  $\frac{b}{h} = 15$  on SSS or HSS edges

The main difference between SSS and HSS is that  $\sigma_{12}$  is zero at boundaries only in the first case. It is the direct consequence of the free tangent displacement  $u_t$  for SSS plates and it is equivalent to impose  $M_{12} = 0$  at boundaries on a plate model.

On Figure 3.7, the ratio between the in-plane shear stress  $\sigma_{12}$  for SSS and HSS plates is plotted along the path  $\mathcal{C}$  which curvi-linear abscissa is  $x_c$  and total length is  $L$ . Thus, far enough from boundaries, the distribution of  $\sigma_{12}$  is similar for hard and soft simple support boundary conditions: it is a consequence of the Saint-Venant principle. Thus, there is a boundary layer next to soft simply supported edges. The length of this boundary layer in the studied case is equal to more than twice the thickness of the CLT panel. Contrary to the case of thin plates, this transition area is not negligible in the case of CLT panels which are relatively thick and anisotropic. Thus, the question of the distinction between soft and hard simple supported plates is meaningful and needs to be developed.

On Figure 3.8, the displacement  $u_1$  is plotted on the loaded edge for a 5-ply CLT panel with HSS boundary conditions. The displacement  $u_1$  is not linear through the thickness, and thus the shear strain  $\varepsilon_{13}$  is not uniform along  $x_3$  because of the high

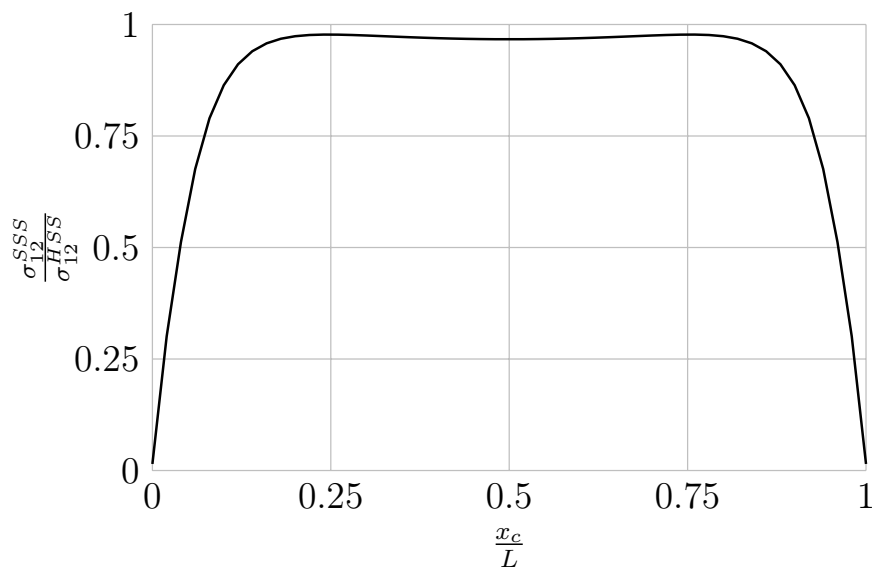


Figure 3.7 – Ratio between the in-plane shear stress  $\sigma_{12}$  of SSS and HSS 5-ply CLT square panels with  $\frac{b}{h} = 15$  along the path  $\mathcal{C}$  (Figure 3.6)

stiffness contrast between longitudinal and tangential layers. The assumption of linear in-plane displacements in Hencky’s kinematic removes warping effects observed in laminated plates. On the contrary, in the Bending-Gradient theory, the four additional variables in  $\Phi$  capture these effects. The Bending-Gradient may thus describe qualitatively better the behavior of CLT panels by introducing four additional unknowns.

The buckling load relative difference between 3D HSS and SSS with respect to HSS plates is plotted on Figure 3.9 for a 5-ply Cross-Laminated-Plate. As expected, the buckling load of SSS panels is lower than in HSS panels since restraining the tangent displacement at boundaries stiffens the plate. This stiffening effect is more important when decreasing the slenderness  $\frac{b}{h}$  for all aspect ratios  $\frac{a}{b}$ . This result comes directly from the fact that hard and soft simple support conditions become closer when increasing the slenderness and converges to HSS which is the only simple support boundary condition in classical plate theory.

Thus, as it was expected, the relative difference between hard and soft simple support boundary, which is around 3% with a maximum of 5% in the studied domain, can be meaningful depending on the required precision.

### 3.3.2.2 Buckling load and compressive strength of HSS CLT panels

In this section, the 3D critical buckling stress  $\sigma_{cr}$  is compared to the compressive strength  $\sigma_u$  of CLT panels. From the paper of Cabrero et al. (2012), the average strength of timber in compression in L-direction is 41.7MPa. For a 5-ply CLT, we may assume

### 3.3. 3D REFERENCE MODEL FOR THE LINEAR BUCKLING OF CLT PANELS

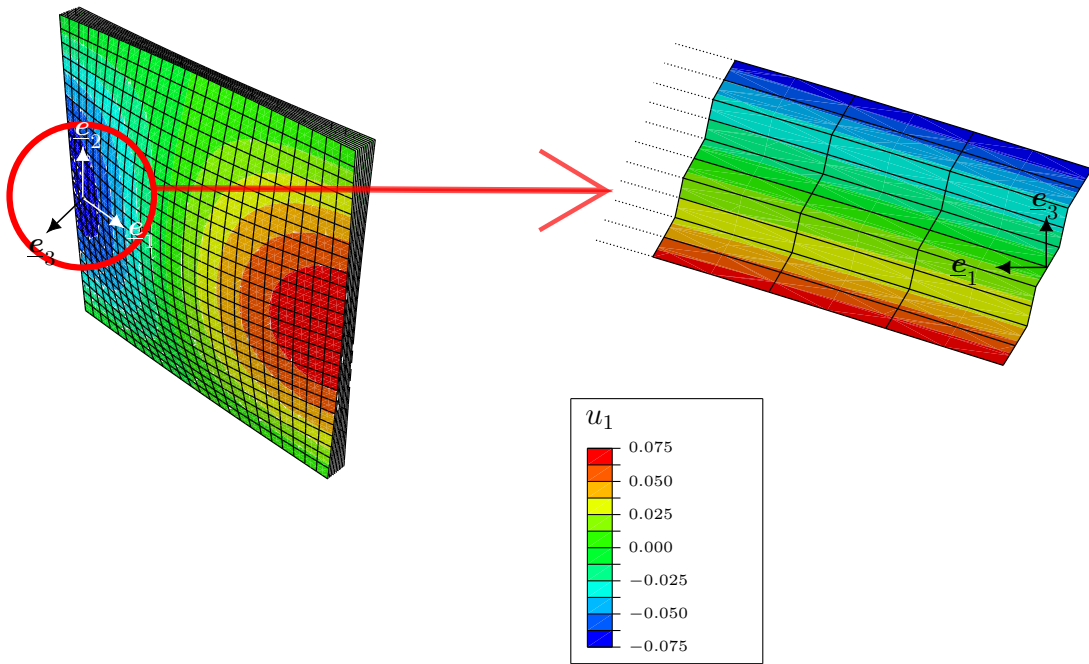


Figure 3.8 – Displacement  $u_1$  according to thickness for an HSS 5-ply CLT square panel with  $\frac{b}{h} = 15$

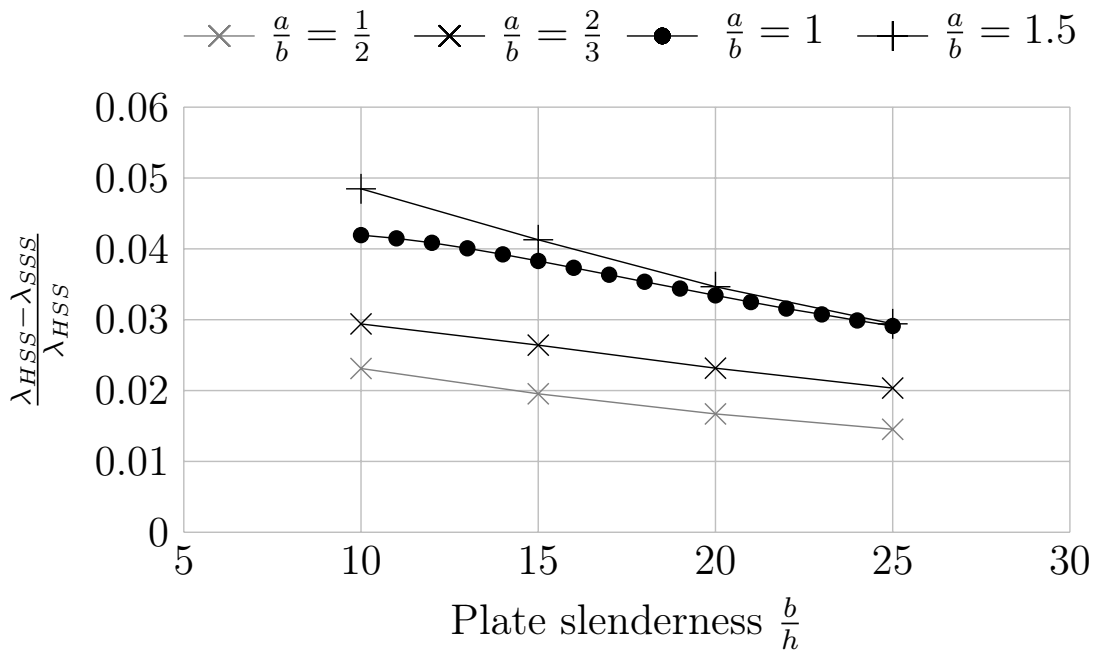


Figure 3.9 – Relative difference between HSS and SSS with varying slenderness  $\frac{b}{h}$  and plate aspect ratio  $\frac{a}{b}$

CHAPTER 3. THE BENDING-GRADIENT THEORY FOR THE LINEAR BUCKLING OF THICK PLATES: APPLICATION TO CROSS-LAMINATED-TIMBER PANELS

that the in-plane compression stress is only distributed in the three longitudinal plies. Thus the compressive strength of a 5-ply CLT panel may be set as  $41.7 \times \frac{3}{5} \approx 25\text{MPa}$  and does not vary with  $\frac{b}{h}$  and  $\frac{a}{b}$  contrary to the buckling load. The same procedure can be applied to 3-ply and 7-ply CLT panels (see Table 3.2).

	3-ply	5-ply	7-ply
$\sigma_u$ (MPa)	27.8	25	23.8

Table 3.2 – Compressive strength of CLT with several configurations

On Figure 3.10, the ratio between the 3D reference buckling load and the compressive strength is plotted according to the slenderness  $\frac{b}{h}$  for square hard-simply-supported 3, 5, and 7-ply CLT square panels. For each configuration, the slenderness domain is chosen considering practical design limits. Indeed, since plies are limited to 51 millimeters (Stürzenbecher et al., 2012), thick walls are designed using more layers than thin walls. On this figure, two domains may be identified: the domain above 1 where material failure occurs before buckling; the domain below 1 where instabilities occur before failure.

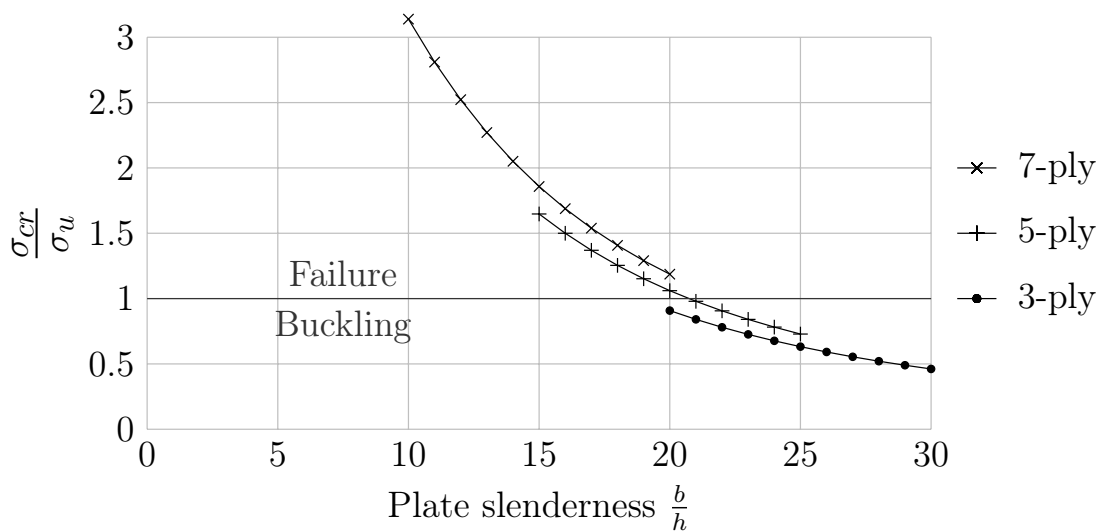


Figure 3.10 – Ratio between reference 3D buckling load and compressive strength for a HSS square CLT panel

One can remark that the buckling load and the compressive strength of CLT panels are of the same order of magnitude. For a slenderness of  $\frac{b}{h} \geq 21$ , the buckling load is lower than the compressive strength for 3- and 5-ply CLT panels. On the contrary, in the studied domain, the buckling load of 7-ply CLT panels is never lower than the

compressive strength. This results show nonetheless the necessity to take into account instabilities issues for the design of all CLT structures because of geometric imperfections which may affect more buckling phenomenons than material strength.

Moreover, for a given slenderness, the ratio between the buckling load and the compressive strength is increasing with the number of plies. Indeed, the more plies there are in the CLT panel, the lower is its compressive strength since there is a lower proportion of stiff layers in the cross section. However, buckling loads depend also on the location of plies because of shear effects (see 3.4.1). It is hence observed from the Figure 3.10 that the buckling load varies less than the material failure between different configurations, therefore the ratio between buckling load and compressive strength of 7-ply panel is higher than 3-ply and 5-ply.

## 3.4 Comparison between numerical results and plate models

In the following, the application of the Bending-Gradient (BG) to linear plate buckling is compared to the classical lamination theory (CPT) and to several Reissner-Mindlin models. For the latter, the well-known first-order shear deformation theory (FOSDT) with the shear correction factor  $\kappa = \frac{5}{6}$  is considered as well as the two projections on Reissner-Mindlin models suggested in Section 3.2.2.3: the shear stiffness projection (SSP) and the shear compliance projection (SCP). The previous 3D numerical calculations by finite element are used as references to compare the accuracy of each theory.

### 3.4.1 CLT panel stiffness for practical configurations

Various CLT configurations can be found on the market. The main configurations are 3,5,7-ply. To investigate a realistic range of panels, the three kinds of configurations are studied. The bending stiffness  $\tilde{D}$  as well as the shear stiffness of the FOSDT  $\tilde{F}^R$  with the correction factor  $\kappa = \frac{5}{6}$ , the shear compliance projection  $\tilde{F}^{sc}$  and the shear stiffness projection  $\tilde{F}^{ss}$  are calculated for 3-, 5-, and 7-ply CLT square panels with a thickness  $h = 0.15\text{m}$ . All values are gathered in Table 3.3.

First, it is observed that the more layers there are in the CLT panels, the lower is  $D_{1111}$  and the higher is  $D_{2222}$ . The main reason is that the proportion between stiff layers and flexible layers balances when increasing the number of layers which explains also the high contrast between  $D_{1111}$  and  $D_{2222}$  particularly in 3-ply. Nevertheless, these variations have little influence on the buckling load. Indeed, the bending stiffness is mostly driven by an average stiffness which can be evaluated in first approximation by the buckling load from the classical lamination theory (see Equation 3.22). This

CHAPTER 3. THE BENDING-GRADIENT THEORY FOR THE LINEAR BUCKLING OF THICK PLATES: APPLICATION TO CROSS-LAMINATED-TIMBER PANELS

	$D_{1111}^*$	$D_{2222}^*$	$D_{1122}^*$	$D_{1212}^*$	$F_{11}^R$	$F_{22}^R$	$F_{11}^{cs**}$	$F_{22}^{cs**}$	$F_{11}^{ss**}$	$F_{22}^{ss**}$
3-ply	3493	242	51	115	53.6	30.1	11.3	24.1	21.8	31.2
5-ply	2893	843	51	115	48.9	34.8	12.3	9.3	13.0	13.6
7-ply	2610	1126	51	115	46.9	36.8	12.5	10.3	13.2	13.7

\* From Equation (3.6)

\*\* From Equations (3.7), (3.10) and (3.11)

Table 3.3 – Bending stiffness ( $kN.m$ ) and shear compliance ( $MN.m^{-1}$ ) for a square CLT plate with a thickness  $h = 0.15m$

value will be the same for the three configurations presented here: the main difference between the buckling load of these configurations will thus be mostly due to the shear compliance.

Furthermore, three models of shear behavior are presented here.  $\tilde{\mathbf{F}}^R$  is the average shear stiffness tensor  $C_{\alpha\beta\beta\alpha}$  through the thickness corrected by  $\kappa = \frac{5}{6}$  which explains its variations in the studied configurations since it is driven by the proportion of stiff layers in the appropriate direction.  $\tilde{\mathbf{F}}^{sc}$  and  $\tilde{\mathbf{F}}^{ss}$  are given by the simplification of the generalized shear compliance tensor  $\underline{\tilde{h}}$  and the generalized shear stiffness tensor  $\underline{\tilde{H}}$  respectively. In the Bending-Gradient theory, the relative position of layers in the cross section are considered (see Equations 3.7) which explains why the shear stiffness  $F_{\alpha\beta}$  from the Bending-Gradient projections are generally lower than the ones from the FOSDT. Indeed, shear effects are more important in the central layers which explains also the variations of  $\tilde{\mathbf{F}}^{sc}$  and  $\tilde{\mathbf{F}}^{ss}$  for the studied ply configurations.

### 3.4.2 Influence of slenderness $\frac{b}{h}$

Figure 3.11 shows the ratio between the first buckling load and the compressive strength of a HSS 5-ply square CLT panel plotted as function of the slenderness  $\frac{b}{h}$ . On Figure 3.12, the relative error of closed-form results normalized with respect to the 3D reference results for the same configurations as in Figure 3.11. On Figure 3.13 and Figure 3.14, the same results as Figure 3.11 and Figure 3.12 are plotted for HSS 3-ply square CLT panel for the corresponding slenderness range.

As expected, from Figures 3.12 and 3.14, the classical lamination theory (CPT) gives results far from the actual ones. Indeed, the error is always larger than 10% in the studied domain and is even higher than 30% for thick configurations. The FOSDT, by considering shear effects, is closer than the classical lamination model although the error is still large. In the studied domain, the Bending-Gradient theory (BG) is clearly the model which best fits the buckling load of plates. For slenderness  $\frac{b}{h} > 10$ , the error is lower than 3.5%, and for  $\frac{b}{h} > 16$  the order of magnitude of the error is less than 1.0%.

It is here noticed that the shear stiffness projection (SSP) of the Bending-Gradient

### 3.4. COMPARISON BETWEEN NUMERICAL RESULTS AND PLATE MODELS

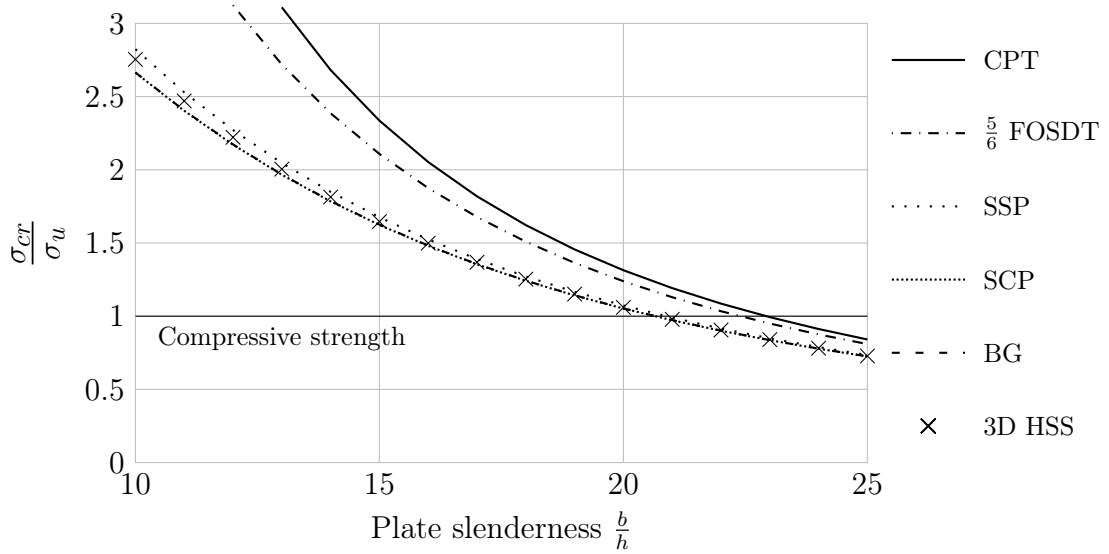


Figure 3.11 – Ratio between buckling load and compressive strength according to slenderness  $\frac{b}{h}$  for a HSS 5ply-CLT square panel

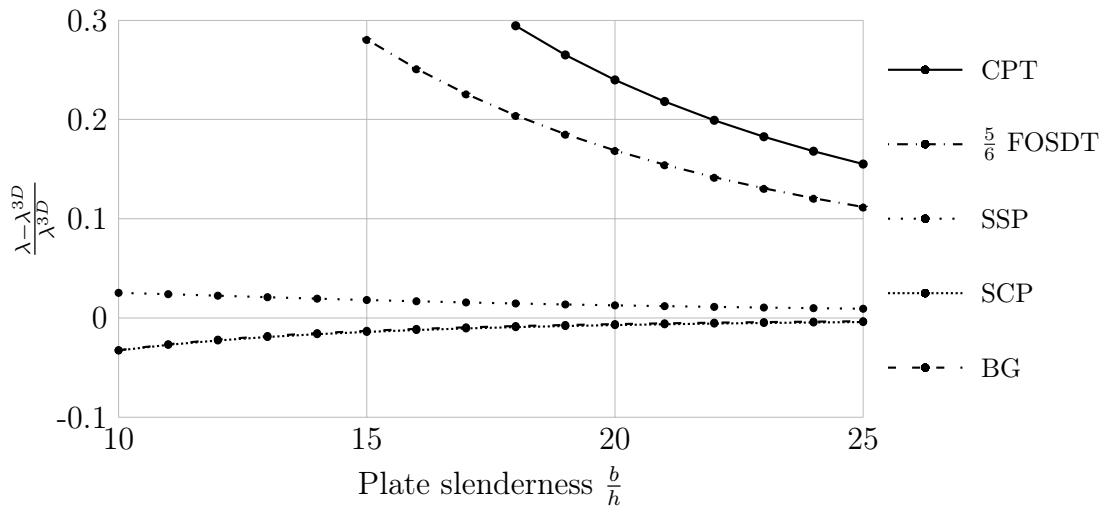


Figure 3.12 – Relative error of plate models compared to 3D results for a HSS 5-ply-CLT square panel

CHAPTER 3. THE BENDING-GRADIENT THEORY FOR THE LINEAR BUCKLING OF THICK PLATES: APPLICATION TO CROSS-LAMINATED-TIMBER PANELS

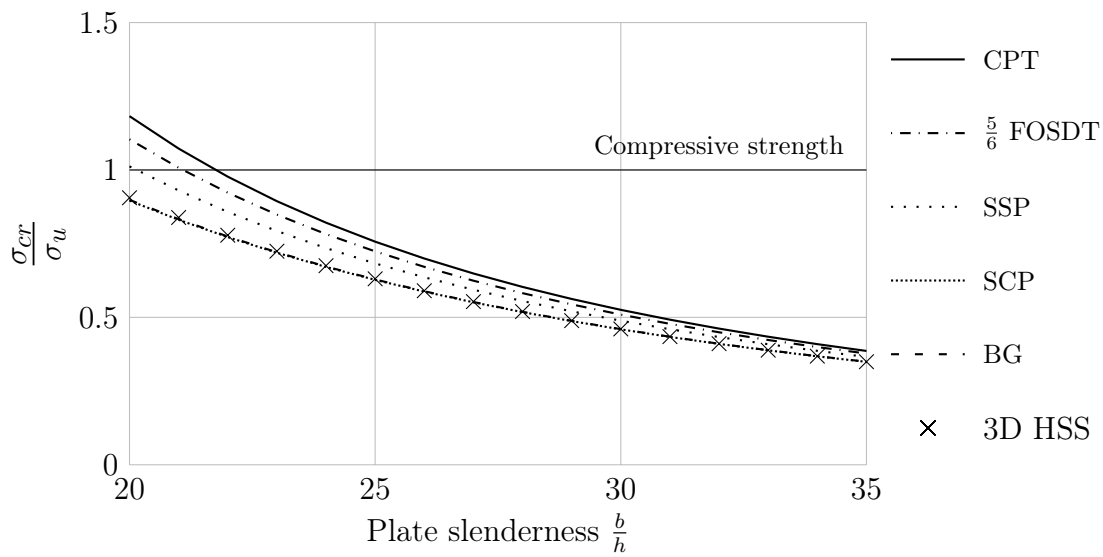


Figure 3.13 – Ratio between the buckling load and the compressive strength according to slenderness  $\frac{b}{h}$  for a HSS 3-ply-CLT square panel

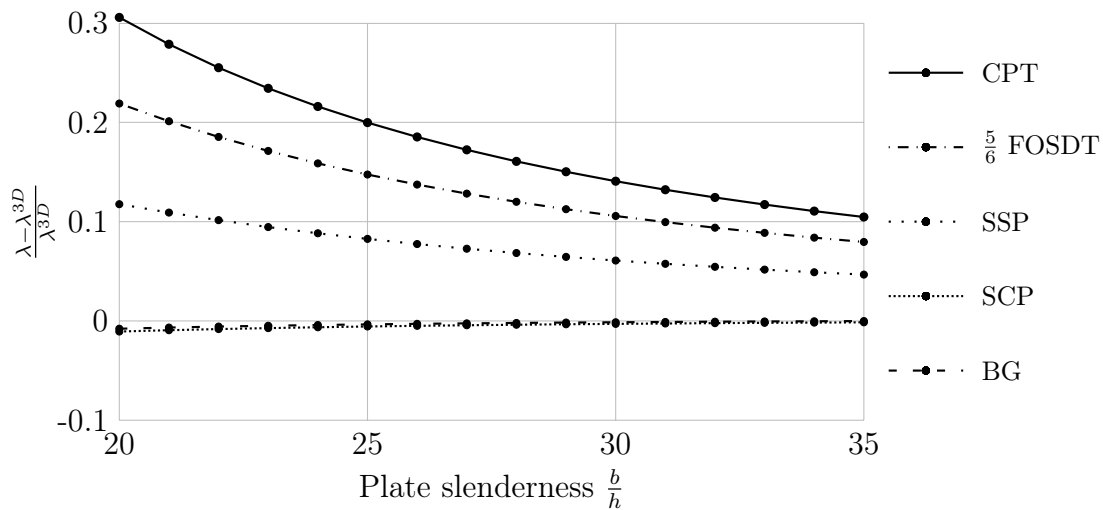


Figure 3.14 – Relative error of plate models compared to 3D results for a HSS 3-ply-CLT square panel

### 3.4. COMPARISON BETWEEN NUMERICAL RESULTS AND PLATE MODELS

theory on a Reissner-Mindlin model gives also good results for 5-ply CLT models but not for the 3-ply configuration contrary to the shear compliance projection (SCP). It is observed in Table 3.3 that the two projections are getting closer with an increasing number of plies.

Remarkably, the shear compliance projection gives results very close from the full Bending-Gradient: the difference between these two models is around 0.1% in the studied domain. Using the full Bending-Gradient seems thus not necessary in this case since the gain of accuracy of the buckling load determination compared to the shear compliance projection is negligible considering the difficulty introduced by keeping all Bending-Gradient unknowns. The shear compliance projection is thus very accurate to model global problem such as buckling. Nevertheless, it is not possible to describe the shear stress distribution through the thickness with this model, but it would be possible with the full Bending-Gradient theory which captures warping effects observed on Figure 3.8 by deriving the in-plane displacement field distribution through the thickness from the full Bending-Gradient model (Lebée and Sab, 2011a,b).

#### 3.4.3 Influence of the plate aspect ratio $\frac{a}{b}$

Figure 3.15 presents the ratio between the buckling load and the compressive strength of a HSS 5-ply CLT with a fixed slenderness  $\frac{b}{h} = 20$  for varying plate aspect ratios. Here, there are successively three modes:  $(m = 1, n = 1)$ ,  $(m = 2, n = 1)$  and  $(m = 3, n = 1)$ . For a better readability, the FOSDT and the shear stiffness projection are not plotted.

As previously observed the classical lamination model is not accurate for the three modes. Its error is larger for modes  $(m = 2, n = 1)$  and  $(m = 3, n = 1)$  than for the mode  $(m = 1, n = 1)$  and the transition ratios, where buckling loads of two different modes are equal, are higher than in the reference cases where  $(\frac{a}{b})^{tr} \approx 1.8$  then 3.1. On the contrary, the full Bending-Gradient theory and the shear compliance projection are very accurate.

The minimum buckling load for all aspect ratio  $\frac{a}{b}$  is conventionally used for the design of walls against buckling. In the Kirchhoff model, the critical aspect ratios of the mode  $(m = 1, n = 1)$  are 1.95, 1.36 and 1.23 for a 3-, 5- and 7-ply CLT panels respectively (see Table 3.3 and Equation 3.23). From the development of the expression (A.16), this critical ratio has been estimated to be equal to 1.22 for a 5-ply CLT with a slenderness  $\frac{b}{h} = 20$  in the Bending-Gradient theory. This estimation is in good agreement with what is observed on Figure 3.15.

On Figure 3.16, the relative error between plate models and 3D numerical results are plotted for a 5-ply CLT panel with a slenderness  $\frac{b}{h} = 20$  with a varying aspect ratio  $\frac{a}{b}$ . Only the mode  $(m = 1, n = 1)$  is plotted. As in previous sections, the full Bending-Gradient and its projections show the best results compared to other theories. The shear

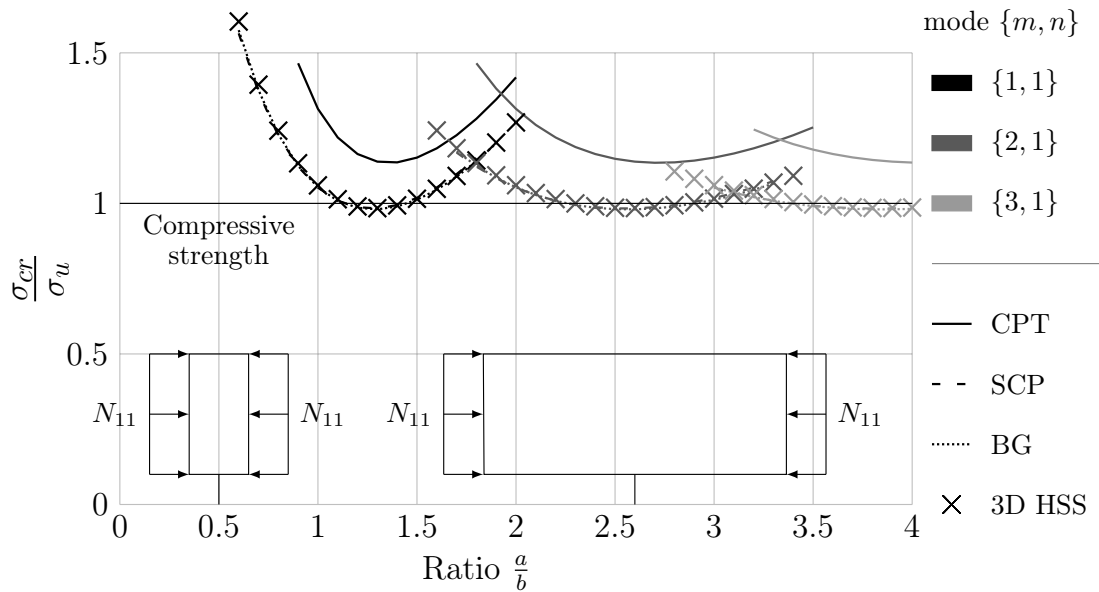


Figure 3.15 – Ratio between the buckling load and the compressive strength according to plate ratio  $\frac{a}{b}$  for a HSS 5ply-CLT with a slenderness  $\frac{b}{h} = 20$

compliance projection is here a little less accurate than previously but it is still better than the shear stiffness projection.

In the following, only the shear compliance projection and the Kirchhoff-Love models are compared to reference results. Indeed, the first one is the most accurate studied Reissner-Mindlin model and does not require the full Bending-Gradient model and the second one does not take into account shear effects as in the Eurocode 5 (European Committee for Standardisation, 1993).

### 3.4.4 Accuracy of the shear compliance stiffness projection for SSS plates

The aim of this section is to study the accuracy of the shear compliance stiffness for the case of soft simply supported CLT panels. Indeed, this boundary condition is closer to the actual case and is thus more appropriate to develop recommendations for the design of CLT. It is shown in the following that the shear compliance projection is still accurate for the buckling of SSS plates.

As it was mentioned in section 3.2.3, there is no closed-form solutions for such boundary conditions. Indeed, the boundary layer observed on Figure 3.7 involves a non-trivial stress distribution next to boundaries. For that reason, a 2D numerical study is performed using the finite element software Abaqus. Square quadratic elements S8R

### 3.4. COMPARISON BETWEEN NUMERICAL RESULTS AND PLATE MODELS

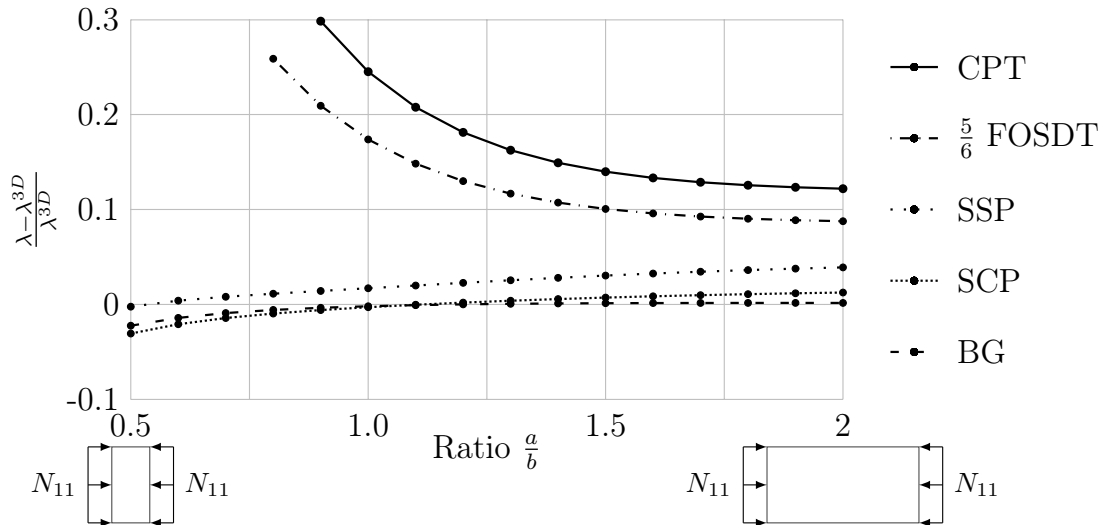


Figure 3.16 – Relative error compared to numerical results for a HSS 5ply-CLT panel with a slenderness  $\frac{b}{h}=20$

with 8 nodes are used. There are 5 degrees of freedom at each node corresponding to the kinematic unknowns in the Reissner-Mindlin model. A reduced integration is done to evaluate the material response in each element as recommended in the Abaqus documentation when using a regular mesh (ABAQUS, 2004). A convergence study was performed to fulfill the same accuracy as the 3D numerical study. The general shell section stiffness is given using the bending and the shear stiffness calculated using the shear compliance projection and computed in Table 3.3.

On Figure 3.17, the relative error of 2D numerical results is plotted when compared to 3D reference results for SSS 5-ply CLT plates with a fixed critical aspect ratio  $\frac{a}{b} = 1.22$  estimated in the previous section and for a varying slenderness  $\frac{b}{h}$ . It must be noticed that the Kirchhoff-Love model results are plotted here for HSS plates. Indeed, since shear effects are not considered in this model (the transverse rotation  $\varphi_t$  is equal to  $-u_{3,t}$ ),  $\varphi_t$  is then always zero on a simple support  $u_3 = 0$ . Only the condition HSS may be modeled in the CPT.

A very good accuracy  $\leq 1.5\%$  is found for the shear compliance projection in the studied domain. As previously observed, the accuracy increases with the plate slenderness  $\frac{b}{h}$ .

Finally, it may be concluded that the shear compliance projection is applicable to soft simply supported plates with a good accuracy by using Reissner-Mindlin finite elements. Recommendations for the design of CLT buckling may then be developed considering soft simple support boundary condition although there is no closed-form solution.

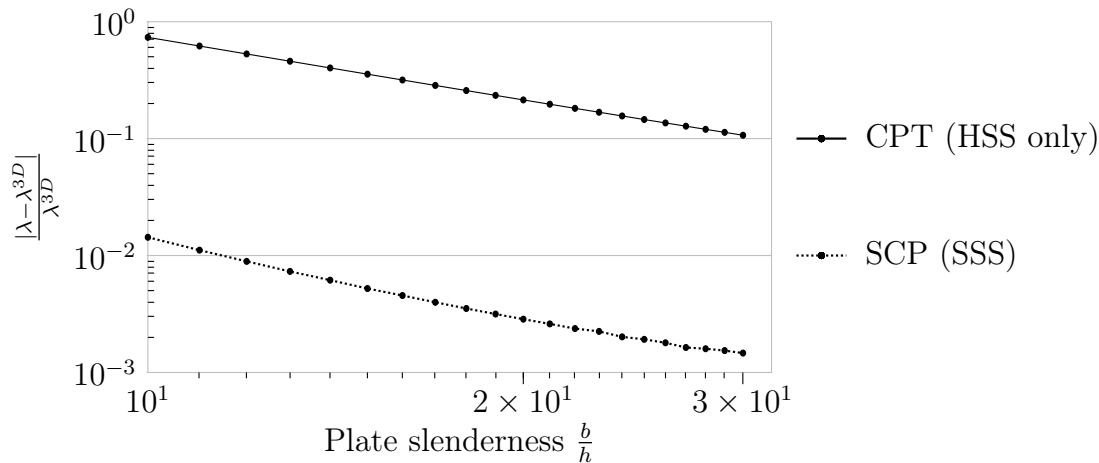


Figure 3.17 – Relative error of the critical buckling load of SSS plates 2D results compared to 3D SSS results for 5-ply CLT plates with an aspect ratio  $\frac{a}{b} = 1.22$

### 3.5 Conclusions

In this chapter, the Bending-Gradient theory was extended to linear buckling analysis and was applied to the case of rectangular CLT panels. Two projections of this theory on a Reissner-Mindlin model were presented: the shear compliance projection and the shear stiffness projection based on assumptions on the Bending-Gradient's kinematic or static degrees of freedom. A 3D numerical study was conducted in order to get reference results for the buckling of CLT panels. Results show that, qualitatively and quantitatively, the Bending-Gradient is well adapted for the study of the buckling of thick and highly anisotropic laminated plates such as CLT contrary to the FOSDT and the classical lamination theory. Moreover, the shear compliance projection of the Bending-Gradient is also very accurate for varying geometries contrary to the shear stiffness projection. The shear compliance projection seems thus more adapted than the full Bending-Gradient theory to engineering issues (such as recommendations) since it uses a simpler model, the Reissner-Mindlin model, without losing accuracy. Moreover, this model can also be used numerically to study soft simply supported plates by using Reissner-Mindlin finite element although there is no closed form solution. It was also noticed that the difference of buckling load between of the two boundary conditions (HSS and SSS) remain limited to 5%. To go further, the non-linear buckling will have to be considered in order to evaluate the post-buckling behavior of CLT plates. Perspectives of this study thus include the effect of plate imperfections such as initial plate shape, loading eccentricity or residual stress and the influence of the variations of mechanical characteristics in particular for the longitudinal Young modulus and the rolling shear stiffness which are of main importance.

### 3.5. CONCLUSIONS

---

---

## Buckling of CLT columns with initial imperfections

*In order to extend the problem to more realistic CLT panels, we study in this chapter the buckling of CLT walls with initial imperfections. In order to simplify the problem, we use the Timoshenko beam theory. We recall the classical Ayrton-Perry formula and, because of the low rolling shear strength in cross-layers, we also introduce a new shear criterion for CLT walls under compressive load.*

### 4.1 Introduction

In Chapter 3, the linear buckling analysis of CLT walls was investigated using several plate models. CLT walls were assumed perfectly straight and under a perfectly centered compressive load. Nonetheless, in actual structures, these assumptions may not always hold up. First, because of the manufacturing process, CLT panels are not perfectly straight. In the Eurocode 5 (European Committee for Standardisation, 1993), a maximum initial straightness imperfection of  $1/500$  of the span is recommended for Laminated Veneer Lumber (LVL) and Glued Laminated Timber and of  $1/300$  of the span for solid timber. The CLT Handbook (Karacabeyli and Douglas, 2013) suggests that the deviation of edges from the straight line between two corners must not exceed 1.6 mm for CLT which corresponds to  $1/2000$  of the length for a 3-meter high wall. Second, because of the connecting system, the load is not perfectly centered. In its guide for application, the company Stora Enso (2014) assumed that, because of the non-symmetrical load on vertical elements, an eccentricity of the load is considered equal to one sixth of the thickness of the CLT which corresponds to  $1/180$  of the length for a slenderness of 30. We note that eccentricity imperfections are much larger than straightness imperfections. Third, during the manufacturing process, residual stresses have been generated particularly during the gluing and pressing process.

To the author's knowledge, the buckling of a column with initial imperfections was first studied by Ayrton and Perry (1886). All initial imperfections lead to additional bending moments, so that the equilibrium is changed. From this equilibrium, it is possi-

#### 4.1. INTRODUCTION

---

ble to express deflections of the wall as a function of the compressive load contrary to the linear buckling analysis where deflections occur only at bifurcation. These deflections are not a linear function of the compressive load. Particularly, when the compressive load is equal to the critical buckling load, the column is unstable: the column is then stable only if the compressive load is lower than the buckling load.

Then, a compressive strength criterion is also introduced. The maximum compressive stress in the column is due to direct compressive load and to additional bending stress which is proportional to the deflections of the column. By comparing this maximum stress expression to the compressive strength, Ayrton and Perry (1886) suggested a strength criterion also called the Ayrton-Perry formula. This criterion is more conservative than both stability criterion and pure compressive strength criterion without considering initial imperfections. The design criterion of timber columns in the Eurocode 5 (European Committee for Standardisation, 1993) is based on this formula using the Euler beam model. In order to extend this model to CLT walls, Thiel (2013) suggested to include shear effects by using the Timoshenko beam model. Particularly, the Timoshenko critical buckling load is used instead of the Euler buckling load.

From the equilibrium of the column, additionally to bending moments, the deflection leads to additional shear forces in the column. Nonetheless, contrary to other timber products such as Glued Laminated Timber (GLT) or Laminated Veneer Lumber (LVL) and because of the configuration of CLT and the low rolling shear strength in cross-layers, a rolling shear failure could occur in cross-layers due to an excessive shear. No such verification are suggested for timber columns (European Committee for Standardisation, 1993) and for CLT columns Thiel (2013) to the author's knowledge. We propose then in this chapter a shear criterion and compare it to the Ayrton-Perry formula in order to check if it is relevant or not.

Finally, contrary to other timber elements, CLT walls can be connected to other vertical timber elements, called wall-to-wall connection (Karacabeyli and Douglas, 2013), at their lateral faces. These connections lead to additional boundary conditions on lateral edges which can not be taken into account by beam models (Thiel and Krenn, 2016) (Chapter 3). It is then necessary to check if the Ayrton-Perry formula and the shear criterion can be extended to plate models in order to take into account these additional boundary conditions.

In Section 4.2, the work of Ayrton and Perry (1886) is recalled using the Timoshenko beam model on a CLT column. Then, in Section 4.3, a shear force criterion is introduced and compared to the Ayrton-Perry formula for two strength class of CLT and for varying initial imperfections.

## 4.2 Buckling of a columns with imperfections

### 4.2.1 Linear buckling of a column without imperfections

We consider a simply supported rectangular column with a length  $l$ , a width  $b$  and a thickness  $h$  corresponding to  $x$ ,  $y$  and  $z$  directions respectively (Figure 4.1). The geometrical slenderness around  $y$  and  $z$  axis are defined as:

$$\lambda_y = \frac{l}{\sqrt{\frac{I_y}{S}}} \quad \text{and} \quad \lambda_z = \frac{l}{\sqrt{\frac{I_z}{S}}}$$

where  $S$  is the effective section of the beam and  $I_y$  and  $I_z$  are the effective quadratic moments around  $y$  and  $z$  axis respectively of an heterogeneous section. Because of the geometry of CLT panels,  $\lambda_z$  is assumed small compared to  $\lambda_y$  that is why only the buckling in  $z$  direction is studied. The elastic Young modulus in  $x$  direction is noted  $E_0(z)$  and the shear modulus between  $x$  and  $z$  is noted  $G_0(z)$ .

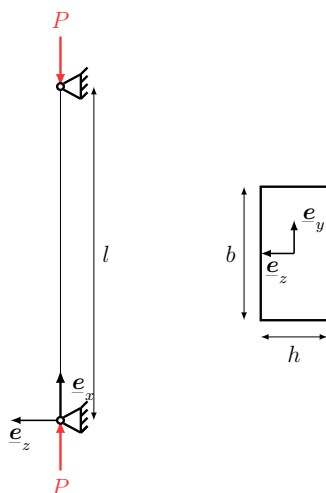


Figure 4.1 – Beam under in-plane compression

In the Timoshenko beam model, the 3D displacement field  $\mathbf{u}(x, y, z)$  is assumed as follows:

$$\begin{cases} u_1(x, y, z) = \varphi(x)z & (4.1a) \\ u_2(x, y, z) = 0 & (4.1b) \\ u_3(x, y, z) = f(x) & (4.1c) \end{cases}$$

where  $f(x)$  is the deflection of the beam at the neutral axis and  $\varphi(x)$  is the rotation of the section (Figure 4.2). The generalized shear strain  $\gamma(x)$  complies with the compatibility

## 4.2. BUCKLING OF A COLUMNS WITH IMPERFECTIONS

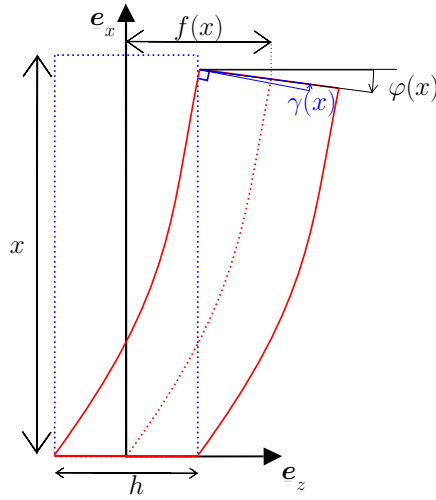


Figure 4.2 – Definition of the deflection  $f(x)$ , of the rotation of the section  $\varphi(x)$  and of the global shear strain  $\gamma(x)$

equation:

$$\gamma(x) = \varphi(x) + f'(x) \quad (4.2)$$

where  $\bullet' = \frac{d\bullet}{dx}$  stands for the first derivative of the variable  $\bullet$ .

The bending moment  $M(x)$  and the shear force  $Q(x)$  are defined as global stress fields as follows:

$$\left\{ \begin{array}{l} M(x) = - \int_{-\frac{h}{2}}^{\frac{h}{2}} bz\sigma_{xx}(x, z)dz, \\ Q(x) = \int_{-\frac{h}{2}}^{\frac{h}{2}} b\sigma_{xz}(x, z)dz. \end{array} \right. \quad (4.3a)$$

$$(4.3b)$$

where  $\sigma_{xx}$  and  $\sigma_{xz}$  are section stress fields. The constitutive relationships between the bending moment  $M$  and the shear force  $Q$  and global kinematic fields are:

$$\left\{ \begin{array}{l} M(x) = D_0\varphi'(x) \\ Q(x) = F_0\gamma(x) \end{array} \right. \quad (4.4a)$$

$$(4.4b)$$

From the work of Jourawski (1856), the bending stiffness  $D_0$  and the shear stiffness  $F_0$

of the beam may be derived as:

$$\left\{ \begin{array}{l} D_0 = \int_{-\frac{h}{2}}^{\frac{h}{2}} bz^2 E_0(z) dz, \end{array} \right. \quad (4.5a)$$

$$\left\{ \begin{array}{l} \frac{1}{F_0} = \frac{b}{D_0^2} \int_{-\frac{h}{2}}^{\frac{h}{2}} \left( \int_{-\frac{h}{2}}^z E_0(t) t dt \right)^2 \frac{1}{G_0(z)} dz. \end{array} \right. \quad (4.5b)$$

In order to study first the linear buckling of the column, we assume that the column is perfectly straight. A centered load  $P$  is applied at each end of the beam (Figure 4.1). The static equilibrium on the deformed configuration for small perturbations writes as:

$$\left\{ \begin{array}{l} Q = M' \\ M - Pf = 0 \end{array} \right. \quad (4.6a)$$

$$(4.6b)$$

From the constitutive relationship (4.4), the problem can be cast as the following differential equation:

$$f'' + K_v^2 f = 0 \quad (4.7)$$

where:

$$K_v^2 = K^2 \frac{1}{1 - \frac{P}{F_0}} \quad \text{and} \quad K^2 = \frac{P}{D_0}.$$

$K$  is directly related to the Euler critical buckling load  $P_{E,0}$  and  $K_v$  includes a correction related to the shear compliance  $F_0$ . Considering the boundary conditions  $f(0) = f(l) = 0$ , non-trivial solutions of this eigenvalue problem write as:

$$f(x) = A \sin K_v x$$

where  $K_v = n\frac{\pi}{l}$ ,  $n \in \mathbb{N}^*$  and  $A$  a constant. These are associated to eigenvalues  $P_{cr,0}$ , also called critical buckling load:

$$\frac{1}{P_{cr,0}} = \frac{1}{P_{E,0}} + \frac{1}{F_0} \quad \text{where} \quad P_{E,0} = D_0 n^2 \frac{\pi^2}{l^2} \quad (4.8)$$

$P_{E,0}$  is the buckling load associated to the Euler beam theory where a zero shear compliance  $\frac{1}{F_0}$  is assumed. It is observed here that the contribution of the shear stiffness  $F_0$  does not depend on the mode  $n$ . In the following, we only consider the first buckling mode  $n = 1$  since it corresponds to the lowest critical buckling load  $P_{cr,0}$ . Finally it is possible to express the expression of  $\varphi(x)$  and  $\gamma(x)$  at bifurcation:

$$\varphi(x) = -\frac{P_{cr,0}}{P_{E,0}} \frac{\pi}{l} A \cos \frac{\pi x}{l} \quad \text{and} \quad \gamma(x) = \frac{P_{cr,0}}{F_0} \frac{\pi}{l} A \cos \frac{\pi x}{l}$$

## 4.2. BUCKLING OF A COLUMNS WITH IMPERFECTIONS

For a fixed amplitude  $A$ , when the slenderness is low, the shear force may require rolling shear strength verification.

In order to quantify the shear stress at bifurcation, it is of interest to consider the results from the 3D numerical study on the buckling of CLT walls in Section 3.3. Note that the critical buckling load for beam (4.8) is similar to the one derived numerically assuming that there are free lateral edges. The stress state calculated numerically at bifurcation is proportional to the amplitude of the mode but does not correspond to an actual state of the CLT wall since it is located at a bifurcation point. Nonetheless, it is possible to calculate the ratio between the maximum bending stress in the longitudinal layers and the maximum shear stress in the cross layers. By comparing this ratio to the ratio between the longitudinal bending strength and the rolling shear strength, it is possible to estimate the failure mode of the CLT wall under this state. According to Schickhofer et al. (2016), the ratio between bending strength and rolling shear strength varies from 17 for the strength class CL24h with a board aspect ratio  $\frac{2b_l}{t_l} \geq 4$  to 35 for the strength class CL28h with a board aspect ratio  $\frac{2b_l}{t_l} < 4$ . The ratio between the maximum bending stress and the maximum shear stress estimated numerically at bifurcation in Chapter 3 for a 3-ply CLT varies strongly with the slenderness  $\frac{b}{h}$  of the beam: for  $\frac{b}{h} = 40$ , it is equal to approximately 49, for  $\frac{b}{h} = 20$ , it is equal to approximately 28. It appears, that the ratio between stress levels and the ratio between strengths are comparable for low slenderness with board aspect ratios lower than 4. This means that failure may also occur because of excessive shear force in addition to the usual Ayrton-Perry criterion based on combined longitudinal compression and bending. Then in the following, we will introduce a shear criterion for CLT walls under compressive load additionally to the conventional Ayrton Perry formula.

### 4.2.2 Buckling of a column with initial imperfections

This section is based on the works of Ayrton and Perry (1886) for the buckling of columns with initial imperfections. We consider that the beam initial and free of stress geometry is

$$f_0(x) = e_0 + w_0 \sin\left(x \frac{\pi}{l}\right).$$

This imperfection corresponds to a load eccentricity  $e_0$  and a straightness defect  $w_0$  related to the first buckling mode (Figure 4.3). The initial imperfection  $f_0(x)$  is small compared to the length  $l$ . Note here that there may be also an initial rotation imperfection  $\varphi_0(x)$ . Nonetheless,  $\varphi_0(x)$  has no impact on the column equilibrium. Then we note  $\varphi(x)$  and  $\gamma(x)$  the additional rotation and shear strain which are directly related to the bending moment  $M(x)$  and the shear force  $Q(x)$ :

$$\begin{cases} M(x) = D_0 \varphi'(x) & (4.9a) \\ Q(x) = F_0 \gamma(x) & (4.9b) \end{cases}$$

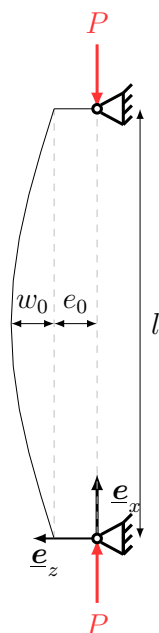


Figure 4.3 – Beam with initial imperfection under in-plane compression

By noting  $f(x)$  as the sum of initial imperfections and elastic deflection, the compatibility equation becomes (4.2):

$$\gamma(x) = \varphi(x) + f'(x) - f_0'(x) \quad (4.10)$$

By injecting these expression in the equilibrium (4.6), a new differential equation is obtained:

$$f''(x) + K_v^2 f(x) + \frac{\pi^2}{l^2} \frac{w_0}{1 - \frac{P}{F_0}} \sin \frac{\pi x}{l} = 0 \quad (4.11)$$

Contrary to the differential equation (4.7) for a column without imperfections, there is an additional term, the third one, which depends on  $x$ . Then, a solution of this problem takes the form

$$f(x) = A \sin K_v x + B \cos K_v x + C \sin \frac{\pi x}{l}$$

where  $A$ ,  $B$ ,  $C$ , are constants. By injecting this solution in the differential equation (4.11), the constant  $C$  of the particular solution can be estimated as:

$$C = \frac{w_0}{\left(1 - \frac{P}{F_0}\right) \left(1 - K_v^2 \frac{l^2}{\pi^2}\right)} = \frac{w_0}{1 - \frac{P}{P_{cr,0}}}$$

$C$  is finite only if  $P < P_{cr,0}$ : the column is stable only if the compressive load  $P$  is lower

## 4.2. BUCKLING OF A COLUMNS WITH IMPERFECTIONS

than the critical buckling load  $P_{cr,0}$ . Granted that  $P < P_{cr,0}$  the solution is obtained by considering boundary conditions  $f(0) = f(l) = e_0$ :

$$f(x) = \frac{w_0}{1 - \frac{P}{P_{cr,0}}} \sin \frac{\pi x}{l} + e_0 \left( \cos K_v x + \tan \frac{K_v l}{2} \sin K_v x \right) \quad (4.12)$$

The maximum deflection is at the mid-span (Ayrton and Perry, 1886) and is noted  $w = f\left(\frac{l}{2}\right)$ . It is then found that:

$$w = \frac{w_0}{1 - \frac{P}{P_{cr,0}}} + \frac{e_0}{\cos \frac{\pi}{2} \sqrt{\frac{P}{P_{E,0}} \frac{1}{1 - \frac{P}{P_{cr,0}}}}} \quad (4.13)$$

The mid-span deflection  $w$  is then a linear combination of two functions  $\alpha(P)$  and  $\beta(P)$ :

$$\alpha(P) = \frac{1}{1 - \frac{P}{P_{cr,0}}} \quad \text{and} \quad \beta(P) = \frac{1}{\cos \frac{\pi}{2} \sqrt{\frac{P}{P_{E,0}} \frac{1}{1 - \frac{P}{P_{cr,0}}}}}$$

It is noted that  $\alpha(0) = \beta(0) = 1$  and that  $\alpha(P)$  and  $\beta(P)$  are infinite for  $P = P_{cr,0}$ . Ayrton and Perry (1886) observed that for Euler beam ( $\frac{1}{F_0} = 0$ ),  $\beta(P) \approx \frac{6}{5}\alpha(P)$ , particularly for  $0.2 < \frac{P}{P_{E,0}} < 0.9$ . Then, since  $\alpha(P)$  has a simpler form, Ayrton and Perry (1886) suggested to combine both straightness imperfections  $w_0$  and eccentricity load  $e_0$  in an equivalent straightness default  $w_{0,eq}$ :

$$w_{0,eq} = w_0 + \frac{6}{5}e_0$$

We note here that this assumption is not true for Timoshenko beam theory. In the Figure 4.4, the ratio between functions  $\beta(P)$  and  $\alpha(P)$  is plotted for varying ratio  $\frac{P}{P_{cr,0}}$  and for varying ratio between the Euler and the Timoshenko critical buckling loads  $\frac{P_{E,0}}{P_{cr,0}}$  which is a measure of shear effects on the critical buckling load. The Figure 4.4 includes most of CLT configuration. It is observed that the assumption of Ayrton and Perry (1886)  $\beta(P) = 1.2\alpha(P)$  is generally an overestimation of the load eccentricity which is conservative. Given that the load  $P$  is lower than one half of the critical buckling load  $P_{cr,0}$ , which is a reasonable assumption in actual structures,  $\beta(P)$  and  $\alpha(P)$  are close and the following equivalent straightness default  $w_{0,eq}$  seems more relevant:

$$w_{0,eq} = w_0 + e_0 \quad (4.14)$$

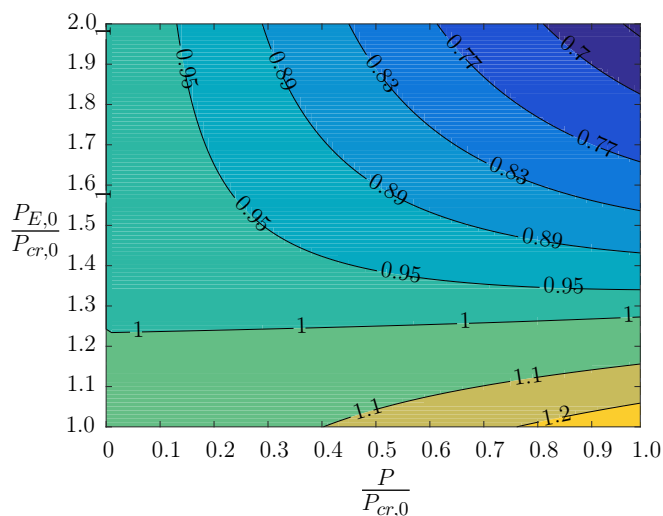


Figure 4.4 – Ratio  $\frac{\beta(P)}{\alpha(P)}$  for varying ratios  $\frac{P}{P_{cr,0}}$  and  $\frac{P_{E,0}}{P_{cr,0}}$

In the following, the initial imperfection  $f_0(x)$  is assumed as:

$$f_0(x) = w_{0,eq} \sin\left(\frac{\pi x}{l}\right)$$

Then, the maximum deflection  $w$  is expressed as:

$$w = \frac{w_{0,eq}}{1 - \frac{P}{P_{cr,0}}} \quad (4.15)$$

The mid-span elastic deflection  $w_{el}$  associated to the compression of a column is then expressed as:

$$w_{el} = w - w_{0,eq} = \frac{w_{0,eq}}{1 - \frac{P}{P_{cr,0}}} - w_{0,eq} = \frac{w_{0,eq}}{\frac{P_{cr,0}}{P} - 1} \quad (4.16)$$

From the constitutive equation (4.9b) and the equilibrium (4.6a,4.6b), the shear strain  $\gamma$  in the column is expressed as:

$$\frac{l}{\pi} \gamma(x) = \frac{P}{F_0} \frac{w_{0,eq}}{1 - \frac{P}{P_{cr,0}}} \quad (4.17)$$

### 4.2.3 Ayrton and Perry criterion

The longitudinal stress  $\sigma_{xx}$  in the section is the combination of stress due to the bending moment  $M$  and to the normal effort  $N = -P$  as follows:

$$\sigma_{xx}(x) = -\frac{P}{EA}E_0(z) + \frac{M(x)}{D_0}E_0(z)z$$

where  $\overline{EA} = \int_{-\frac{h}{2}}^{\frac{h}{2}} bE_0(z)dz$  is the normal stiffness of the beam. We note  $\sigma_{\max}$  the maximum compressive stress in absolute terms.  $\sigma_{\max}$  is obtained at mid-span, where the bending moment  $M$  is maximum. For most columns, including CLT columns, the maximum compressive stress is at the lower face for  $z = -\frac{h}{2}$ :

$$\sigma_{\max} = \frac{P}{EA}E_L + \frac{Pw}{D_0} \frac{h}{2} E_L$$

We note  $\sigma_u$  the ultimate compressive load corresponding generally to the elastic limit in compression in wood engineering. The ratio between the maximum stress  $\sigma_{\max}$  in the column and the ultimate compressive load  $\sigma_u$  has then the following expression:

$$\frac{\sigma_{\max}}{\sigma_u} = \frac{P}{P_u} \left( 1 + \frac{1}{1 - \frac{P}{P_{cr,0}}} \omega \right) \quad (4.18)$$

where  $P_u = \sigma_u \frac{\overline{EA}}{E_L}$  is the ultimate compressive load,  $E_L$  is the longitudinal Young modulus and  $\omega = \frac{\overline{EA}hw_{0,eq}}{2D_0}$  is a measure of initial imperfections. In Equation (4.18), the strength criterion  $\frac{\sigma_{\max}}{\sigma_u} < 1$  is expressed as a criterion on a polynomial equation in  $P$ :

$$P^2 - [(1 + \omega) P_{cr,0} + P_u] P + P_u P_{cr,0} > 0$$

The discriminant  $\Delta$  of this polynomial equation can be expressed as a sum of positive terms:

$$\begin{aligned} \Delta &= [(1 + \omega) P_{cr,0} + P_u]^2 - 4P_u P_{cr,0} \\ &= (P_{cr,0} - P_u)^2 + P_{cr,0} \omega [2(P_{cr,0} + P_u) + P_{cr,0} \omega] \end{aligned}$$

Then roots in  $P$  of this polynomial equation are real. Since  $P_u P_{cr,0} > 0$ , both roots of this polynomial equation are positive. Then, to satisfy the strength criterion (4.18),  $P$  must be lower than the smallest root which can be written as:

$$\frac{P}{P_u} < \frac{2}{(1 + \omega + \lambda_{rel}^2) + \sqrt{(1 + \omega + \lambda_{rel}^2)^2 - 4\lambda_{rel}^2}} = \bar{N}_{AP} \quad (4.19)$$

where  $\lambda_{\text{rel}}$  is the relative slenderness defined as:

$$\lambda_{\text{rel}} = \sqrt{\frac{P_u}{P_{cr,0}}} \quad (4.20)$$

$\bar{N}_{\text{AP}}$  is the normalized compressive limit according to the Ayrton-Perry criterion. It is observed that for  $\omega = 0$ , corresponding to a perfectly straight column, the criterion becomes  $\bar{N}_{\text{AP}} = \inf(P_c, P_{cr,0})$  which is in agreement with a perfect column.

In the Eurocode 5 standards (European Committee for Standardisation, 1993) and then in (Thiel, 2013) this criterion has been adapted:

- First, it is used only when the critical buckling load is low enough:  $\lambda_{\text{rel}} > 0.3$ . Otherwise, the criterion is based on the compressive strength only;  $P < \frac{f_{c,0,k} k_{\text{mod}}}{\gamma_M} \frac{EA}{E_L}$  where  $f_{c,0,k}$  is the characteristic compressive strength,  $k_{\text{mod}}$  is a modification factor depending on the service class and on the duration of loading and  $\gamma_M$  is a coefficient taking into account the natural variability of the material;
- Second, the design compressive strength  $f_{d,0,k} = \frac{f_{c,0,k} k_{\text{mod}}}{\gamma_M}$  is used in the expression of  $P_c$  in the left side of the criterion (4.19) whereas the characteristic compressive strength  $f_{c,0,k}$  is used to define the relative slenderness  $\lambda_{\text{rel}}$ ;
- Third, characteristic modulus of elasticity  $E_{0,05}$ , corresponding to the fifth percentile, is used to calculate the critical buckling load  $P_{cr,0}$ ;
- Finally, the measure of initial imperfection  $\omega$  is defined as a function of the relative slenderness:  $\omega = \beta_c (\lambda_{\text{rel}} - 0.3)$  where  $\beta_c$  is a factor taking into account imperfections.

Hence the Ayrton-Perry criterion has been adapted to timber columns in the Eurocode 5 using several corrections mainly due to variations of the mechanical properties of wood. We note here that the definition of initial imperfections is not linked directly with the length of the column but with the relative slenderness and no details are provided on the origin of the value of  $\beta_c$ .

## 4.3 Proposed shear force criterion

In the previous chapter, we recalled the Ayrton-Perry criterion which is currently adopted in the Eurocode 5. In this section, we propose a new criterion for the design of CLT walls based on the rolling shear failure.

### 4.3.1 Definition of the shear criterion

We assume here that the shear force failure and the compression failure are not interacting since bending and shear effects are elastically uncoupled in the Timoshenko beam model and since the compression failure and the shear failure occurs at different

### 4.3. PROPOSED SHEAR FORCE CRITERION

locations. Indeed, the compression failure occurs at mid-span whereas the shear failure occurs at support ends. Moreover, compression failure occurs in external longitudinal layers whereas shear failure occurs in internal cross-layers.

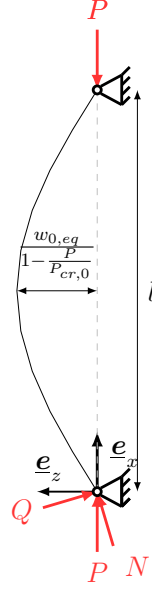


Figure 4.5 – Deflection of the beam at the equilibrium

From the equilibrium (4.6) and the expression of the deflection (4.15), the maximum shear force  $Q_{\max}$  is at support ends and is given by:

$$Q_{\max} = \frac{\pi}{l} \frac{P w_{0,eq}}{1 - \frac{P}{P_{cr,0}}}$$

This expression can be found geometrically from the decomposition of the external force  $P$  in a normal force  $N$  and a transverse force  $Q = P f'(0)$  (Figure 4.5). Following the approach of Jourawski (1856) (Equation A.10), the expression of the shear stress  $\sigma_{xz}(z_0)$  is given by:

$$\sigma_{xz}(x, z_0) = \frac{Q(x)}{D_0} \int_{z_0}^{\frac{h}{2}} E_0(z) z dz$$

In CLT, the maximum shear stress must be compared to the ultimate rolling shear strength in cross-layers  $\sigma_{rt,u}$  and to the ultimate longitudinal shear strength in longitudinal layers  $\sigma_{lr,u}$ . We note  $Q_u$  the ultimate shear force defined as:

$$Q_u = \tau_u \frac{D_0}{\int_{z_0}^{\frac{h}{2}} E_0(z) z dz} \quad (4.21)$$

where  $\tau_u$  is the ultimate shear strength at  $z_0$ . Then, the shear criterion of CLT wall can be given by:

$$\frac{P}{P_u} < \frac{1}{\frac{\pi w_{0,eq} P_u}{l Q_u} + \lambda_{rel}^2} = \bar{N}_\tau \quad (4.22)$$

where  $\bar{N}_\tau$  is the relative compressive limit according to the shear criterion. It is noted here that if  $\frac{\pi w_{0,eq} P_u}{l Q_u} \ll \lambda_{rel}^2$ , this criterion is equivalent to the stability criterion  $P < P_{cr,0}$ . Nonetheless, because of the high strength contrast between bending strength  $\sigma_c$  and rolling shear strength  $\sigma_{rt}$  and because of high eccentricity of the load suggested by Stora Enso (2014),  $\frac{\pi w_{0,eq} P_u}{l Q_u}$  is not always negligible for CLT walls compared to  $\lambda_{rel}^2$ .

Then, in the following, we compare the Ayrton-Perry criterion and the proposed shear criterion to observe if the new one is relevant.

### 4.3.2 Comparison between Ayrton-Perry formula and shear criterion

In this section, we compare the Ayrton-Perry formula and the shear criterion defined in Sections 4.2.3 and 4.3.1. Two CLT configurations called CLT1 and CLT2 are considered in this section following Schickhofer et al. (2016) corresponding to strength class CLT24h with a board aspect ratio  $\frac{2b_l}{t_l} \geq 4$  and to an hypothetical strength class CLT32h with a board aspect ratio  $\frac{2b_l}{t_l} < 4$ . Even if the strength class CLT32h has not been suggested, such strength class could be used in the future for very tall timber buildings. As suggested in the Eurocode 5, 5th percentile is used in calculation corresponding to 5/6 of the mean value as plotted in Table 4.1. We set the creep factor  $k_{def} = 1.0$  and the factor  $k_{mod} = 1.1$  since we consider here instantaneous load with no distinction on the direction (European Committee for Standardisation, 1993). 3-ply configuration is used where each ply has the same thickness.  $D_0$  (4.5a),  $F_0$  (4.5b) and  $Q_u$  (4.21) are calculated assuming that the cross-layer Young modulus  $E_C = 0$ .

Characteristic (MPa)	$\sigma_u$	$\tau_u$	$E_{L,0,05}$	$G_{LZ,0,05}$	$G_{CZ,0,05}$	$k_{mod}$	$k_{def}$
CLT1	24	1.4	$\frac{5}{6}11600$	$\frac{5}{6}650$	$\frac{5}{6}100$	1.1	1.0
CLT2	32	0.8	$\frac{5}{6}11600$	$\frac{5}{6}650$	$\frac{5}{6}65$	1.1	1.0

Table 4.1 – Elastic and strength properties of Norway Spruce CLT1 and CLT2 (Schickhofer et al., 2016)

In the Ayrton-Perry formula, it is assumed that initial imperfections are small compared to the length of the column. By taking directly the eccentricity of the load as  $\frac{h}{6}$  as suggested in (Thiel and Schickhofer, 2010), the assumption of small initial imperfections is not valid for small slenderness  $\frac{l}{h}$ . Hence, we choose to express initial

### 4.3. PROPOSED SHEAR FORCE CRITERION

imperfections as a function of the length only. Three cases are then studied:

- $w_{0,eq} = 0$  for the case of a perfect column;
- $w_{0,eq} = \frac{l}{500}$  as recommended in the Eurocode 5;
- $w_{0,eq} = \frac{l}{100}$  corresponding, for a slenderness  $\frac{l}{h} \approx 21$ , to an initial straightness defect of  $\frac{l}{500}$  added to a load eccentricity of  $\frac{h}{6}$  according to (4.14).

In Figures 4.6 and 4.7, Ayrton-Perry criterion is plotted using both Euler (black curves) and Timoshenko (blue curves) beam theories and is compared to the shear criterion (red curves). Moreover, a distinction is made between no initial imperfection, an initial imperfection of respectively  $w_{0,eq} = \frac{l}{500}$  and of  $w_{0,eq} = \frac{l}{100}$  plotted with continuous line, densely and loosely dashed lines respectively. Note that Ayrton-Perry criterion calculated here is not exactly the same as calculated in the Eurocode 5 since imperfections are assumed directly from the span and not from the relative slenderness. Furthermore, the design compressive strength, including the correction  $k_{mod}$  is used in the calculation of the relative slenderness  $\lambda_{rel}$  (4.20). Figure 4.6 stands for CLT1 configuration and Figure 4.7 stands for CLT2 configuration. Here, results are directly plotted as function of the slenderness  $\frac{l}{h}$  since  $\lambda_{rel}^2$  is not proportional to the slenderness of the column when using Timoshenko critical buckling load in (4.20).

First it is noted, by comparing Euler and Timoshenko beam models, that shear elastic effects can be relatively significant on the Ayrton-Perry criterion up to 9% for  $w_{0,eq} = \frac{l}{100}$ . Nonetheless, these effects are lower than what observed for linearized critical buckling loads in Chapter 3. Indeed, at low slenderness, shear effects have a strong impact on the critical buckling load but the relative slenderness  $\lambda_{rel}$  is low. As a consequence, the initial imperfection  $\omega$  has a stronger impact on the Ayrton-Perry criterion (4.19) than the critical buckling load  $P_{cr,0}$ . On the opposite, at high slenderness, the critical buckling load has a strong impact on the Ayrton-Perry criterion (4.19) but shear effects have a lower impact on the critical buckling load.

Second, the amplitude of initial imperfection has a strong influence on the Ayrton-Perry critical load particularly when the critical buckling load  $P_{cr,0}$  and the characteristic compressive load  $P_u$  are comparable. The Ayrton-Perry critical load  $\bar{N}_{AP}$  is then reduced up to 33% for  $w_0 = \frac{l}{500}$  and to 58% for  $w_0 = \frac{l}{100}$ .

Third it is observed in Figure 4.7 that, for CLT2, the shear criterion may be relevant for large initial imperfection  $w_{0,eq} = \frac{l}{100}$  where the shear criterion is lower than the Ayrton-Perry criterion for slenderness lower than 15. We note here that CLT2 is an extreme case since there is a very strong stiffness and strength contrast between longitudinal-layer and cross-layer stiffness. Then the shear criterion may be relevant but only when rolling shear properties, particularly the rolling shear strength, are low. It was observed by Ehrhart et al. (2015) that rolling shear properties of CLT are very sensitive to the board aspect ratio  $\frac{w_l}{t_l}$ . Hence further studies on the rolling shear strength of CLT walls and its impact on the shear criterion seems necessary. This shear criterion could be particularly relevant when using lower strength class in cross-layers which is

a common practise. Moreover, it could also be relevant for the design of new wooden products such as CLT panels with regular gaps in internal layers (Franzoni et al., 2016a, 2017a).

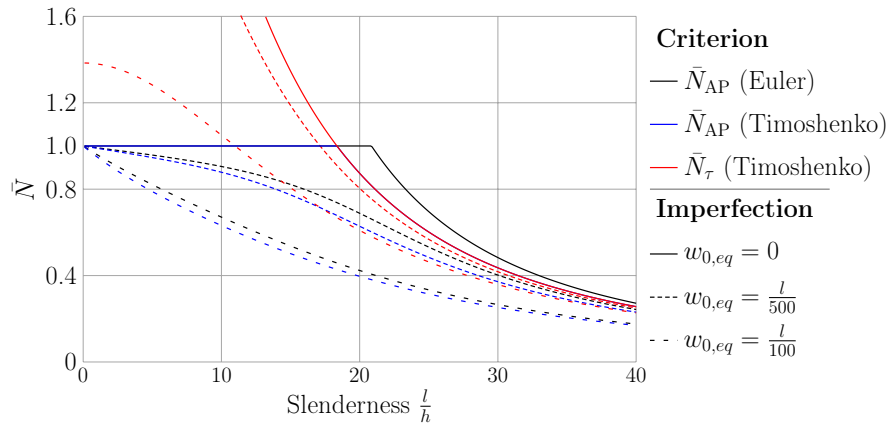


Figure 4.6 – Ayrton-Perry formula (A-P) and shear criterion for CLT1 configuration

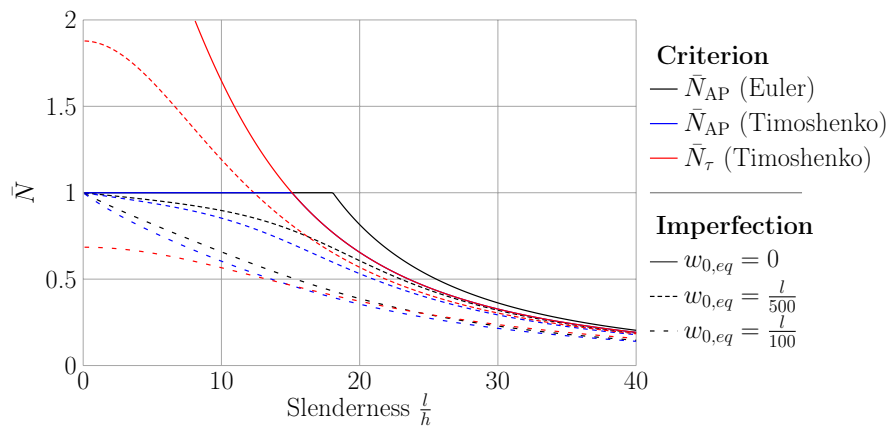


Figure 4.7 – Ayrton-Perry (A-P) criterion and shear criterion for CLT2 configuration

## 4.4 Conclusion

In this chapter, we recalled the Ayrton-Perry criterion of a CLT column under compression and we introduced a shear criterion for CLT walls. It was observed that the shear criterion can be relevant for thick walls and for CLT with a low cross-layer shear strength and in a less critical way, a low cross-layer shear stiffness. Hence further research on the impact of the shear strength on the relevance of this shear criterion seems

#### 4.4. CONCLUSION

---

necessary. Moreover, the Ayrton-Perry criterion has been extended to Reissner-Mindlin plate models in Appendix A.3. Thus, the design of CLT walls suggested by Thiel (2013) can be extended to configurations with simply supported lateral edges. Finally it is observed that shear effects are still relatively significant on the Ayrton-Perry criterion even if they are smaller than on the linearized critical buckling load derived in Chapter 3. We recall here that we ignore in this chapter imperfections due to residual stress in the CLT after manufacturing process. These imperfections could be included in the equivalent initial straightness imperfection.

Besides initial imperfections of timber elements, viscoelastic effects must be considered. These effects are recalled by Bažant and Cedolin (1991): additional creep deformations are observed. Since the relationship between deflection and compressive load is not linear, the problem is different from a beam under bending: creep deflections are not proportional to the creep factor. Then, in the following chapter, viscoelastic effects of wood are introduced to study the behavior of a timber column under compression at long term.

---

## Long-term buckling of CLT columns

*In the previous chapter, the elastic behavior of a column with initial imperfections under compression was investigated. Nevertheless, timber is a viscoelastic material and additional creep deformations must be added to these initial imperfections. First, in Section 5.1, a review is presented on the viscoelastic behavior of wood under constant or varying climate and in different loading directions. Then, in Section 5.3, a brief recall on the viscoelastic behavior of a timber column already studied by Bažant and Cedolin (1991) among others is done using the Euler beam model. This study is extended to the viscoelastic behavior of a Timoshenko column with both bending and shear creep in Section 5.4. Finally, in Section 5.5, the influence of the creep, particularly the shear creep, on the long term Ayrton-Perry criterion is studied.*

### 5.1 Wood: a viscoelastic material

Wood is a time-dependent material. This phenomenon was first characterized during the 18th century by Buffon (1741) from three-point bending tests. Particularly, he observed that time to failure, *i.e.* the time until failure under a constant loading, depends on the imposed load. From his observations, he recommended not to load permanent wooden structure above half of the initial strength and not to load short-lived structure above two third of the strength. As detailed in the following, the time-dependent behavior of wood is complex.

#### 5.1.1 Viscoelastic behavior of wood in longitudinal direction

Viscoelasticity is a mechanical characteristic of materials combining elasticity and viscosity resulting in an evolution of the relationship between strains and stress during time. Two types of tests are used to measure this property: creep tests and relaxation tests.

## 5.1. WOOD: A VISCOELASTIC MATERIAL

A creep test consists in an increase of deformation under constant stress (Figure 5.1). At time  $t_0$ , the stress is set to  $\sigma_0$  and is then kept constant until time  $t_1$ . At  $t_0$ , instantaneous linear deformations  $\varepsilon_0$  are due to the load  $\sigma_0$ . Then, between time  $t_0$  and time  $t_1$ , deformations increase because of the viscoelastic behavior. Additional deformations  $\varepsilon_c(t)$  are called creep deformations and depend on the intensity and the duration of the load. Then, after unloading at  $t_1$ , an instantaneous elastic recovery  $\varepsilon_1$  is observed. It was observed by Nakai and Grossman (1983) that  $\varepsilon_1 = \varepsilon_0$  for wood for weak loads. Then after time  $t_1$ , there is a recovery of deformations  $\varepsilon_r$  due to the viscoelastic behavior which is not always total: residual plastic deformations  $\varepsilon_p$  can remain even at long term.

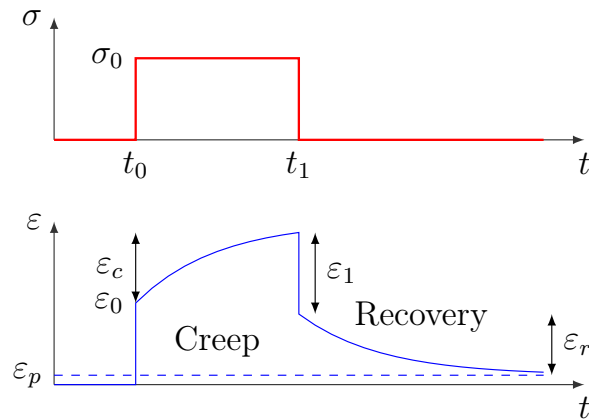


Figure 5.1 – Creep-recovery test principle

The relaxation test is the dual of the creep test: it consists in a decrease of stress under constant strain. Although an equivalence between creep and relaxation have been demonstrated by Grossman and Kingston (1954) for wood, only few studies have been led using relaxation tests since they are generally more complex to set up and since creep tests are more representative of the actual stress state in timber structures.

Numerous studies on the creep behavior of wood have been conducted and have been well reviewed by Schniewind and Barrett (1972) then Holzer et al. (2007) and Montero (2010) and main observations are briefly recalled here. The viscoelastic behavior of wood is often represented by the creep function  $J(t, t_0, \sigma_0) = \frac{\varepsilon(t)}{\sigma_0}$ .

In a creep test, three different phases are generally observed (Figure 5.2). The primary creep is a short phase at the beginning of the experiment. During this step, the creep rate is high and decreases progressively. During secondary creep, the creep rate is almost constant. This stage is generally very long and is the most studied phase. The tertiary creep is the final phase consisting in an acceleration of creep until failure. The time of each phases depends strongly on the stress level; particularly the secondary creep. That is why relatively low stress are imposed during creep tests in order to avoid

failure.

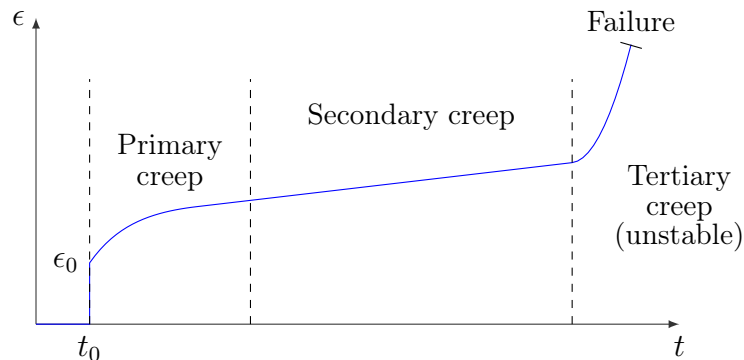


Figure 5.2 – Experimental setup

For a linear viscoelastic material, considering  $\varepsilon_1(t)$  and  $\varepsilon_2(t)$  as total deformations due to constant stress  $\sigma_1$  and  $\sigma_2$ , viscoelastic deformations due to the linear combination of stress  $\lambda_1\sigma_1 + \lambda_2\sigma_2$  are assumed equal to the linear combination of corresponding deformations  $\lambda_1\varepsilon_1(t) + \lambda_2\varepsilon_2(t)$ . Thus for a linear viscoelastic material,  $J(t, t_0, \sigma_0) = J(t, t_0)$ . Schniewind and Barrett (1972) reviewed several studies where a linear viscoelastic behavior were observed for wood at moderate load lower than 40% or 50% of the initial strength.

Boltzmann superposition principle stipulate that, for linear viscoelastic behavior, the superposition of loads during times implies the superposition of the corresponding response. This principle is particularly usefull for intermittent loading. Nakai and Grossman (1983) validate experimentally this principle for wood at moderate load.

An aging material is a material whose behavior depends on the time  $t_0$  at which it is loaded. For example, concrete is an aging material since its properties change during curing. Generally, in creep studies, wood is assumed to be a non-aging material:  $J(t, t_0) = J(t - t_0)$ .

Gressel (1984) studied creep behavior of wood from 10-years bending tests on three different species at 20° C and 65% of the relative humidity. After 10 years, he observed additional creep deformations between 0.3 and 0.7 of the initial deflection. Then, using a power creep law, he estimated additional creep deformations between 0.4 and 1.0 of the initial deflection after 100 years. Navi and Heger (2005) compared several creep studies on wood (Cariou, 1987; Hayashi et al., 1993; Le Govic et al., 1988; Nielsen, 1984) from bending or tensile tests, several stress levels, and different climate. More detailed reviews can be found in (Schniewind and Barrett, 1972; Holzer et al., 2007; Navi and Heger, 2005). Results are highly dependant on species and climate conditions.

### 5.1.2 Influence of climate conditions

Gerhards (2007) presented a detailed review on the temperature and moisture effects on linear elastic wood behavior. Particularly, the modulus of elasticity decreases with an increase of moisture content below fiber saturation and with an increase of temperature. Besides, the creep behavior of wood is also strongly influenced by climate conditions.

First, at constant moisture content, creep is faster for test at high temperature than for test at low temperature. The Time-Temperature Superposition Principle (TTSP) states that a function links two creep curves at different room temperature. In a diagram with a logarithmic scale for time  $t$ , this function correspond to a shift of the creep curve along log-time axis which is linked to the difference of temperature between the two tests. As noted by Holzer et al. (2007), the TTSP is very usefull to obtain long-time creep curve at normal temperature from short-time creep tests at high temperature which is also called accelerated creep. This principle has been widely used to determine the viscoelastic behavior of polymers. Nevertheless, the application of the TTSP for wood has not been fully established. Goldsmith and Grossman (1967) stated that: "Short term tests at higher temperatures cannot replace long-term tests at normal temperatures". Thus, as suggested by Davidson (1962), the TTSP "must be used with caution" for wood. Indeed, wood is a complex material made of several different polymers such as cellulose fibers, hemicellulose and lignin. Thus, even if multiparabolic models have been also suggested and used for the viscoelastic behavior of green wood (Bardet and Gril, 2002), it is preferable to make longer tests at constant climate corresponding to the service class defined in the Eurocode 5 (European Committee for Standardisation, 1993).

Wood viscoelastic behavior is also strongly influenced by relative humidity. First, as observed by Matar (2003), the creep behavior depends on the moisture content in the specimen. Similarly to temperature, this effect is very complex and difficult to model. Second, cyclic variations of relative humidity lead to additional deformations due to mechanosorptive effects during sorption and desorption. Several studies have been performed on this effect reviewed by Mårtensson (1994). Nevertheless, the impact of relative humidity is limited on CLT since they are very thick and only a small part of CLT is subjected to variation of moisture content. Moreover, CLT are slightly subjected to moisture variations in structures because of insulation and the rather large thickness of the panels.

From these studies, creep deformations are taken into account in the Eurocode 5 (European Committee for Standardisation, 1993) with the creep factor  $k_{\text{def}}$  by considering creep deformations after 50 years. This creep factor depends on the service class:  $k_{\text{def}}$  is equal to 0.6 in service class 1 for moisture content lower than 13%, and to 0.8 for moisture content between 13% and 20% for solid timber. Nonetheless, this creep factor is higher for plywood since the creep behavior of wood is not identical in all directions.

### 5.1.3 Orthotropic creep

The studies on the viscoelastic behavior of wood reviewed previously were focused on the longitudinal stiffness  $E_L$ . Nonetheless, wood presents an orthotropic behavior with a strong stiffness contrast between longitudinal direction and radial and tangential directions. From tensile and shear creep tests on Douglas-fir, Schniewind and Barrett (1972) studied the orthotropic viscoelastic behavior of wood. First, they observed that creep in radial  $R$  and tangential  $T$  directions is almost eight times larger than the creep in longitudinal direction after 1000 minutes corresponding to the primary creep. Second, they observed that the shear creep in longitudinal-tangential plane is between 4 and 5 times larger than the longitudinal tensile creep. From these observations, each parameter should be considered individually.

Currently, in the Eurocode 5 (European Committee for Standardisation, 1993), only one creep parameter  $k_{\text{def}}$  is defined for wood based material. The orthotropic viscoelastic behavior is considered for the design of plywood with a higher creep factor  $k_{\text{def}}$ : 0.8 in service class 1, and 1.0 in service class 2. Using only one creep parameter for plywood is admissible since an homogeneous equivalent behavior can be assumed because of the layers are thin compared to the thickness of the panel. Nonetheless, this is not admissible for CLT panels. Moreover, the effects of orthotropic viscoelastic behavior depends on the configurations of CLT, i.e. on the number and on the relative thickness of layers.

In order to estimate the creep behavior of CLT in bending, two additional parameters must be included in calculations: the longitudinal-radial shear stiffness  $G_{LC}$  and the cross-layer shear stiffness  $G_{CZ}$ . Thus, the creep behavior of CLT in bending is more complex than the one of solid timber. Only few studies on the creep behavior of CLT have been conducted (Jöbstl and Schickhofer, 2007; Colling, 2014; Pirvu and Karabeyli, 2014). Jöbstl and Schickhofer (2007) compared the creep behavior of glue-laminated timber (GLT) and of CLT from four-point bending tests during during one year. They observed that the relative creep of 5-ply CLT is 39% to 47% higher than GLT after one year. To go further, they calculate the shear creep of the cross-layer specifically in order to extend their results to all CLT configurations. Thus, they separated in their calculation the bending deflection and the shear deflection. They also separate the shear effects of longitudinal layers and of cross layers. Nevertheless, since they only measured the mid-span deflection, they were not able to measure directly the bending deflection and the shear deflection as well as the delayed shear stiffness of each layer. To complete the required data, they used recommendations. First they assumed that the contribution of cross-layers to bending stiffness is negligible which is a common assumption in CLT. Then, they assumed that the longitudinal bending creep factor and the shear creep factor of longitudinal layers are similar according to standards. Nevertheless, Schniewind and Barrett (1972) observed that this assumption seems not true. Finally, they assumed an elastic cross-layer shear stiffness  $G_{CZ}$  of 50 and 60 MPa. These assumptions are very

## 5.2. DEFINITION OF THE PROBLEM

conservative compared to what is observed in literature from numerical study (Aicher and Dill-Langer, 2000; Jakobs et al., 2005), from analytical models and from experimental studies (Ehrhart et al., 2015; Franzoni et al., 2016a) where values up to 200 MPa were found depending on the sawing pattern of boards and on the narrow-edge gluing as observed in Chapters 1 and 2. As a consequence, very different cross-layer shear creep factors  $k_{\text{def},9090}$  were obtained depending on the initial  $G_{CZ}$  assumption. Moreover the global creep factor  $k_{\text{def},CLT}$  calculated depend on the slenderness if the bending creep factor  $k_{\text{def},E}$  is different from the shear creep factor  $k_{\text{def},G}$ . Thus, their conclusions are true only for the studied slenderness. Consequently, it seems important to characterize directly the longitudinal-layer shear creep factor  $k_{\text{def},090}$  and the cross-layer shear creep factor  $k_{\text{def},9090}$ .

In the following, the effects of the orthotropic creep of wood on the behavior of a viscoelastic column are studied. First, in Section 5.3, the viscoelastic behavior of a column with the Euler beam model under constant loading is recalled and the long term critical buckling load is derived. Moreover, equivalent long term imperfections are derived as the sum of initial imperfection and creep deflection. These long term imperfections are then injected in the Ayrton-Perry criterion instead of initial imperfections in order to derive a long term Ayrton-Perry formula. Then in Section 5.4, the problem is extended to the Timoshenko beam model by considering both bending and shear creep of the column but there is no distinction between the longitudinal-layer and the cross-layer shear creep since their difference has not been clearly established in literature. Finally, in Section 5.5, effects of the viscoelasticity of the column, particularly the shear creep and the long term strength, on the Ayrton-Perry formula and on the shear criterion are studied.

## 5.2 Definition of the problem

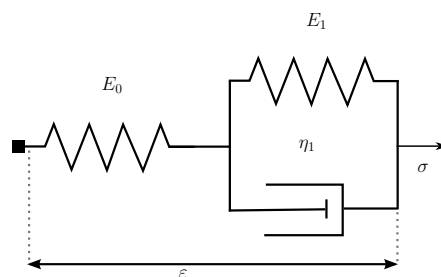


Figure 5.3 – Poynting-Thomson

Several models have been suggested to model the creep behavior of wood. Generally, in these models, it is assumed infinite deflections at long-term (Gressel, 1984).

Nonetheless, for the design, no long term criterion can be established using these models since the system is always unstable at long term. According to the Eurocode 5, structures are designed for a lifetime of at least 50 years. Hence, the long-term stability may be seen as equivalent to assume the stability after fifty years and an assumption of finite deflections at long term is made. Thus, only the final deflection is important to conclude on the long-term stability of the column. The simplest creep model which assumes long term finite deformations is the Poynting-Thomson model (Figure 5.3) composed of linear elastic spring corresponding to elastic deformation and a Kelvin-Voigt model corresponding to creep deformations. Two elementary models are used here:

- the linear spring which models the elasticity  $E$  of the material:  $\sigma = E\varepsilon$
- the linear dash-pot which models the viscosity  $\eta$  of the material:  $\sigma = \eta \frac{d\varepsilon}{dt}$  where  $t$  stands for time.

The differential equation corresponding to the Poynting-Thomson model (Figure 5.3) in a given direction writes as:

$$\sigma + \frac{\eta_1}{E_0 + E_1} \frac{d\sigma}{dt} = \frac{E_0 E_1}{E_0 + E_1} \varepsilon + \frac{E_0 \eta_1}{E_0 + E_1} \frac{d\varepsilon}{dt} \quad (5.1)$$

where  $\sigma$  and  $\varepsilon$  are stress and strain. By noting  $E_\infty = \frac{E_0 E_1}{E_0 + E_1}$  as the long term stiffness and  $t_E = \frac{\eta_1}{E_1}$  the characteristic time of the model, the differential equation (5.1) can be rewritten as:

$$\sigma + t_E \frac{E_\infty}{E_0} \frac{d\sigma}{dt} = E_\infty \varepsilon + t_E E_\infty \frac{d\varepsilon}{dt}$$

For wood, the viscoelastic behavior of the nine components of the orthotropic law should be considered. Nonetheless, their impact is complex on the CLT viscoelastic behavior because of its heterogeneities. Indeed, the viscoelastic behaviors of each component are mixed in the global bending and shear behavior of the CLT. Hence, in order to simplify the problem, we assume here that the global bending and shear viscoelastic behaviors of the CLT are homogeneous and are modeled by two Poynting-Thomson models replacing the constitutive equations (4.6):

$$\left\{ \begin{array}{l} M + t_D \frac{D_\infty}{D_0} \frac{dM}{dt} = D_\infty \chi + t_D D_\infty \frac{d\chi}{dt} \end{array} \right. \quad (5.2a)$$

$$\left\{ \begin{array}{l} Q + t_F \frac{F_\infty}{F_0} \frac{dQ}{dt} = F_\infty \gamma + t_F F_\infty \frac{d\gamma}{dt} \end{array} \right. \quad (5.2b)$$

### 5.3. LONG TERM BUCKLING OF AN IMPERFECT EULER COLUMN

where  $M(x, t)$  and  $Q(x, t)$  are the bending moment and the shear force defined as:

$$\begin{cases} M(x, t) = - \int_{-\frac{h}{2}}^{\frac{h}{2}} bz\sigma_{xx}(x, z, t)dz, & (5.3a) \\ Q(x, t) = \int_{-\frac{h}{2}}^{\frac{h}{2}} b\sigma_{xz}(x, z, t)dz. & (5.3b) \end{cases}$$

$\sigma_{xx}$  and  $\sigma_{xz}$  are the longitudinal and the shear stress.  $D_0$  (4.5a) and  $F_0$  (4.5b) are the initial bending and shear stiffness.  $D_\infty$  and  $F_\infty$  are the long term bending and shear stiffness and  $t_D$  and  $t_F$  are the characteristic time of the bending and shear creep models respectively.  $\chi$  and  $\gamma$  are the curvature and the global shear strain of the beam which comply with compatibility equations:

$$\begin{cases} \chi(x, t) = \varphi'(x, t), & (5.4a) \\ \gamma(x, t) = \varphi(x, t) + (f'(x, t) - f'_0(x)). & (5.4b) \end{cases}$$

where  $\varphi$  and  $f$  are the rotation and the total deflection of the beam.  $\bullet' = \frac{d\bullet}{dx}$  is the derivative of the parameter  $\bullet$  according to  $x$  direction.  $f_0(x)$  is the initial imperfection (Figure 5.4) defined as:

$$f_0(x) = w_{0,eq} \sin \frac{\pi x}{l} \quad (5.5)$$

Finally, the equilibrium at time  $t$  of the column under the constant compressive load  $P$  writes as:

$$\begin{cases} Q(x, t) = M'(x, t) & (5.6a) \\ M(x, t) = Pf(x, t) & (5.6b) \end{cases}$$

## 5.3 Long term buckling of an imperfect Euler column

First, the resolution of problem of a viscoelastic column under compression is recalled using the Euler beam model (Bažant and Cedolin (1991)). Accordingly we assume here that the initial and the long term shear compliances are zero:  $\frac{1}{F_\infty} = \frac{1}{F_0} = 0$ . From the viscoelastic constitutive equation (5.2b), the global shear strain  $\gamma$  is negligible compared to  $f'$  and to  $\varphi$  in (5.4b):

$$f'(x, t) - f'_0(x) = -\varphi(x, t) \quad (5.7)$$

Then by replacing the curvature  $\chi = f''_0 - f''$  (5.4a,5.7) and considering the equilibrium (5.6b) and the initial deflection  $f_0$  (5.5) in the bending viscoelastic constitutive equation

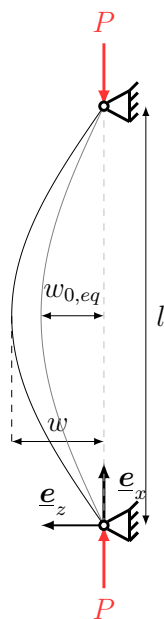


Figure 5.4 – Viscoelastic column with initial imperfection under compression

(5.2a) leads to a differential equation in  $f(x, t)$ :

$$Pf + t_D \frac{P_{E,\infty}}{P_{E,0}} P \frac{df}{dt} + D_\infty f'' + t_D D_\infty \frac{df''}{dt} = D_\infty f_0'' = -P_{E,\infty} w_{0,eq} \sin\left(\frac{\pi x}{l}\right) \quad (5.8)$$

The solution  $f$  of this problem is of the form:

$$f(x, t) = w(t) \sin\left(\frac{\pi x}{l}\right)$$

where  $w(t)$  is the total mid-span deflection at time  $t$ . The differential equation (5.8) can then be rewritten as differential equation of  $w(t)$  only:

$$t_D \left(1 - \frac{P}{P_{E,0}}\right) \frac{dw}{dt} + \left(1 - \frac{P}{P_{E,\infty}}\right) w = w_{0,eq} \quad (5.9)$$

where  $P_{E,0} = D_0 \frac{\pi^2}{l^2}$  and  $P_{E,\infty} = D_\infty \frac{\pi^2}{l^2}$  are the short term and long term Eulerian critical buckling load. At  $t = 0$ , the total deflection is equal to instantaneous deflection (4.15):

$$w(0) = \frac{1}{1 - \frac{P}{P_{E,0}}}$$

### 5.3. LONG TERM BUCKLING OF AN IMPERFECT EULER COLUMN

The solution of this problem is:

$$w(t) = \frac{w_{0,eq}}{1 - \frac{P}{P_{E,\infty}}} \left( 1 + \left( \frac{t_E}{\tau} - 1 \right) \exp^{-\frac{t}{\tau}} \right) \quad (5.10)$$

where  $\tau$  is the characteristic time of the creep deflections:

$$\tau = t_E \frac{1 - \frac{P}{P_{E,0}}}{1 - \frac{P}{P_{E,\infty}}}$$

We note here that, contrary to creep deflections of a beam under bending,  $\tau \neq t_E$  because of the non-linearity of the problem.

The mid-span deflection  $w(t)$  is finite at long term only if  $\tau > 0$ . Granted that the stability criterion at short term  $P < P_{E,0}$  is satisfied,  $w(t)$  is finite at long term only if  $P < P_{E,\infty}$  which corresponds to a long term stability criterion. Thus  $P < P_{E,\infty}$ , the long term deflection  $w_\infty$  is:

$$w_\infty = \frac{w_{0,eq}}{1 - \frac{P}{P_{E,\infty}}} \quad (5.11)$$

This long term deflection  $w_\infty$  is a combination of initial imperfection  $w_{0,eq}$  of elastic deflection  $w_{el}$  and of creep deflection  $w_\varphi$ :

$$w_\infty = w_{0,eq} + w_{el,\infty} + w_\varphi \quad (5.12)$$

By defining the long term imperfections as  $w_{0,eq}^\infty = w_{0,eq} + w_\varphi$ , the expression of the maximum shear stress  $\sigma_{max,\infty}$  at long term is expressed similarly to  $\sigma_{max}$  (4.18) by replacing  $w_{0,eq}$  by  $w_{0,eq}^\infty$ . In order to derive the expression of  $w_{0,eq}^\infty$ , we recall the expression of the of the long term elastic deflection  $w_{el,\infty}$  (4.16) by replacing initial imperfections by long term imperfections:

$$w_{el,\infty} = \frac{w_{0,eq} + w_\varphi}{\frac{P_{E,0}}{P} - 1}$$

Then, from this expression and expressions of the long term deflection (5.11,5.12), the equivalent long term imperfection  $w_{0,eq}^\infty$  is derived as:

$$w_{0,eq}^\infty = w_{0,eq} \frac{1 - \frac{P}{P_{E,0}}}{1 - \frac{P}{P_{E,\infty}}} = w_{0,eq} \frac{\tau}{t_E}$$

Then, it is observed that replacing  $w_{0,eq}$  by  $w_{0,eq}^\infty$  in the expression of the bending stress (4.18) is equivalent to replace the critical buckling load  $P_{cr,0}$ , which is equivalent to  $P_{E,0}$  in the Euler beam model, by the long term critical buckling load  $P_{E,\infty}$ .

Then a long term strength criterion can be suggested for a permanent load  $P$ :

$$\frac{P}{\sigma_c S_{\text{eff}}} < \frac{1}{0.5(1 + \omega + \lambda_{\text{rel},\infty}^2) + \sqrt{0.25(1 + \omega + \lambda_{\text{rel},\infty}^2)^2 - \lambda_{\text{rel},\infty}^2}} = \bar{N}_{\text{AP},\infty} = \bar{N}_{\text{AP},\infty} \quad (5.13)$$

where  $\lambda_{\text{rel},\infty}$  is the long term relative slenderness defined as:

$$\lambda_{\text{rel},\infty} = \sqrt{\frac{P_{u,\infty}}{P_{E,\infty}}}$$

where  $P_{u,\infty}$  is the long term ultimate compressive load associated to the long term ultimate compressive strength  $\sigma_{u,\infty}$ .

## 5.4 Viscoelastic behavior of a column with the Timoshenko beam model under constant loading

In this section, we extend the viscoelastic analysis to Timoshenko beam considering shear effects on the behavior. The viscoelastic behavior of both bending and shear are considered (5.2). Then, by considering both equilibrium (5.6) and the compatibility equations (5.4) a system with two differential equations is obtained as a function of the deflection  $f(x, t)$  and the shear strain  $\gamma(x, t)$ :

$$\begin{cases} Pf + t_D \frac{D_\infty}{D_0} P \frac{df}{dt} - D_\infty \gamma' + D_\infty f'' - t_D D_\infty \frac{d\gamma'}{dt} + t_D D_\infty \frac{df''}{dt} = -P_{E,\infty} & (5.14a) \\ F_\infty \gamma + t_F F_\infty \frac{d\gamma}{dt}(x, t) - P f' - t_F \frac{F_\infty}{F_0} P \frac{df'}{dt} = 0 & (5.14b) \end{cases}$$

Solutions of this problem have the form:

$$\begin{aligned} f(x, t) &= w(t) \sin\left(\frac{\pi x}{l}\right) \\ \gamma(x, t) &= \Gamma(t) \cos\left(\frac{\pi x}{l}\right) \end{aligned}$$

where  $w(t)$  and  $\Gamma(t)$  are the mid-span deflection and the shear strain at support  $x = 0$  at time  $t$ . By injecting these solutions in the differential equations 5.14, a system of two

5.4. VISCOELASTIC BEHAVIOR OF A COLUMN WITH THE TIMOSHENKO BEAM MODEL UNDER CONSTANT LOADING

differential equations of  $w(t)$  and  $\Gamma(t)$  only is obtained:

$$\left\{ \begin{array}{l} t_D \left( 1 - \frac{P}{P_{E,0}} \right) \frac{dw}{dt} + \left( 1 - \frac{P}{P_{E,\infty}} \right) w - \frac{l}{\pi} \left( \Gamma - t_D \frac{d\Gamma}{dt} \right) = w_{0,eq} \end{array} \right. \quad (5.15a)$$

$$\left\{ \begin{array}{l} t_F \frac{P}{F_0} \frac{dw}{dt} + \frac{P}{F_\infty} w - \frac{l}{\pi} \left( \Gamma - t_F \frac{d\Gamma}{dt} \right) = 0 \end{array} \right. \quad (5.15b)$$

We define the vector  $\underline{\mathbf{X}}(t)$  as:

$$\underline{\mathbf{X}}(t) = \begin{pmatrix} w(t) \\ \frac{l}{\pi} \Gamma(t) \end{pmatrix}$$

The problem (5.15) can then be written as a differential equation on  $\underline{\mathbf{X}}(t)$  only:

$$\left( 1 - \frac{P}{P_{cr,0}} \right) \frac{d\underline{\mathbf{X}}}{dt}(t) + \underline{\mathbf{A}} \cdot \underline{\mathbf{X}}(t) = \frac{w_{0,eq}}{t_D} \underline{\mathbf{B}} \begin{pmatrix} 1 \\ \frac{P}{F_0} \end{pmatrix} \quad (5.16)$$

where

$$\underline{\mathbf{A}} = \begin{pmatrix} \frac{1}{t_D} \left( 1 - \frac{P}{P_{E,\infty}} \right) - \frac{1}{t_F} \frac{P}{F_\infty} & \frac{1}{t_F} - \frac{1}{t_D} \\ \frac{1}{t_D} \frac{P}{F_0} \left( 1 - \frac{P}{P_{E,\infty}} \right) - \frac{1}{t_F} \frac{P}{F_\infty} \left( 1 - \frac{P}{P_{E,0}} \right) & \frac{1}{t_F} \left( 1 - \frac{P}{P_{E,0}} \right) - \frac{1}{t_D} \frac{P}{F_0} \end{pmatrix}$$

The characteristic polynomial of the matrix  $\underline{\mathbf{A}}$  is given by:

$$\begin{aligned} \det(\underline{\mathbf{A}} - \lambda \underline{\mathbf{I}}) &= \lambda^2 - \lambda \left[ \frac{1}{t_D} \left( 1 - \frac{P}{P_{cr,E,\infty}} \right) + \frac{1}{t_F} \left( 1 - \frac{P}{P_{cr,G,\infty}} \right) \right] + \frac{1}{t_D t_F} \left( 1 - \frac{P}{P_{cr,0}} \right) \left( 1 - \frac{P}{P_{cr,\infty}} \right) \\ &= \lambda^2 - b\lambda + c \end{aligned}$$

where  $-b$  and  $c$  are coefficients of the polynomial.  $P_{cr,E,\infty}$  and  $P_{cr,G,\infty}$  are long term critical buckling when considering only the bending creep or the shear creep respectively:

$$\frac{1}{P_{cr,E,\infty}} = \frac{1}{P_{E,\infty}} + \frac{1}{F_0} \quad \text{and} \quad \frac{1}{P_{cr,G,\infty}} = \frac{1}{P_{E,0}} + \frac{1}{F_\infty}$$

$P_{cr,\infty}$  is the long term critical buckling load defined as:

$$\frac{1}{P_{cr,\infty}} = \frac{1}{P_{E,\infty}} + \frac{1}{F_\infty}$$

It is observed that the discriminant  $\Delta = b^2 - 4c$  is always positive since it can be

written as a sum of positive terms:

$$\Delta = \frac{1}{t_D^2} \left(1 - \frac{P}{P_{cr,E,\infty}}\right)^2 + \frac{1}{t_F^2} \left(1 - \frac{P}{P_{cr,G,\infty}}\right)^2 + \frac{P^2}{t_D t_F} \left(\frac{1}{F_\infty} - \frac{1}{F_0}\right) \left(\frac{1}{P_{E,\infty}} - \frac{1}{P_{E,0}}\right)$$

Then the two roots are real numbers. Solutions of the equation (5.16) are then given by:

$$\underline{\mathbf{X}}(t) = \underline{\mathbf{X}}_1 \exp^{-\lambda_1 t} + \underline{\mathbf{X}}_2 \exp^{-\lambda_2 t} + \underline{\mathbf{X}}_3$$

where  $\underline{\mathbf{X}}_1$  and  $\underline{\mathbf{X}}_2$  are eigenvectors of  $\underline{\mathbf{A}}$  associated to roots  $\lambda_1$  and  $\lambda_2$  and  $\underline{\mathbf{X}}_3$  is a constant vector.  $\underline{\mathbf{X}}(t)$  is finite at long term only if both roots  $\lambda_1$  and  $\lambda_2$  are positive. Then, the column is stable at long term only if  $b < 0$  and  $c > 0$  which is equivalent to the following criteria:

$$\begin{cases} \frac{1}{P} > \frac{1}{t_D + t_F} \left(\frac{t_F}{P_{cr,E,\infty}} + \frac{t_D}{P_{cr,G,\infty}}\right) & (5.17a) \\ P < P_{cr,\infty} & (5.17b) \end{cases}$$

We note that, since  $P_{cr,\infty} < P_{cr,E,\infty}$  and  $P_{cr,\infty} < P_{cr,G,\infty}$ , the criterion (5.17a) is always true given that the criterion (5.17b) is fulfilled.

Here we are only interested on the long term deformation  $\underline{\mathbf{X}}_3$ . Provided that the stability criterion (5.17b) is fulfilled, long term deformation  $\underline{\mathbf{X}}_3$  are derived from the equilibrium equation (5.16):

$$\underline{\mathbf{X}}_3 = \begin{pmatrix} w_\infty \\ \frac{l}{\pi} \Gamma_\infty \end{pmatrix} = w_{0,eq} \frac{1}{1 - \frac{P}{P_{cr,\infty}}} \begin{pmatrix} 1 \\ \frac{P}{F_\infty} \end{pmatrix}$$

We demonstrated here that the expression of the long term deflection  $w_\infty$  is similar to what is observed with the Euler beam model while changing the critical buckling load. As a consequence, the long term strength criterion (5.13) can be adapted to Timoshenko beam by replacing the long term buckling load  $P_{E,\infty}$  by  $P_{cr,\infty}$ . Moreover, it is observed that long term shear strain  $\Gamma_\infty$  is also similar to the expression of the short term shear strain (4.17) while changing the critical buckling load and the shear stiffness. Then the proposed shear criterion can also be adapted at long term by replacing the critical buckling load:

$$\frac{P}{P_{u,\infty}} < \frac{1}{\frac{\pi w_{0,eq}}{l} \frac{P_{u,\infty}}{Q_{u,\infty}} + \lambda_{rel,\infty}^2} = \bar{N}_{\tau,\infty} \quad (5.18)$$

## 5.5 Influence of the orthotropic viscoelastic behavior on the Ayrton-Perry criterion

In this section, the long term Ayrton-Perry criterion and the proposed shear criterion are plotted for different orthotropic viscoelastic behavior of CLT1 and CLT2 (Table 4.1). Particularly, the influence of the creep factor  $k_{\text{def}}$ . Moreover, the duration of load effect on the residual strength of CLT has been studied by Shiro et al. (2014) and Pirvu and Karacabeyli (2014) which observed that the variation of the bending strength of CLT is almost similar to what is observed for solid timber. Nonetheless, the variation of the rolling-shear strength has not been studied to the other knowledge and could be different to what is observed for bending. That is why we suggest to observe the influence of the modification factor  $k_{\text{mod}}$ . In the Eurocode 5 European Committee for Standardisation (1993), only one  $k_{\text{def}}$  and one  $k_{\text{mod}}$  are suggested corresponding to the long term behavior of the timber in the longitudinal direction. The use of only one creep factor and one modification factor for both bending and shear viscoelastic behavior in expression of the long term Ayrton Perry criterion 5.13 and of the long term shear criterion 5.18 will result in approximately the same results as observed at short term since relative shear effects are approximately identical. Nonetheless, because of its configuration and of the orthotropic behavior of wood, a distinction between the long term bending and the long term shear behaviors seems necessary for CLT.

### 5.5.1 Viscoelastic behavior with two creep factors $k_{\text{def},D}$ and $k_{\text{def},F}$

First, we assume that the bending creep behavior and the shear creep behavior are different and we introduce the bending creep factor  $k_{\text{def},D}$  and the shear creep factor  $k_{\text{def},F}$ . The critical buckling load at long term  $P_{cr,\infty}$  is then:

$$\frac{1}{P_{cr,\infty}} = \frac{1 + k_{\text{def},D}}{P_{E,0}} + \frac{1 + k_{\text{def},F}}{F_0}$$

Only one modification factor  $k_{\text{mod}} = 0.6$  corresponding to the service class 1 for a permanent loading. is used in the following to observe only the impact of  $k_{\text{def},F}$ . In Figures 5.5 and 5.6, long term Ayrton-Perry formula and shear criterion are plotted as a function of the slenderness  $\frac{l}{h}$  for  $k_{\text{def},D} = 0.6$  (Service class 1) and for  $k_{\text{def},F} = 2k_{\text{def},D}$ . Considering the lack of knowledge regarding the rolling shear creep and the various values in the literature mentioned in Section 5.1, this choice may be optimistic.

As expected, shear effects are amplified compared to a model with only one creep factor  $k_{\text{def}}$ . Particularly, for a small initial imperfection  $w_0 = \frac{l}{500}$  the relative difference between the Ayrton-Perry criterion with the Euler and the Timoshenko beam models is large up to 14.5%. Moreover it is noted that, for  $w_0 = \frac{l}{100}$ , the shear criterion is lower than the Ayrton-Perry criterion for a slenderness  $\frac{l}{h} \leq 15$  and for a low cross-layer shear

stiffness similarly to what was observed at short term.

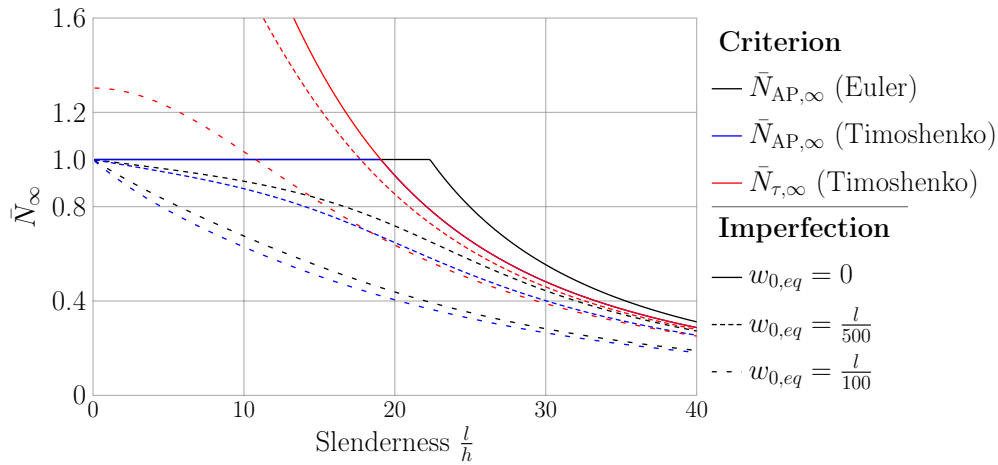


Figure 5.5 – Ayrton-Perry formula and shear criterion at long-term with two creep factors  $k_{\text{def},D}$  and  $k_{\text{def},F}$  for configuration CLT1

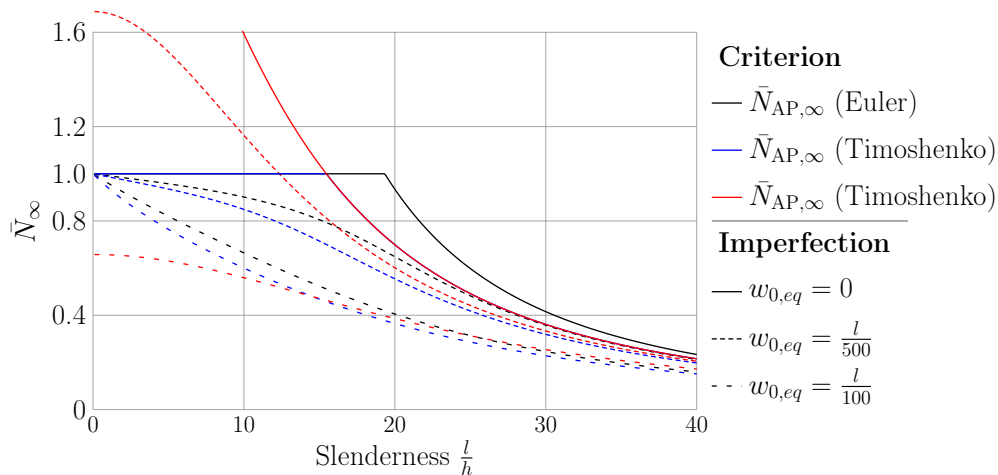


Figure 5.6 – Ayrton-Perry formula and shear criterion at long-term with two creep factors  $k_{\text{def},D}$  and  $k_{\text{def},F}$  for configuration CLT2

From these results it is observed that the shear creep factor  $k_{\text{def},F}$  has mainly an impact on the Ayrton-Perry criterion since it decreases the long term buckling load. Nonetheless, it has only a limited impact on the relevance of shear criterion compared to the Ayrton-Perry criterion. Additionally, the influence of  $k_{\text{def},F}$  may be stronger as observed in (Jöbstl and Schickhofer, 2007).

## 5.6. CONCLUSION

### 5.5.2 Viscoelastic behavior with two modification factors $k_{\text{mod},D}$ and $k_{\text{mod},F}$

Second, in order to study the influence of a difference between variations of the bending and the shear strength of CLT, we introduce two modification factors: the bending modification factor  $k_{\text{mod},E}$  and the shear modification factor  $k_{\text{mod},G}$ . In order to study separately the effects of  $k_{\text{mod}}$  and  $k_{\text{def}}$ , we assume here that  $k_{\text{def},E} = k_{\text{def},G} = 0.6$ . In Figures 5.7 and 5.8, long term Ayrton-Perry formula and shear criterion are plotted as a function of the slenderness  $\frac{l}{h}$  for  $k_{\text{mod},E} = 0.6$  (Service class 1) and for  $k_{\text{mod},G} = 0.4$ . Similarly to what was observed for  $k_{\text{def},G}$ , there is not enough studies on the rolling shear strength to give a representative  $k_{\text{mod},G}$  and only its impact on the shear criterion is studied here.

In both Figures 5.7 and 5.8, a significant drop of  $\bar{N}_{\tau,\infty}$  is observed. Particularly, for slenderness up to  $\frac{l}{h} = 34$ ,  $\bar{N}_{\tau,\infty}$  is lower than  $\bar{N}_{\text{AP},\infty}$  which show the strong impact of  $k_{\text{mod},G}$  on the long term shear criterion.

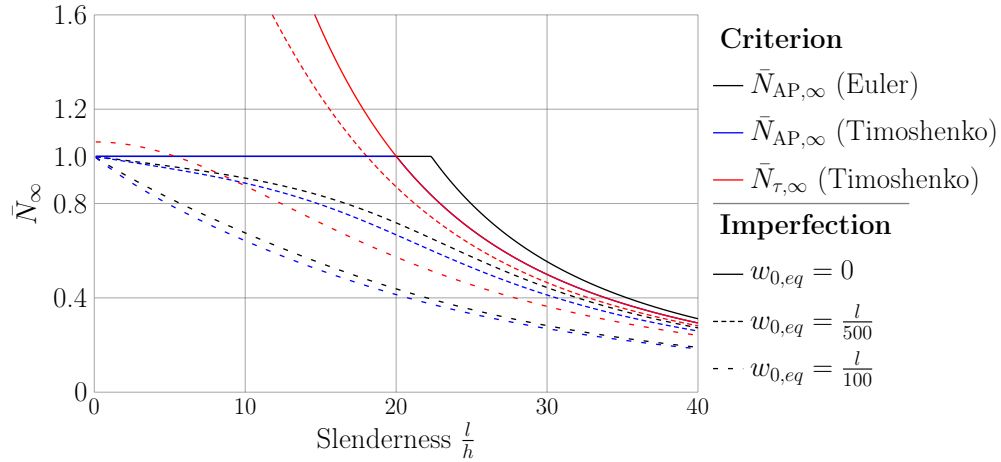


Figure 5.7 – Ayrton-Perry formula and shear criterion at long-term with two modification factors  $k_{\text{mod},D}$  and  $k_{\text{mod},F}$  for configuration CLT1

## 5.6 Conclusion

In this chapter, we extended the viscoelastic behavior of a column under compression to the Timoshenko beam model and we considered both bending and shear creep behaviors. We observed that shear effects are amplified at long term and confirmed that a new shear force criterion should be taken into account particularly for small cross-layer shear strength and when initial imperfections are large. The relevance of this shear criterion is due to the high contrast between the longitudinal compressive strength

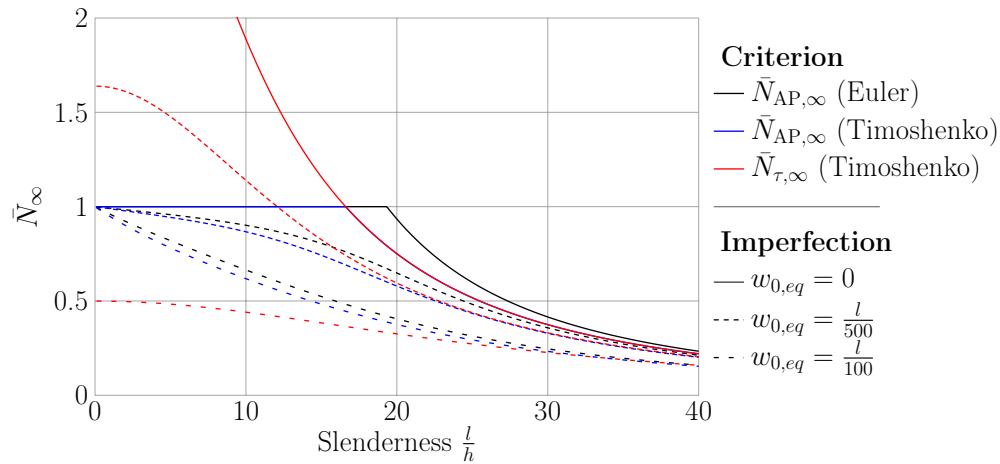


Figure 5.8 – Ayrton-Perry formula and shear criterion at long-term with two modification factors  $k_{mod,D}$  and  $k_{mod,F}$  for configuration CLT2

$\sigma_u$  and the rolling shear strength  $\tau_u$ . Further studies are then necessary on the rolling shear strength. For instance, the shear criterion may be particularly relevant for regularly spaced CLT walls (Franzoni et al., 2016a, 2017a) as well as heterogeneous CLT lay-ups with lower strength classes in cross-layers. Finally, the viscoelastic effects on the rolling shear strength and stiffness should be investigated. Such experimental campaigns are currently in progress using the four-point bending test on sandwich beam introduced in Chapter 2.

## 5.6. CONCLUSION

---



---

## General Conclusion

The aim of this thesis was to investigate the stability and the strength of CLT walls at short and long term. In this purpose, we first suggest closed-form bounds of the equivalent-layer stiffness from the local behavior of wood and the sawing pattern of the boards. Particularly it was observed that the equivalent cross-layer shear stiffness can be two to three times larger than the local rolling shear stiffness. It was also observed that, for most boards, these bounds are valid for both boards with and without narrow glued edges. In order to confirm these theoretical observations, an experimental study on the equivalent cross-layer shear stiffness is necessary. To this purpose, a new experimental protocol has been suggested: a four-point bending test on a sandwich beam with wooden core oriented in the tangential direction. The new method of measurement of the bending stiffness by the rotation at support seems more reliable than the classical measurement by the relative displacement in the area between loads since it averages mechanical properties over the whole span. Moreover, it was observed a reduced coefficient of variations of the equivalent cross-layer shear stiffness compared to the local rolling shear stiffness. Nonetheless, the experimental campaign done during this PhD thesis is not sufficient to conclude on the equivalent cross-layer shear stiffness. A much larger experimental campaign is then necessary where several parameters such as span, sawing pattern and dimensions of boards, wood species and narrow edge gluing.

In the second part of this dissertation, the buckling of CLT walls was investigated. First, it was observed that the critical buckling load is of the same order as the compressive strength of CLT walls particularly because of cross-layer shear effects. A suggested projection of the Bending-Gradient model provided accurate results compared to the 3D numerical study. Moreover, it was observed that the distinction between soft and hard simple support could be relevant. Since, the buckling of CLT walls was found relevant, initial imperfections was further considered to model a more realistic CLT wall. Classically, the Ayrton-Perry criterion is used to design columns and walls. It was shown that this criterion can be extended to plate models when considering simply supported lateral edges. Additionally, because of the low rolling shear strength, a new shear cri-

## *General Conclusion*

---

terion for CLT walls was suggested additionally to the Ayrton-Perry formula. It was shown that this criterion can be relevant particularly for small slenderness and when the design rolling shear strength is low. Finally, viscoelastic effects have been also considered. Especially, the bending and the shear creep have been considered separately. It was shown that the Ayrton-Perry criterion and the proposed shear criterion can be extended to constant loading at long term by replacing the initial critical buckling load by the long-term critical buckling load. It was shown that, because of the orthotropic viscoelastic behavior of wood, the shear criterion can be more relevant at long term than at short term. From this observation the study of the long-term cross-layer shear behavior is very important. Such experiment are currently in progress using the suggested four-point bending test on sandwich beam with a wooden core. Nonetheless, because of the lack of results and the duration of creep experiment, results of this experimental campaign have not been presented in this dissertation. However, this experimental protocol seems adapted to such study.

---

## Annexes

### A.1 The Timoshenko beam model

In this appendix, the Timoshenko beam model is recalled. We consider a simply supported rectangular beam with a length  $l$ , a width  $b$  and a thickness  $h$  corresponding to  $x$ ,  $y$  and  $z$  directions respectively (Figure 4.1). We assume that local mechanical properties are invariant according to  $x$  and  $y$  axis. The 3D displacement field  $\mathbf{u}(x, y, z)$  is then assumed invariant according to  $y$  axis as following:

$$\begin{cases} u_x(x, y, z) = \varphi(x)z & \text{(A.1a)} \\ u_y(x, y, z) = 0 & \text{(A.1b)} \\ u_z(x, y, z) = f(x) & \text{(A.1c)} \end{cases}$$

where  $f(x)$  is the deflection of the beam at the neutral axis and  $\varphi(x)$  is the rotation of the section (Figure A.2). The 3D strain field  $\varepsilon_{ij} = \frac{1}{2} \left( \frac{du_i}{dx_j} + \frac{du_j}{dx_i} \right)$  can then be expressed as a function of global kinematic fields  $f(x)$  and  $\varphi(x)$ :

$$\begin{cases} \varepsilon_{xx}(x, y, z) = \varphi'(x)z & \text{(A.2a)} \\ 2\varepsilon_{xz}(x, y, z) = \gamma_{xz}(x, y, z) = \varphi(x) + f'(x) & \text{(A.2b)} \\ \varepsilon_{yy} = \varepsilon_{zz} = \varepsilon_{xy} = \varepsilon_{yz} = 0 & \text{(A.2c)} \end{cases}$$

A constant local shear strain  $\gamma_{xz}$  is assumed over the section of the beam. Then, the global shear strain of the beam is identical to the local shear strain:  $\gamma = \gamma_{xz}$ .

We note  $E_0(z)$  the elastic Young modulus in  $x$  direction and  $G_0(z)$  the shear modulus between  $x$  and  $z$ . Assuming that the local 3D stress fields  $\sigma_{zz}$  and  $\sigma_{yy}$  are negligible compared to  $\sigma_{xx}$ ,  $\sigma_{xx}$  and  $\sigma_{xz}$  are expressed as:

$$\begin{cases} \sigma_{xx}(x, z) = E_0(z)\varepsilon_{xx}(x, z) & \text{(A.3a)} \\ \sigma_{xz}(x, z) = G_0(z)\gamma_{xz}(x, z) & \text{(A.3b)} \end{cases}$$

A.1. THE TIMOSHENKO BEAM MODEL

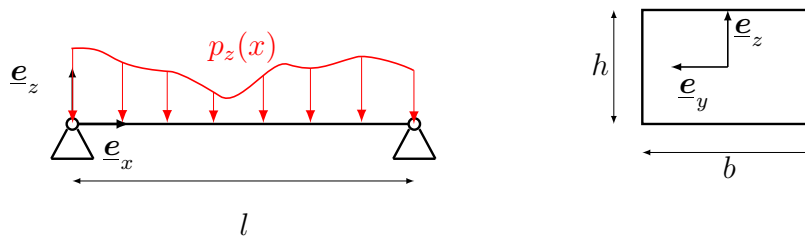


Figure A.1 – Scheme of a beam

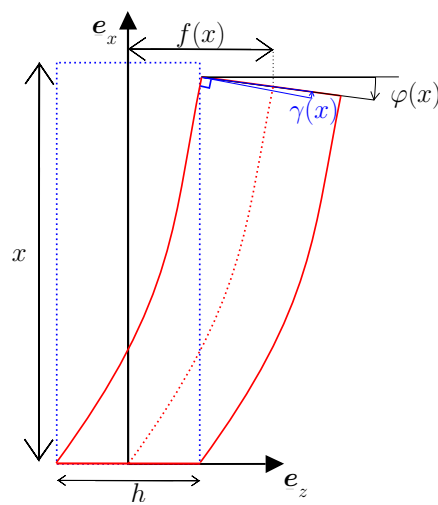


Figure A.2 – Definition of the deflection  $f(x)$ , of the rotation of the section  $\varphi(x)$  and of the global shear strain  $\gamma(x)$

## APPENDIX A. ANNEXES

---

The bending moment  $M(x)$  and the shear force  $Q(x)$  are defined as global stress fields as following:

$$\left\{ \begin{array}{l} M(x) = - \int_{-\frac{h}{2}}^{\frac{h}{2}} bz\sigma_{xx}(x, z)dz, \\ Q(x) = \int_{-\frac{h}{2}}^{\frac{h}{2}} b\sigma_{xz}(x, z)dz. \end{array} \right. \quad \begin{array}{l} \text{(A.4a)} \\ \text{(A.4b)} \end{array}$$

Then, by integrating the local 3D stress fields (A.3) over the section and considering the kinematic assumption (A.2), the bending moment  $M(x)$  and the shear force  $Q(x)$  are related to the rotation  $\varphi(x)$  and to the global shear strain  $\gamma(x) = \gamma_{xy}(x, y, z)$

$$\left\{ \begin{array}{l} M(x) = \varphi'(x) \int_{-\frac{h}{2}}^{\frac{h}{2}} bz^2 E_0(z)dz \\ Q(x) = \gamma(x) \int_{-\frac{h}{2}}^{\frac{h}{2}} bG_0(z)dz \end{array} \right. \quad \begin{array}{l} \text{(A.5a)} \\ \text{(A.5b)} \end{array}$$

The bending stiffness  $D_0$  and the shear stiffness  $F_0$  can then defined according to (A.5a) and (A.5a):

$$\left\{ \begin{array}{l} D_0 = \int_{-\frac{h}{2}}^{\frac{h}{2}} bz^2 E_0(z)dz, \\ F_0 = \int_{-\frac{h}{2}}^{\frac{h}{2}} bG_0(z)dz. \end{array} \right. \quad \begin{array}{l} \text{(A.6a)} \\ \text{(A.6b)} \end{array}$$

From the expression of the local stress  $\sigma_{xx}$  (A.3a), of the local strain (A.2a) and from the constitutive equation (A.5a), the stress  $\sigma_{xx}$  under bending can be derived:

$$\sigma_{xx}(x, z) = \frac{E_0(z)z}{D_0} M(x) \quad \text{(A.7)}$$

Finally, we introduce the the local stress equilibrium:

$$\left\{ \begin{array}{l} \frac{d\sigma_{xx}}{dx} + \frac{d\sigma_{xy}}{dy} + \frac{d\sigma_{xz}}{dz} = 0, \\ \frac{d\sigma_{xz}}{dx} + \frac{d\sigma_{yz}}{dy} + \frac{d\sigma_{zz}}{dz} = 0. \end{array} \right. \quad \begin{array}{l} \text{(A.8a)} \\ \text{(A.8b)} \end{array}$$

We assumed that the problem is invariant according to  $y$ , then the second term of each equation (A.8a,A.8b) vanishes. By integrating each equilibrium over the section, the

## A.1. THE TIMOSHENKO BEAM MODEL

global equilibrium of the beam is classically found:

$$\begin{cases} M'(x) = Q(x); & \text{(A.9a)} \\ Q'(x) + p_z(x) = 0. & \text{(A.9b)} \end{cases}$$

where  $p_z(x)$  is the external load in  $z$  direction (Figure A.1).

Nonetheless, it is observed that the expression of  $\sigma_{xz}$  (A.3b) is not statically compatible. First, at the upper and lower faces of the beam, for  $z = \pm \frac{h}{2}$ ,  $\sigma_{xz}$  does not comply with zero shear stress boundary conditions. Second, for multi-layer composite, there are discontinuities of the shear stress between two layers with different shear stiffness  $G_0$  and the shear stress (A.3b). Another expression for the shear stiffness  $F_0$  may be derived following the works of Jourawski (1856) particularly suitable for heterogeneous beam.

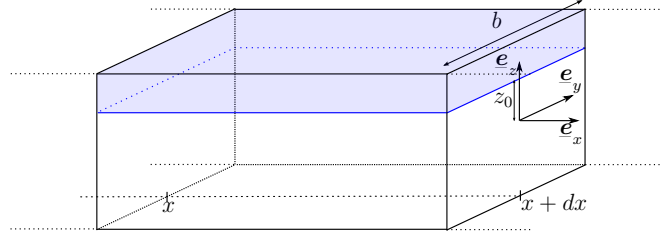


Figure A.3 – Scheme of an elementary part of the beam of length  $dx$

First, from the integration of the equilibrium (A.8a) between  $z = z_0$  and  $z = \frac{h}{2}$  (Figure A.3), and considering the boundary condition  $\sigma_{xz}(x, \frac{h}{2}) = 0$  it is obtained that:

$$\int_{z_0}^{\frac{h}{2}} \frac{d\sigma(x, z)}{dx} dz = \sigma_{xz}(x, z_0)$$

Then, from the expression of the stress  $\sigma_{xx}$  as a function of  $M(x)$  (A.7) and recalling the equilibrium (A.9a), the shear stress  $\sigma_{xz}(x, z_0)$  can be expressed as:

$$\sigma_{xz}(x, z_0) = \frac{Q(x)}{D_0} \int_{z_0}^{\frac{h}{2}} E(z)z dz \quad \text{(A.10)}$$

The internal shear stress energy  $W_{xz}$ :

$$W_{xz} = \int_{-\frac{h}{2}}^{\frac{h}{2}} \frac{1}{2} \frac{\sigma_{xz}^2(x, z)}{G_0(z)} b dz = \frac{1}{2} \frac{Q^2(x)}{D_0^2} \int_{-\frac{h}{2}}^{\frac{h}{2}} \left( \int_{z_0}^{\frac{h}{2}} E(z)z dz \right)^2 \frac{b}{G_0(z_0)} dz_0 \quad \text{(A.11)}$$

Since we have:

$$W_{xz} = \frac{1}{2} \frac{Q^2(x)}{F_0}$$

the shear stiffness  $F_0$  can be identified as:

$$F_0 = \frac{D_0^2}{\int_{-\frac{h}{2}}^{\frac{h}{2}} \left( \int_{z_0}^{\frac{h}{2}} E(z)z dz \right)^2 \frac{b}{G_0(z_0)} dz_0} \quad (\text{A.12})$$

For a homogeneous section, the shear stiffness  $F_0 = \frac{5}{6}G_0bh$  is obtained with the classical shear coefficient  $\kappa = \frac{5}{6}$ .

## A.2 Resolution of the linear buckling with the Bending-Gradient theory using Voigt's notations

In the following, the Voigt notations are used to turn contraction products into conventional matrix products and to ease comprehension, brackets  $[\bullet]$  are used to denote that a tensor is considered in a matrix form. Thus  $[\bullet]$  is a linear operator, reallocating tensor components. The third-order tensor  $\underline{\Phi}$  becomes the vector:

$$[\underline{\Phi}] = \begin{pmatrix} \Phi_{111}^{mn} \\ \Phi_{221}^{mn} \\ \sqrt{2}\Phi_{121}^{mn} \\ \Phi_{112}^{mn} \\ \Phi_{222}^{mn} \\ \sqrt{2}\Phi_{122}^{mn} \end{pmatrix}$$

Forth-order and sixth-order tensors take a matrix form:

$$[\underline{D}] = \begin{pmatrix} D_{1111} & D_{1122} & 0 \\ D_{1122} & D_{2222} & 0 \\ 0 & 0 & 2D_{1212} \end{pmatrix}$$

$$[\underline{h}] = \begin{pmatrix} h_{111111} & h_{111122} & 0 & 0 & 0 & \sqrt{2}h_{111221} \\ h_{221111} & h_{221122} & 0 & 0 & 0 & \sqrt{2}h_{221221} \\ 0 & 0 & 2h_{121121} & \sqrt{2}h_{121211} & \sqrt{2}h_{121222} & 0 \\ 0 & 0 & \sqrt{2}h_{112121} & h_{112211} & h_{112222} & 0 \\ 0 & 0 & \sqrt{2}h_{222121} & h_{222211} & h_{222222} & 0 \\ \sqrt{2}h_{122111} & \sqrt{2}h_{122122} & 0 & 0 & 0 & 2h_{122221} \end{pmatrix}$$

It is noticed here that zeros in matrix  $[\underline{D}]$  and  $[\underline{h}]$  are due to the material orthotropy in each layer (Lebée and Sab, 2011b) and lead to an uncoupling between shear effects in  $x_1$  and  $x_2$ -directions as in the Reissner-Mindlin model.

With Voigt notation, we assume that the identity tensor  $\underline{\mathfrak{I}}$  takes the following form:

$$\underline{\mathfrak{J}} = \begin{pmatrix} 1 & 0 & 0 & 0 & 0 & 1/\sqrt{2} \\ 0 & 0 & 1/\sqrt{2} & 0 & 1 & 0 \end{pmatrix}$$

in order to comply with the following relationship:

$$\underline{\mathbf{Q}} = \underline{\mathbf{J}} [\underline{\mathbf{R}}] = \underline{\mathbf{J}} \begin{pmatrix} R_{111} \\ R_{221} \\ \sqrt{2}R_{121} \\ R_{112} \\ R_{222} \\ \sqrt{2}R_{122} \end{pmatrix}$$

Since modes shapes have a double-sinus formulation (see Equation 3.21) differential operators  $\underline{\nabla}$  may be derived in matrix forms as functions of wavelengths  $K_m$  and  $K_n$ :

$$\underline{\mathbf{K}} = \begin{pmatrix} K_m \\ K_n \end{pmatrix}; \underline{\mathbf{L}} = \begin{pmatrix} K_m & 0 & 0 \\ 0 & K_m & 0 \\ 0 & 0 & -K_m \\ K_n & 0 & 0 \\ 0 & K_n & 0 \\ 0 & 0 & -K_n \end{pmatrix}$$

With such a form the equilibrium equation (3.3) is then rewritten as follows:

$${}^t \underline{\mathbf{K}} \underline{\mathbf{J}} [\underline{\mathbf{R}}] + \lambda_{mn} (K_m)^2 U_3^{mn} = 0 \iff \underline{\nabla} (\underline{\mathbf{i}}; \underline{\mathbf{R}}) + U_{3,\alpha\beta} N_{\alpha\beta}^0 = 0$$

$$[\underline{\mathbf{R}}] = \underline{\mathbf{L}} [\underline{\mathbf{M}}] = \underline{\mathbf{L}} \begin{pmatrix} M_{11} \\ M_{22} \\ \sqrt{2}M_{12} \end{pmatrix} \iff \underline{\mathbf{R}} = \underline{\mathbf{M}} \otimes \underline{\nabla}$$

Then, considering modes shape (Equation 3.21), the eigenvalue problem (Equation 3.20) may be rewritten as a matrix product between a  $7 \times 7$  matrix divided in 4 blocks and the vector  $(U_3^{mn}, [\underline{\Phi}])$  which length is 7.

$$\begin{pmatrix} \lambda_{mn} (K_m)^2 & {}^t \underline{\mathbf{K}} \underline{\mathbf{J}} \underline{\mathbf{L}} [\underline{\mathbf{D}}] {}^t \underline{\mathbf{L}} \\ {}^t \underline{\mathbf{J}} \underline{\mathbf{K}} & \underline{\mathbf{I}} + [\underline{\mathbf{h}}] \underline{\mathbf{L}} [\underline{\mathbf{D}}] {}^t \underline{\mathbf{L}} \end{pmatrix} \begin{pmatrix} U_3^{mn} \\ [\underline{\Phi}] \end{pmatrix} = 0 \quad (\text{A.13})$$

where  $\underline{\mathbf{I}}$  is the  $6 \times 6$  identity matrix. From this equation,  $[\underline{\Phi}]$  may be expressed as a function of  $U_3^{mn}$ :

$$[\underline{\Phi}] = - \left( \underline{\mathbf{I}} + [\underline{\mathbf{h}}] \underline{\mathbf{L}} [\underline{\mathbf{D}}] {}^t \underline{\mathbf{L}} \right)^{-1} {}^t \underline{\mathbf{J}} \underline{\mathbf{K}} U_3^{mn} \quad (\text{A.14})$$

A.2. RESOLUTION OF THE LINEAR BUCKLING WITH THE BENDING-GRADIENT THEORY USING VOIGT'S NOTATIONS

---

and the eigenvalue problem is then expressed only according to the eigenmode  $U_3^{mn}$ :

$$\left\{ \begin{aligned} & {}^t\mathbf{K} \mathbf{J} \mathbf{L} \left[ \mathbf{D} \right] {}^t\mathbf{L} \left( \mathbf{I} + \left[ \mathbf{h} \right] \mathbf{L} \left[ \mathbf{D} \right] {}^t\mathbf{L} \right)^{-1} {}^t\mathbf{J} \mathbf{K} \\ & - (K_m)^2 \lambda_{mn} \end{aligned} \right\} U_3^{mn} = 0 \quad (\text{A.15})$$

The non-trivial solutions ( $U_3^{mn} \neq 0$ ) are thus given by:

$$\lambda_{mn} = \frac{{}^t\mathbf{K} \mathbf{J} \mathbf{L} \left[ \mathbf{D} \right] {}^t\mathbf{L} \left( \mathbf{I} + \left[ \mathbf{h} \right] \mathbf{L} \left[ \mathbf{D} \right] {}^t\mathbf{L} \right)^{-1} {}^t\mathbf{J} \mathbf{K}}{(K_m)^2} \quad (\text{A.16})$$

corresponding to the mode  $U_3 = U_3^{mn} \sin(K_m x_1) \sin(K_n x_2)$ . We may note that the equilibrium is checked for any amplitude  $U_3^{mn}$  in the linear buckling analysis of a initially perfectly straight plate.

### A.3 Deflection of CLT wall with initial imperfections

The problem studied in Appendix A.2 is completed to the case of a plate with an initial imperfection  $U_{3,0}(x_1, x_2)$  corresponding to the buckling mode  $(m, n)$ :

$$U_{3,0}(x_1, x_2) = U_{3,0}^{mn} \sin(K_m x_1) \sin(K_n x_2)$$

The equilibrium (A.13) of the plate under the compressive load  $P_1$  can then be rewritten:

$$\begin{pmatrix} P_1 (K_m)^2 & {}^t \mathbf{K} \mathbf{J} \mathbf{L} \left[ \mathbf{D} \right] {}^t \mathbf{L} \\ {}^t \mathbf{J} \mathbf{K} & \mathbf{I} + \left[ \mathbf{h} \right] \mathbf{L} \left[ \mathbf{D} \right] {}^t \mathbf{L} \end{pmatrix} \begin{pmatrix} U_{3,el}^{mn} \\ \left[ \mathbf{\Phi} \right] \end{pmatrix} = \begin{pmatrix} -P_1 (K_m)^2 U_{3,0}^{mn} \\ 0 \\ 0 \end{pmatrix} \quad (\text{A.17})$$

where  $U_{3,el}(x_1, x_2) = U_{3,el}^{mn} \sin(K_m x_1) \sin(K_n x_2)$  is the elastic deflection, i.e. the deflection added to imperfections under the load  $P_1$ . A solution of this equation is found for :

$$U_{3,el}^{mn} = \frac{U_{3,0}^{mn}}{\frac{\lambda_{mn}}{P_1} - 1}$$

It is noted here that the elastic deflections have a similar expression as in the Timoshenko beam theory (4.16). Then, we suggest to adapt the Ayrton-Perry criterion recalled in Section 4.2.3 to the Bending-Gradient theory.

From the Bending-Gradient theory Lebée and Sab (2011a) the maximum bending stress  $\sigma_{\max}$  can be expressed relatively to the ultimate compressive strength  $\sigma_u$  similarly to (4.18):

$$\frac{\sigma_{\max}}{\sigma_u} = \frac{P_1}{P_{1,u}} \left( 1 + \frac{1}{1 - \frac{P_1}{\lambda_{mn}}} \omega_1 \right) \quad (\text{A.18})$$

where

$$\omega_1 = \frac{6U_{3,0}^{mn}}{h} \frac{\left( \mathbf{I} + \left[ \mathbf{h} \right] \mathbf{L} \left[ \mathbf{D} \right] {}^t \mathbf{L} \right)^{-1} {}^t \mathbf{J} \mathbf{K} {}^t \mathbf{\kappa}}{\lambda_{mn}}$$

and  $P_{1,u}$  is the ultimate compressive load defined as:

$$P_{1,u} = \frac{C_{1111}^{\sigma,0}}{A_{1111}} \sigma_u$$

The vector  $\mathbf{\kappa}$  is given by:

$$\mathbf{\kappa} = \frac{h^2 C_{1111}^{\sigma,0}}{12 A_{1111}} \begin{pmatrix} K_m \left[ C_{1111}^{\sigma,0} (D_{1111} d_{1111} + D_{1122} d_{1122}) + C_{1122}^{\sigma,0} (D_{1111} d_{1122} + D_{1122} d_{2222}) \right] \\ K_n \left[ C_{1111}^{\sigma,0} (D_{1122} d_{1111} + D_{2222} d_{1122}) + C_{1122}^{\sigma,0} (D_{1122} d_{1122} + D_{2222} d_{2222}) \right] \end{pmatrix}$$

### A.3. DEFLECTION OF CLT WALL WITH INITIAL IMPERFECTIONS

---

where  $\underline{d} = \underline{D}^{-1}$  is the bending compliance and  $\underline{C}^{\sigma,0}$  is the plane stress tensor of the layers oriented in the longitudinal direction.  $A_{1111}$  is the in plane stiffness defined as:

$$A_{1111} = \int_{-\frac{h}{2}}^{\frac{h}{2}} C_{1111}^{\sigma}(x_3) dx_3$$

Then, the Ayrton-Perry criterion (4.19) can be adapted to the Bending-Gradient model. This can be usefull particularly when lateral edges are not free since beam models are not sufficient in such cases.



---

## Bibliography

- 408, N.-E., 2012. Timber structure-structural timber and glued laminated timber. determination of some physical and mechanical properties.
- ABAQUS, 2004. Abaqus analysis user's manual: Volume iv: Elements.
- Aicher, S., Dill-Langer, G., 2000. Basic considerations to rolling shear modulus in wooden boards. *Otto-Graf-Journal* 11, 157.
- Allen, H. G., 2013. *Analysis and Design of Structural Sandwich Panels: The Commonwealth and International Library: Structures and Solid Body Mechanics Division*. Elsevier.
- Ambartsumian, S., 1957a. Analysis of two-layer orthotropic shells. *Investiia Akad Nauk SSSR, Ot Tekh Nauk* 7, 93–106.
- Ambartsumian, S., 1957b. Two analysis method for two-layer orthotropic shells. *Izv. An. Arm. SSR Seiya Fiz-Matem nauk* 10 (2).
- Ambartsumian, S., 1970. *Theory of Anisotropic plates: strength, stability, vibration*. Technomic Publishing Company.
- Arcan, M., Hashin, Z., , Voloshin, A., 1978. A method to produce uniform plane-stress states with applications to fiber-reinforced materials. *Experimental mechanics* 18 (4), 141–146.
- ASTM, D., 1981. *Standard methods of testing small clear specimens of timber*. Philadelphia (PA): American Society for Testing and Materials.
- Ayrton, W., Perry, J., 1886. On struts. *The engineer* 62, 464.
- Bardet, S., Gril, J., 2002. Modelling the transverse viscoelasticity of green wood using a combination of two parabolic elements. *Comptes rendus mécanique* 330 (8), 549–556.

## BIBLIOGRAPHY

---

- Bažant, Z., Cedolin, L., 1991. Stability of structures. ASME Appl. Mech. Rev.
- Bogensperger, T., Moosbrugger, T., Silly, G., 2010. Verification of clt-plates under loads in plane. In: 11th World Conference on Timber Engineering (WCTE2010), Riva del Garda.
- Buffon, G., 1741. Experiences sur la force du bois. second memoire. Memoire de l'Academie Royale des Sciences. Paris, 292–334.
- Cabrero, J., Blanco, C., Gebremedhin, K., Martin-Meizoso, A., 2012. Assessment of phenomenological failure criteria for wood. European Journal of Wood and Wood Products 70 (6), 871–882.
- Cariou, J.-L., 1987. Caractérisation d'un matériau viscoélastique anisotrope: le bois. Ph.D. thesis.
- Carrera, E., 2003. Historical review of zig-zag theories for multilayered plates and shells. Applied mechanics reviews 56 (3), 287–308.
- Chow, T., 1971. On the propagation of flexural waves in an orthotropic laminated plate and its response to an impulsive load. Journal of Composite Materials 5 (3), 306–319.
- Ciarlet, P., 1997. Mathematical Elasticity - Volume II: Theory of Plates. Studies in Mathematics and its Applications. North Holland.
- Ciarlet, P. G., Destuynder, P., 1979. Justification of the 2-dimensional linear plate model. Journal de Mécanique 18 (2), 315–344.
- Colling, F., 2014. Creep behavior of cross laminated timber in service class 2. Tech. rep., Hochschule Augsburg, University of Applied Sciences.
- D2718, A., 2003. Standard test method for structural panels in planar shear (rolling shear).
- Dahl, K. B., Malo, K., 2009a. Linear shear properties of spruce softwood. Wood science and technology 43 (5-6), 499–525.
- Dahl, K. B., Malo, K., 2009b. Nonlinear shear properties of spruce softwood: experimental results. Wood science and technology 43 (7-8), 539.
- Davidson, R., 1962. The influence of temperature on creep in wood. Forest Prod J 12, 377–381.
- Dumail, J.-F., Olofsson, K., Salmén, L., 2000. An analysis of rolling shear of spruce wood by the iosipescu method. Holzforschung 54 (4), 420–426.

## BIBLIOGRAPHY

---

- Ehrhart, T., Brandner, R., Schickhofer, G., Frangi, A., 2015. Rolling shear properties of some european timber species with focus on cross laminated timber (clt): test configuration and parameter study.
- European Committee for Standardisation, C., 1993. Eurocode 5—design of timber structures.
- European Committee for Standardisation, C., 24-02-2016. Working draft of design of clt in a revised eurocode 5-1-1.
- Franzoni, L., Lebé, A., Lyon, F., Foret, G., 2016a. Bending behavior of regularly spaced clt panels. In: Proceeding of the 14th World Conference on Timber Engineering, Vienna,(AUT). pp. 22–25.
- Franzoni, L., Lebé, A., Lyon, F., Foret, G., 2016b. Influence of orientation and number of layers on the elastic response and failure modes on clt floors: modeling and parameter studies. *European Journal of Wood and Wood Products* 74 (5), 671–684.
- Franzoni, L., Lebé, A., Lyon, F., Forêt, G., 2017a. Elastic behavior of cross laminated timber and timber panels with regular gaps: Thick-plate modeling and experimental validation. *Engineering Structures* 141, 402–416.
- Franzoni, L., Lebé, A., Lyon, F. t., 2017b. Closed-form solutions for predicting the thick elastic plate behavior of clt panels with gaps. Submitted.
- French, M.**, Mar. 2015. Vienna plans world’s tallest wooden skyscraper.
- Gerhards, C. C., 2007. Effect of moisture content and temperature on the mechanical properties of wood: an analysis of immediate effects. *Wood and Fiber Science* 14 (1), 4–36.
- Goldsmith, V., Grossman, P., 1967. Effect of frequency of vibration on viscoelastic properties of wood. *Journal of the Institute of Wood Science* (18), 44.
- Görlacher, R., 2002. Ein verfahren zur ermittlung des rollschubmoduls von holz. *European Journal of Wood and Wood Products* 60 (5), 317–322.
- Gressel, P., 1984. Prediction of long-term deformation-behavior from short-term creep experiments. *Holz Als Roh-und Werkstoff* 42 (8), 293–301.
- Grossman, P., Kingston, R., 1954. Creep and stress relaxation in wood during bending. *Aust. J. Appl. Sci* 5, 403–417.
- Guggenberger, W., Moosbrugger, T., 2006. Mechanics of cross-laminated timber plates under uniaxial bending. In: WCTE 2006-9th International Conference on Timber Engineering.

## BIBLIOGRAPHY

---

- Hayashi, K., Felix, B., Le Govic, C., 1993. Wood viscoelastic compliance determination with special attention to measurement problems. *Materials and Structures* 26 (6), 370–376.
- Hencky, H., 1947. Über die berücksichtigung der schubverzerrung in ebenen platten. *Ingenieur-Archiv* 16 (1), 72–76.
- Hibbett, Karlsson, Sorensen, 1998. ABAQUS/standard: User's Manual, Part IV : Elements. Vol. 1. Hibbett, Karlsson & Sorensen.
- Holzer, S., Loferski, J., Dillard, D., 2007. A review of creep in wood: Concepts relevant to develop long-term behavior predictions for wood structures. *Wood and Fiber Science* 21 (4), 376–392.
- Iosipescu, N., 1967. New accurate procedure for single shear testing of metals. *J MATER* 2 (3), 537–566.
- Jakobs, A., et al., 2005. Zur berechnung von brettlagenholz mit starrem und nachgiebigem verbund unter plattenartiger belastung mit besonderer berücksichtigung des rollschubes und der drillweichheit. Ph.D. thesis, Universität der Bundeswehr München, Universitätsbibliothek.
- Jöbstl, R., Schickhofer, G., 2007. Comparative examination of creep of glt and clt slabs in bending. In: *International Council for Research and Innovation in building and construction*.
- Jourawski, D., 1856. Sur le résistance d'un corps prismatique et d'une piece composée en bois ou on tôle de fer à une force perpendiculaire à leur longueur. In: *Annales des Ponts et Chaussées*. Vol. 12. pp. 328–351.
- Kączkowski, Z., 1980. Plates–static calculations. Arkady, Warszawa.
- Karacabeyli, E., Douglas, B., 2013. CLT Handbook: cross-laminated timber. FPIInnovations.
- Keunecke, D., Hering, S., Niemz, P., 2008. Three-dimensional elastic behaviour of common yew and norway spruce. *Wood science and technology* 42 (8), 633–647.
- Keunecke, D., Sonderegger, W., Pereteanu, K., Lüthi, T., Niemz, P., 2007. Determination of young's and shear moduli of common yew and norway spruce by means of ultrasonic waves. *Wood science and technology* 41 (4), 309–327.
- Kirchhoff, G. R., 1850. Über das gleichgewicht und die bewegung einer elastischen scheinbe. *Journal für die reine und angewandte Mathematik*.

## BIBLIOGRAPHY

---

- Kollman, F. F. P., Côté, W. A., 1968. Principles of wood science and technology: solid wood. Allen & Unwin.
- Kreuzinger, H., 1999. Platten, scheiben und schalen: Ein berechnungsmodell für gängige statikprogramme. *bauen mit holz* 1, 34–39.
- Le Govic, C., Hadjhamou, A., Rouger, F., Felix, B., 1988. Modélisation du fluage du bois sur la base d'une équivalence temps-température. In: Actes du 2e colloque Sciences et Industries du bois, ARBOLOR Nancy, France. pp. 349–356.
- Lebée, A., Sab, K., 2011a. A bending-gradient model for thick plates. part i: Theory. *International Journal of Solids and Structures* 48 (20), 2878–2888.
- Lebée, A., Sab, K., 2011b. A bending-gradient model for thick plates. part ii: Closed-form solutions for cylindrical bending of laminates. *International Journal of Solids and Structures* 48 (20), 2889–2901.
- Lebée, A., Sab, K., 2012. Homogenization of cellular sandwich panels. *Comptes Rendus Mécanique* 340 (4-5), 320–337.
- Lebée, A., Sab, K., 2013. Justification of the bending-gradient theory through asymptotic expansions. In: *Generalized Continua as Models for Materials*. Springer, pp. 217–236.
- Lebée, A., Sab, K., 2015a. On the generalization of reissner plate theory to laminated plates: Comparison with the bending-gradient theory. submitted.
- Lebée, A., Sab, K., 2015b. On the generalization of reissner plate theory to laminated plates: Theory. submitted.
- Leissa, A. W., 1985. Buckling of laminated composite plates and shell panels. Tech. rep., OHIO STATE UNIV RESEARCH FOUNDATION COLUMBUS.
- Lekhnitskii, S., 1935. Strength calculation of composite beams. *Vestnik inzhener i tekhnikov* 9, 137–148.
- Levinson, M., 1980. An accurate, simple theory of the statics and dynamics of elastic plates. *Mechanics Research Communications* 7 (6), 343–350.
- Li, Y., 2015. Duration-of-load and size effects on the rolling shear strength of cross laminated timber. Ph.D. thesis, University of British Columbia.
- Liu, J. Y., Flach, D. D., Ross, R. J., Lichtenberg, G. J., 1998. An improved shear test fixture using the losipescu specimen. *ASME APPLIED MECHANICS DIVISION-PUBLICATIONS-AMD* 231, 139–148.

## BIBLIOGRAPHY

---

- Lomholt, I., Jan. 2015. Stadthaus london: Murray grove building.
- Love, A. E. H., 1888. The small free vibrations and deformation of a thin elastic shell. *Philosophical Transactions of the Royal Society of London. A*, 491–546.
- Mairs, J., Apr. 2016. Anders berensson proposes wooden skyscraper with decorative facade for stockholm.
- Mårtensson, A., 1994. Mechano-sorptive effects in wooden material. *Wood Science and Technology* 28 (6), 437–449.
- Matar, A., 2003. The mechano sorptive creep of softwood in bending. Ph.D. thesis, South Bank University.
- Medlock, K., May 2016. Construction of world's tallest building is underway in vancouver.
- Mestek, P., 2011. Punktgestützte Flächentragwerke aus Brettspertholz (BSP): Schubmessung unter Berücksichtigung von Schubverstärkungen. na.
- Mindlin, R., 1951. Influence of rotatory inertia and shear on flexural motions of isotropic, elastic plates. *Journal of Applied Mechanics* 18, 31–38.
- Montero, C., 2010. Caractérisation du comportement viscoélastique asymptotique du bois. Ph.D. thesis, Université Montpellier II-Sciences et Techniques du Languedoc.
- Moosbrugger, T., Guggenberger, W., Bogensperger, T., 2006. Cross-laminated timber wall segments under homogeneous shear with and without openings. In: *Proceedings of the 9th World Conference on Timber Engineering*.
- Moses, D. M., Prion, H. G., 2002. Anisotropic plasticity and the notched wood shear block. *Forest products journal* 52 (6), 43.
- Nakai, T., Grossman, P., 1983. Deflection of wood under intermittent loading. *Wood Science and Technology* 17 (1), 55–67.
- Navi, P., Heger, F., 2005. Comportement thermo-hydromécanique du bois: Applications technologiques et dans les structures. PPUR presses polytechniques.
- Nielsen, L. F., 1984. Power law creep as related to relaxation, elasticity, damping, rheological spectra and creep recovery with special reference to wood. In: *IUFRO-Engineering Group Conference*. pp. 181–204.
- Noor, A. K., 1973. Mixed finite-difference scheme for analysis of simply supported thick plates. *Computers & Structures* 3 (5), 967–982.

## BIBLIOGRAPHY

---

- Noor, A. K., 1975. Stability of multilayered composite plates. *Fibre Science and Technology* 8 (2), 81–89.
- Pagano, N., 1969. Exact solutions for composite laminates in cylindrical bending. *Journal of composite materials* 3 (3), 398–411.
- Perret, O., Douthe, C., Lebée, A., Sab, K., 2017a. Determination of the equivalent-layer shear stiffness of clt: Closed-form bounds. (submitted).
- Perret, O., Douthe, C., Lebée, A., Sab, K., 2017b. Determination of the equivalent-layer shear stiffness of clt: four-point bending of cfrp sandwich beams. (submitted).
- Perret, O., Lebée, A., Douthe, C., Sab, K., 2016. The bending–gradient theory for the linear buckling of thick plates: Application to cross laminated timber panels. *International Journal of Solids and Structures* 87, 139–152.
- Phan, N., Reddy, J., 1985. Analysis of laminated composite plates using a higher-order shear deformation theory. *International Journal for Numerical Methods in Engineering* 21 (12), 2201–2219.
- Pirvu, C., Karacabeyli, E., 2014. Time-dependent behaviour of clt. In: *World Conference on Timber Engineering*.
- Reddy, J., 1984. A refined nonlinear theory of plates with transverse shear deformation. *International Journal of solids and structures* 20 (9-10), 881–896.
- Reissner, E., 1945. The effect of transverse shear deformation on the bending of elastic plates. *Journal of Applied Mechanics*.
- Reissner, E., 1975. On transverse bending of plates, including the effect of transverse shear deformation. *International Journal of Solids and Structures* 11 (5), 569–573.
- Reissner, E., 1984. On a certain mixed variational theory and a proposed application. *International Journal for Numerical Methods in Engineering* 20, 1366–1368.
- Ren, J., 1986a. Bending theory of laminated plate. *Composites science and technology* 27 (3), 225–248.
- Ren, J., 1986b. A new theory of laminated plate. *Composites Science and Technology* 26 (3), 225–239.
- Ren, J., Owen, D., 1989. Vibration and buckling of laminated plates. *International Journal of Solids and Structures* 25 (2), 95–106.
- Sab, K., Lebée, A., 2015. *Homogenization of heterogeneous thin and thick plates*. John Wiley & Sons.

## BIBLIOGRAPHY

---

- Schickhofer, G., Brandner, R., Bauer, H., 2016. Introduction to clt, product properties, strength classes. of COST Actions FP1402 & FP1404 KTH Building Materials, 10.3. 2016 Cross Laminated Timber—A competitive wood product for visionary and fire safe buildings, 9.
- Schniewind, A., Barrett, J., 1972. Wood as a linear orthotropic viscoelastic material. *Wood Science and Technology* 6 (1), 43–57.
- Sebera, V., Muszyński, L., Tippner, J., Noyel, M., Pisaneschi, T., Sundberg, B., 2015. Fe analysis of clt panel subjected to torsion and verified by dic. *Materials and Structures* 48 (1-2), 451–459.
- Shiro, N., Atsushi, M., Tatsuya, S., Yasuhiro, A., Nobuyoshi, Y., Takeshi, H., Naoto, A., Motoi, Y., 2014. Creep and duration of load characteristics of cross laminated timber. In: *Proceedings of the 13th World Conference on Timber Engineering (WCTE 2014)*, Quebec City.
- Silly, G., 2010. Numerical study on in-plane shear and torsional stiffness of clt.
- Stora Enso, C., 2014. Document technique d’application 3/13-750 : Panneaux bois Ã usage structurel. *AgrÃment Technique EuropÃen*.
- Stürzenbecher, R., Hofstetter, K., Eberhardsteiner, J., 2010. Structural design of cross laminated timber (clt) by advanced plate theories. *Composites Science and Technology* 70 (9), 1368–1379.
- Stürzenbecher, R., Hofstetter, K., Eberhardsteiner, J., 2012. Introduction to cross laminated timber. *Wood Design Focus* 22 (2), 12.
- Thiel, A., 2013. Uls and sls design of clt and its implementation in the cltdesigner. In: *Focus solid timber solutions—European conference on cross laminated timber (CLT)*. The University of Bath, Bath.
- Thiel, A., Krenn, H., 2016. Buckling lods for cross-laminated timber elements under uniaxial in-plane compression. In: *Proceedings of the 14th World Conference on Timber Engineering (WCTE 2016)*, Vienna.
- Thiel, A., Schickhofer, G., 2010. Cltdesigner—a software tool for designing cross-laminated-timber elements: 1d-plate-design. In: *World conference on timber engineering*, Italy.
- Timoshenko, S., Gere, J., 1961. *Theory of elastic stability*. 1961. McGrawHill-Kogakusha Ltd, Tokyo.

## *BIBLIOGRAPHY*

---

- Touratier, M., 1991. An efficient standard plate theory. *International journal of engineering science* 29 (8), 901–916.
- Whitney, J., 1969. The effect of transverse shear deformation on the bending of laminated plates. *Journal of Composite Materials* 3 (3), 534–547.
- Whitney, J., 1972. Stress analysis of thick laminated composite and sandwich plates. *Journal of Composite Materials* 6 (4), 426–440.
- Whitney, J., Pagano, N., 1970. Shear deformation in heterogeneous anisotropic plates. *Journal of Applied Mechanics* 37 (4), 1031–1036.
- Yang, P., Norris, C., Stavsky, Y., 1966. Elastic wave propagation in heterogeneous plates. *International Journal of Solids and Structures* 2 (4), 665–684.
- Yoshihara, H., Furushima, T., 2003. Shear strengths of wood measured by various short beam shear test methods. *Wood science and technology* 37 (3-4), 189–197.
- Yoshihara, H., Kubojima, Y., 2002. Measurement of the shear modulus of wood by asymmetric four-point bending tests. *Journal of wood science* 48 (1), 14–19.
- Yoshihara, H., Kubojima, Y., Nagaoka, K., Ohta, M., 1998. Measurement of the shear modulus of wood by static bending tests. *Journal of wood science* 44 (1), 15–20.
- Youngs, R., 1957. The perpendicular-to-grain mechanical properties of red oak related to temperature, moisture content and time. Ph.D. thesis.
- Zhou, Q., Gong, M., Chui, Y. H., Mohammad, M., 2014. Measurement of rolling shear modulus and strength of cross laminated timber fabricated with black spruce. *Construction and Building Materials* 64, 379–386.

## **Strength and Stability of Cross Laminated Timber walls at short and long term**

This PhD thesis addresses the issue of CLT wall buckling. These wooden panels, made of boards which are glued cross-wise, are more and more used in construction. The current trend of the market is to design high-rise buildings which raises the issue of the compressive strength of such walls. It turns out that wood is a highly anisotropic material. Especially, the shear stiffness and strength perpendicular to the grain (rolling shear) are much weaker than in the direction parallel to the grain. This high contrast requires more elaborate design criteria than classical tools used in timber engineering. This work is organized in two main parts. First, the equivalent rolling-shear behavior of a CLT layer is investigated. Bounds are established for the stiffness of an equivalent layer using a theoretical approach. These bounds are validated by means of a new experimental set-up which allows the measurement of the rolling shear stiffness with less variability than the classical single lap shear test. In the second part, this data is used in the buckling analysis of CLT walls with increasing refinements. First, the linear buckling load of a thick plate without imperfection is established. This load is based on a new higher-order plate theory and reveals that the critical load based on a thin plate theory (Kirchhoff-Love) cannot predict correctly the strength of CLT walls. Then, the influence of imperfections is introduced adapting the classical approach from Ayrton and Perry to the case of a Timoshenko beam. This extension reveals that a new design criterion has to be satisfied under buckling which is specific to CLT. Finally, this analysis is extended to long term loads assuming a simple creep law and leading to a new simple design criterion which may be easily introduced in current design codes.

**Keywords** Cross Laminated Timber, Equivalent-layer stiffness, Rolling shear, short and long term buckling, Imperfections

## Résistance et Stabilité de murs en bois lamellé-croisé à court et à long terme

Ce mémoire de thèse aborde le problème du flambement de murs en bois lamellé-croisé. Ces panneaux de bois, constitués de planches collées perpendiculairement, sont de plus en plus utilisés dans la construction. La tendance actuelle du marché est de concevoir des immeubles de grande hauteur, ce qui soulève la question de la résistance en compression de ces murs. Il s'avère que le bois est fortement anisotrope. En particulier, la raideur et la résistance en cisaillement perpendiculaire aux fibres, également appelé cisaillement roulant, sont beaucoup plus faibles que dans la direction parallèle aux fibres. Ce fort contraste nécessite un critère de conception plus élaboré que les outils classiques utilisés dans l'ingénierie du bois. Ce travail est organisé en deux parties. Dans la première partie, la raideur équivalente de cisaillement transverse d'un panneau de bois lamellé-croisé est étudiée. Des bornes sont établies par une approche théorique. Ces bornes sont validées par un nouveau dispositif expérimental qui permet la mesure de la raideur en cisaillement roulant avec une variabilité plus faible que le test *single-lap* classiquement utilisé. Dans la deuxième partie, ces données sont utilisées dans l'analyse du flambement de panneaux en bois lamellé-croisé en raffinant progressivement le problème. Dans un premier temps, la charge critique de flambement linéaire d'une plaque épaisse sans imperfections est établie. Cette charge critique est basée sur une nouvelle théorie de plaque d'ordre supérieur et montre que la charge critique de flambement basée sur une théorie de plaque mince (Kirchhoff-Love) ne peut pas estimer correctement la résistance de murs en bois lamellé-croisé. Dans un second temps, l'influence des imperfections est étudiée en adaptant l'approche classique de Ayrton et Perry à une poutre de Timoshenko. Cette extension a révélé qu'un nouveau critère de résistance doit être satisfait lors du flambement qui est spécifique aux murs en bois lamellé-croisé. Dans un dernier temps, cette analyse est étendue aux charges permanentes en supposant une loi de fluage simple qui conduit à un nouveau critère de conception simple qui pourrait facilement être adopté dans les codes de conception actuels.

**Mots-clés** Bois Lamellé-Croisé, Raideur de couche équivalente, Cisaillement-roulant, Flambement à court et long terme, Imperfections